Optical feedback sensing in microfluidics : design and characterization of VCSEL-based compact systems

Yu Zhao

THÈSE

En vue de l'obtention du

DOCTORAT DE L'UNIVERSITÉ DE TOULOUSE

Délivré par :

Institut National des Sciences Appliquées de Toulouse (INSA de Toulouse)

Présentée et soutenue par :
Yu ZHAO

le jeudi 28 septembre 2017

Titre :

Optical feedback sensing in microfluidics : design and characterization of VCSEL-based compact systems

École doctorale et discipline ou spécialité :
ED GEET : Photonique et Systèmes Optoélectroniques

Unité de recherche :
LAAS-CNRS

Directeur/trice(s) de Thèse :

Julien PERCHOUX
Véronique BARDINAL

Jury :
Dr. Pierluigi DEBERNARDI, Rapporteur
Dr. Santiago ROYO, Rapporteur
Pr. Anne HUMEAU-HEURTIER, Présidente
Pr. Michele NORGIA
Pr. Thierry BOSCH, Invité

Résumé

L'interférométrie par retro-injection optique (OFI) est une technique de détection émergente pour les systèmes fluidiques. Son principe est basé sur la modulation de la puissance et/ou de la tension de polarisation d'une diode laser induites par interférence entre le faisceau propre de la cavité laser et la lumière réfléchie ou rétro-diffusée par une cible distante. Grâce à l'effet Doppler, cette technique permet de mesurer précisément la vitesse de particules en mouvement dans un fluide, et de répondre aux besoins croissants de mesure de débit dans les systèmes d'analyse biomédicale ou chimique.

Dans cette thèse, les performances de la vélocimétrie par rétro-injection optique sont étudiées théoriquement et expérimentalement pour le cas de micro-canaux fluidiques. Un nouveau modèle numérique multi-physique (optique, optoélectronique et fluidique) est développé pour reproduire les spectres Doppler expérimentaux. En particulier, les effets de la concentration en particules, de la distribution angulaire de la diffusion du laser par les particules, ainsi que du profil d'écoulement dans le canal sont pris en compte. Un bon accord est obtenu entre les vitesses d'écoulement théoriques et expérimentales. Ce modèle est également appliqué avec succès à la mesure de la vitesse locale dans un micro-canal et à l'analyse de l'impact sur le signal des configurations particulières de canal.

Enfin, la conception d'un capteur OFI tirant parti des avantages des Lasers à Cavité Verticale à Emission par la Surface (VCSEL) est proposée. Grâce au développement de techniques de microfabrication à base de matériaux polymères, un premier démonstrateur composé d'un VCSEL à lentille intégrée est réalisé et testé sans aucune optique macroscopique additionnelle. Les résultats obtenus en termes de mesure de flux sur des canaux micro-fluidiques de tailles différentes valident l'intérêt de cette approche et ouvrent la voie vers la réalisation de capteurs OFI ultra-compacts.

Mots clés: Interférométrie par réinjection optique; VCSEL; Micro-fluidique; Mesure de débit; Effet Doppler

Abstract

Optical feedback interferometry (OFI) is an emerging sensing technique which has been studied in fluidic systems. This sensing scheme is based on the modulation of the laser emission output power and/or the junction voltage induced by the interaction between the back-scattered light from a distant target and the laser inner cavity light. Thanks to the Doppler Effect, OFI can precisely measure the velocity of seeding particles in flowing liquids which is much required in chemical engineering and biomedical fields.

In the present thesis, optical feedback interferometry performance for microscale flow sensing is studied theoretically and experimentally. A new numerical modeling approach based on multi-physics numerical simulations for OFI signal simulation in the micro-scale flowmetry configuration is presented that highlight the sensor performances. In this model, many factors are involved such as particle concentration and laser-particle scattering angle distribution and flow velocity distribution. The flow rate measurement shows good agreement with the modeling. The implementation of OFI based sensors in multiple fluidic systems, investigating the impact of the fluidic chip specific configuration on the sensor signal.

Finally, a compact OFI flowmetry sensor based on Vertical-Cavity Surface-Emitting Lasers (VCSELs) using micro optical fabrication techniques is demonstrated as well. The simulation method for the design and the microfabrication procedures are detailed. After an evaluation of the experimental results, the capabilities of this new OFI sensor in microfluidic measurements are emphasized, thus demonstrating an open path towards ultra-compact microfluidic systems based on the OFI sensing technique.

Keywords: Optical feedback interferometry; VCSEL; microfluidics; flow measurement; Doppler Effect.

Acknowledgments

Many thanks to Mr. Pierluigi Debernardi and Mr. Santiago Royo for accepting to be the reviewers of my thesis. I am thankful for any advice and suggestions from all the jury members as well.

Here, I would like to express my sincere gratitude to my supervisors Dr. Julien Perchoux and Pr. Véronique Bardinal for the continuous support of my Ph.D study and related research, for their patience, motivation, and immense knowledge. Their guidance helped me in all the time of research and writing of this thesis. I could not have imagined having better supervisors and mentors for my Ph.D study.

I'm also grateful to all the researchers in groups OSE for their kindness and the positive work ambiance in the course of my PHD study: Thierry Bosch, Francoise Lizion, Olivier Bernal, Francis Bony, Hélène Tap, Han-Cheng Seat and Adam Quotb. I also appreciate Clement Tronche and Francis Jayat for their great technical help in experiments and instruments, and Emmanuelle Tronche for her help in the management work for me.

My sincere thanks also goes to all the researchers and Ph.D students in group MICA: Philippe Menini, Emeline Descamps, Jérôme Launay, François Olivie, Vincent Raimbault, Isabelle Seguy, Pierre Temple Boyer. Particularly thanks to Dr. Thierry Camps for his solid knowledge about the VCSEL. Besides MICA members, I would like also thank the technicians in LAAS clean room for the help in micro-fabrication: Benjamin Reig, Fabien Mesnilgrente, Jean-Baptiste Doucet, Rémi Courson,…

I would like to thank my friends and colleges, the other Ph.D students: Antonio Luna Arriaga, Jalal Al Roumy, Evelio R. Miquet, Laura Le Barbier, Lavinia Ciotirca, Lucas Perbet and Blaise Mulliez, Fernando Urgiles, Harris Apriyanto and Mengkoung Veng. I equally appreciate the time spent with the stagiaires José Luis, Alejandro, Einar and Fadila.

Last but not the least, I must express my most profound gratitude to my parents and my wife for supporting me spiritually throughout the thesis and my life in general. I miss my grandfather very much, I hope today he can be proud of me in heaven.

Bless my daughter Lucie.

Zhao Yu

Toulouse

Contents

General introduction

With the development of micro-technology during the last two decades, a significant progress has been made in integrated microfluidic devices. Thanks to the miniaturization and integration of the chemical process this change of scale can provide many advantages such as high speed, reduction of reagent consumption, short reaction time and lower cost. Therefore microfluidic systems are of great interest in biomedical and chemical engineering domains, such as clinical diagnostics of pathologies, single-cell analysis and manipulation, drug development and chemical synthesis[1].

In microfluidic systems such as droplet-based systems where the droplets contain the reagents and analytes, the flowing velocity inside the channel determines the duration of reaction or characterization, therefore flowing velocity or volume flow rate measurement is fundamental for the micro-scale flow study.

Moreover, the flowmetry sensor in microfluidic system is also of great direct interest in biomedical and chemical engineering applications. In biomedical applications, microvascular blood flow imaging can offer the doctors the blood perfusion information, which is remarkably useful to improve patient health care or treatment, for example, assessment of burn depth, skin cancer diagnostics and drug interaction with metabolism[2]–[5]. In chemical engineering, the flowing velocity field distribution is also fundamental for many manipulations, such as different liquids mixing, two-phase fluid study, …[6].

Taking the advantage of non-destructive interaction with the objects, optical sensing techniques have attracted increasing attention during the last decades as a tool for addressing the velocity measurement of flows. Nowadays numerous optical technologies have been proposed, such as Dual-Slit (DS)[7], Particle Image Velocimetry (PIV)[8] and Laser Doppler Velocimetry (LDV)[9].

OFI (Optical Feedback Interferometry) is a very simple interferometric sensing technology based on the optical feedback effect in lasers. It was early proposed to measure displacement [10], [11], velocity [12]–[15] and vibration[16], [17]. Its principle

is the following: a part of the emitted laser beam reflected or scattered by a distant target re-enters the laser cavity where it interacts with the initial laser free-running light. As an emerging sensing technique, OFI has been studied in fluidic systems for flowing velocity monitoring in microfluidic channels [18]–[21].

However, most of the existing related OFI based studies concern millimeter scale fluidic systems, while only a few of them are treating micro-scale configurations. OFI based microfluidic flowmeter sensor study remains indeed challenging because of the many practical problems, especially with systems where the typical scale is smaller than the sensing volume dimension. These challenges come from the complexity of structure and the flow feature in the microscale reactor, and the difficulty of particle scattering performance study.

In the current thesis, optical feedback interferometry performance for micro-scale flow sensing is studied theoretically and experimentally. A novel numerical modeling approach based on a multi-physics approach for OFI flowmeter signal simulation is presented. In this model, many factors are involved such as particle concentration, laser-particle scattering angle distribution, and fluidic velocity distribution. This model is then validated in different experimental configurations using a commercial 670nm VCSEL (Vertical-Cavity Surface-Emitting Laser) as the laser source. This kind of laser diode presents many advantages compared to edge-emitting lasers for OFI interferometry, such as parallel operation, short cavity length (single longitudinal mode) and circular beam. Finally, based on previous work on microfabrication techniques, a miniaturized optical component involving a polymer pedestal and a microlens integrated directly on an 850nm VCSEL chip was implemented to build a more compact OFI flowmetry sensor system. The measurement results from this system are demonstrated as well and compared to modeling.

The thesis manuscript is organized as follows:

Chapter 1 presents a review of the optical methods used for flowmetry, particularly the Laser Doppler Velocimetry, the Particle Imaging Velocimetry and the Optical Feedback Interferometry. In this review, the techniques are compared in the frame of historical aspects, basic sensing system, sensing principle, and recent developments associated

with microfluidic measurement and biomedical applications. The comparison highlights the potential of OFI in microfluidic measurement.

In the second chapter, based on the well-known three-mirror cavity model, a mathematic model is proposed that describes the laser diode output power behavior in presence of the feedback perturbation from multiple scatterers. Using the commercial optical ray tracing software ZEMAX-EE, the laser beam propagation inside the micro-scale reactor is first simulated, thereby both the laser illumination and feedback light power from each particle are evaluated.The flowing velocity profile in the micro-scale channels assessed using a computational fluid dynamics (CFD) software Fluent. The Doppler frequency spectrum is finally reproduced via a Matlab algorithm. At the end of this chapter, additional physical aspects are involved in the model such as scattered light angular distribution and the particle concentration.

The third chapter presents a series of measurements to validate the method proposed in Chapter 2. The experiment results are compared with simulation results and discussed in detail. Several important factors influencing the OFI signal spectrum are studied: particle size, particle concentration, channel rear surface reflectivity and channel dimension.Depth direction velocity profile scan measurements are also investigated.

In Chapter 4, a compact OFI flowmetry sensor based on lensed-VCSELs mounted on a Printed Circuit Board (PCB) using micro-optical fabrication techniques is designed. The aim is to avoid the use of any macroscopic lens while keeping a reduced beam size in the channel (few tens of microns). The design methodology of the system is first presented. Then we expose the technological issues we had to solve to fabricate all parts. Consistent measurement results are obtained, proving the capabilities of this OFI sensor presenting a small footprint (few millimeters) in microfluidic measurements

Finally, a general conclusion is given and further work extensions are proposed.

1 Optical sensors in flow measurement

Introduction

Biomedical applications are experiencing a trend towards more accurate, less expensive and more compact systems. Microfluidic embedded systems can be aligned very well with this trend due to their special advantages such as high-speed, compacity, and low cost. Thereby, such systems have been developed dramatically in biomedical and chemical engineering projects during the last two decades. Optical flowmetry sensor, as a mature and non-invasive sensing technique which has been applied extensively to fluidic velocity measurement, could be a promising tool satisfying requirements of microfluidic embedded systems.

In this chapter, a comparative review of optical techniques applied to flow measurements is briefly presented with a specific highlight for two well-established techniques: Laser Doppler Velocimetry and Particle Image Velocimetry. Previous work on optical feedback interferometry in the microfluidic and biomedical context is detailed. To propose a general understanding of them, all the techniques are described in the following aspects: history, sensing principle, recent application achievements in fluidic systems and biomedical applications. Finally, all of them are compared for a summary.

1.1. Laser Doppler Velocimetry (LDV)

Laser Doppler velocimetry is the first noninvasive optical technology that has been employed in fluidic sensing application since the 1960s. This sensing scheme is based on the well-known Doppler Effect of the laser light that is scattered by flowing particles carried in the fluid. By measuring the Doppler frequency shift, the velocity assessment of the seeding particles in the fluidic system can be retrieved. Nowadays, it has been developed as a well-commercialized technique that monitors the gas or liquid flowing velocity in the human body, atmosphere or ocean, etc…

1.1.1. History

In 1964, Yeh and Cummins for the first time successfully measured flowing velocity profiles by measuring the Doppler frequency shift of the light scattered from small flowing particles [22]. The scattered and reference radiation were heterodyned on a photomultiplier (PMT) producing an electrical signal at the difference frequency which was associated with the Poiseuille's law [23]. In their work, the monochromatic laser beam from a 632.8 nm He-Ne laser source was separated by a beam splitter into two beam paths. One was defined as the signal beam emitting onto the polystyrene solution in a 10cm diameter tube, the other as the reference beam. Both beams were collected by a PMT producing the signal with the beat frequency. Since the 1960s, numerous LDV works have been presented in velocity measurement in the flow of gases and liquids [24]–[26].

LDV also drew great interest as well in biomedical measurements. In 1972, for the first time, Riva et al applied LDV to in-vivo measurement [27], they successfully measured blood flowing velocity in retinal arteries of the rabbit. They investigated the LDV signal in presence of the blood multiple scattering performances in both ~200μm tube and smaller retina arterials. For the application to human retina, they concluded that the 10mW, 2 minutes He-Ne laser exposure in the rabbit produced no retinal damage. Furthermore, the signal-to-noise ratio (SNR) achieved in the experiments suggested that a reduction of incident power by a factor of 10 or even more would still permit the observation of the spectrum.
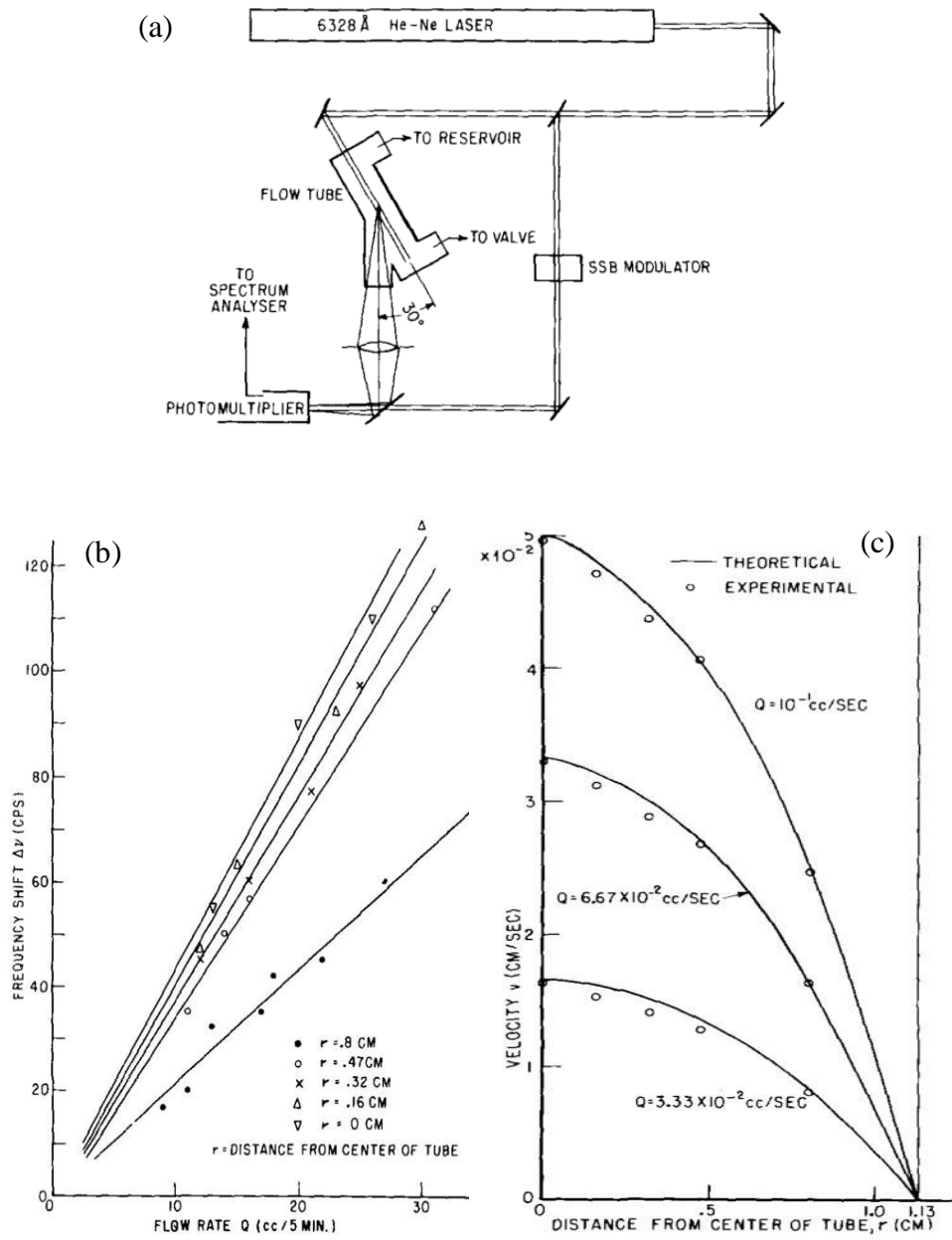
Fig.1.1. Experimental setup and the main results in Yeh and Cumming's work[22]. (a) Setup schematic (b) Experimental frequency shifts (markers) at several radial positions as a function of the flow rate with the linear fitting (lines). (c) Velocity profile (markers) in different flow rates compared with the Poiseuille's law (lines).
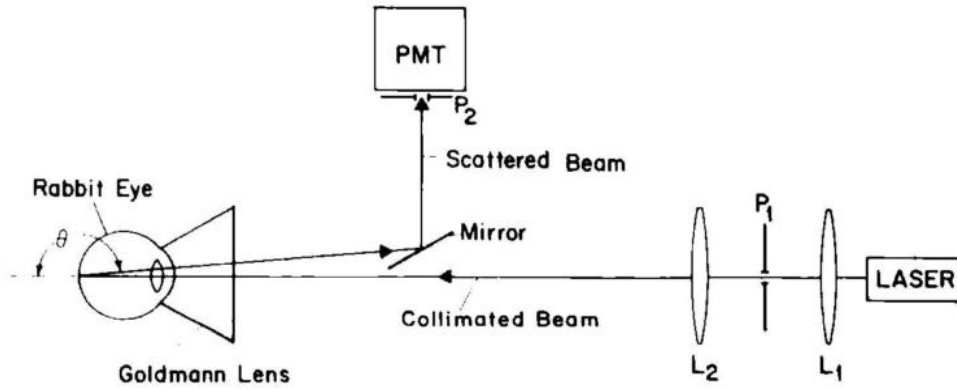
Fig.1.2. Schematic of experimental setup for blood velocity measurements on rabbit retina [27].

1.1.2. Sensing principle

Most modern LDV systems employ a dual-beam configuration as shown in Fig.1.3[28]. A laser source at λ_0 is split into two laser beams using low-aberration optics elements. The dual beams focus and interact inside the channel with an angle of 2θ. A localized fringe pattern is created in the intersection area. When the two incident waves are in phase, constructive interferences appear, locally leading to a maximum of intensity (bright fringes). On the contrary, destructive interferences appear of minimum intensity (dark fringes) in the case dual incident beams are out of phase. The set of fringes which is referred to as the measurement volume or probe volume has a fixed fringe spacing which is defined as:

$$\lambda_f = \frac{\lambda_0}{2\sin\theta} \tag{1.1}$$

When a flowing particle crosses the fringes, it scatters light which is collected by the receiver and projected on the surface of a highly sensitive photodetector. The photodetector records a signal burst, whose amplitude is modulated by the fringe pattern. The burst frequency f is measured and is directly proportional to the particle velocity component normal to these fringes. The measured particle velocity component is found as:

$$V = f\lambda_f \tag{1.2}$$
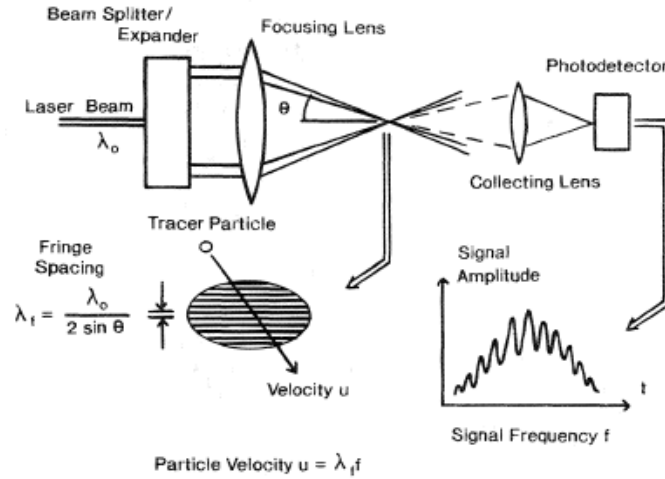
Fig.1.3. Principle of dual-beam laser Doppler velocimetry[28].

1.1.3. Recent achievements

Since the 1970s, great effort has been made to increase the accuracy of LDV sensors in fluidic measurements for microfluidic and nano-fluidic applications and turbulence research. One most critical problem in accuracy development is wave-front distortion that is due to self-diffraction of the (Gaussian) laser beam. To overcome this limitation, Lars Büttneretal.et al [9] designed a novel dual-beam LDV system that was able to measure the position of a passing tracer particle in the measurement volume. Contrary to the previous dual laser beam configuration, where the sensor was based on the superposed interference fringe systems generated by one with convergent and the other with divergent fringes, by two wavelengths (660nm and 825nm). Because the local fringe spacings are different for the two wavelengths, the Doppler frequencies are also different. The ratio of these two frequencies is characteristic for the position at which the particle passes the bi-chromatic interference fringe system, and therefore the position can be determined.

9
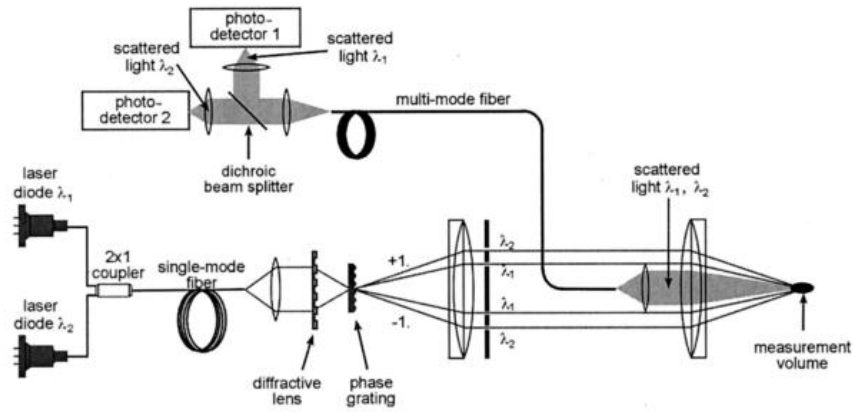
Fig.1.4. Schematic of the dual-wavelength based laser Doppler velocity profile sensor in Büttner's work[9].

As shown in Fig.1.4, the radiation of at 660nm and 825nm wavelength was combined by a single-mode fiber coupler and guided via a singlemode fiber to a collimating lens and a diffractive lens to focus the beams. A transmission phase grating was placed in the center of the separated beam waists, leading +1st and -1st diffraction orders beam were used as the LDA partial beams focused again to generate the fringes. Two photo-detectors measured the signal at different wavelengths. In Fig.1.5, the two interference fringe systems in their work with convergent and divergent fringes were in different laser axial positions (Z direction): the beam waist of 660nm laser is placed before the crossing plane of the partial beams, and the beam waist of the other (850nm) is placed behind the crossing plane to discriminate the particle passing position in Z direction.
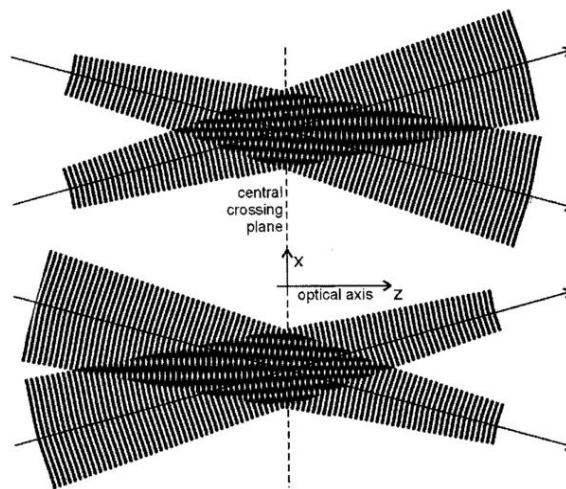
Fig.1.5. Two (superposed) interference fringe systems are generated at two laser wavelengths in Büttner's work[9]. Top: convex wavefronts that result in divergent fringes at 650nm. Bottom: concave wavefronts that result in convergent fringes at 850nm.

In 2010, König et al. from the same group proposed a novel laser Doppler velocity profile sensor. Instead of parallel fringe systems, two superposed fan-like fringe systems at different wavelengths (532nm and 654nm) are employed to determine the velocity distribution inside a 1600μm×107μm microchannel. The setup is shown in Fig.1.6, the laser radiation was split into two separate beams by two beam splitter cubes. Each beam passed an acoustic-optical modulator (AOM) driven by a function generator and was guided via single-mode fiber to a third beam splitter merging again. With the alternating operation of the AOMs time division multiplexing can be realized. Thereby the first diffraction orders are guided to the sensor head by a single-mode fiber. Converging or the diverging fringe system can be chosen by changing the currently active AOM. In the flow rate measurement operated in this system, good velocity uncertainty of 0.18% and a spatial resolution of 960 nm in laser axial direction are demonstrated in the flow[29].
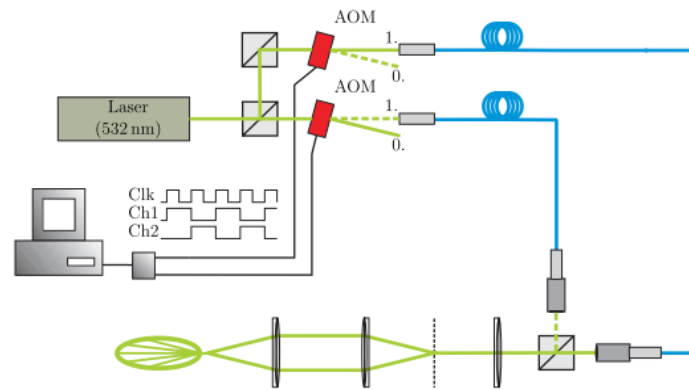
Fig.1.6. Setup of the time division multiplexing velocity profile sensor[29].

1.1.4. Biomedical applications

As a non-invasive and fast technique, LDV has been drawn increasing attention in biomedical domains. Various related measurement works are overviewed here to give a general understanding of LDV's evolution in this domain.

As an approach of in-vivo velocimetry that facilitates 2D flow velocity mapping by mechanical translating instruments, Scanning Laser Doppler Velocimetry (SLDV) has been a standard tool in diagnostics. Essex and Byrne[30] demonstrated a scanning laser Doppler velocimetry system with continuously moving laser beams. In their work (Fig.1.7), a rotating mirror was used to apply 2D scan on the skin. Human retina blood

perfusion can be measured by a SLDV scheme of a spatial resolution of up to 10μm and a temporal resolution of 2 s for a scan of 256×64 pixels [31]. Besides blood velocity or perfusion diagnostics, SLDV can be also used in the diagnosis of burn depth. Papeet al. [32] reported the use of laser Doppler imaging in the assessment of burns intermediate depth (Fig.1.8): high perfusion shows superficial burns area (ankle) and low perfusion shows the unburned skin area (toes and sole). By this result, doctors can distinguish superficial burns from deeper burns that need surgical treatment.
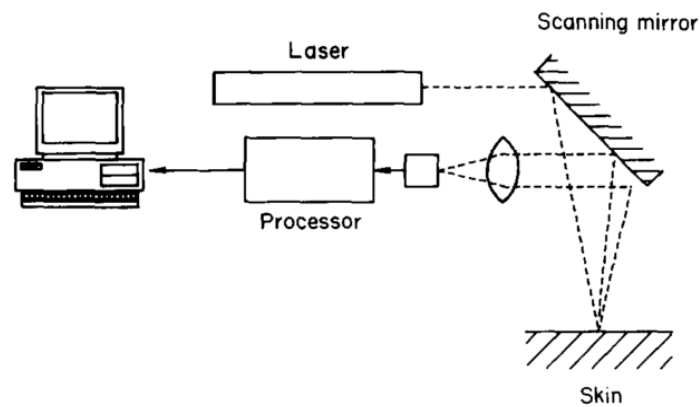
Fig.1.7. Schematic of typical SLDV setup[30].
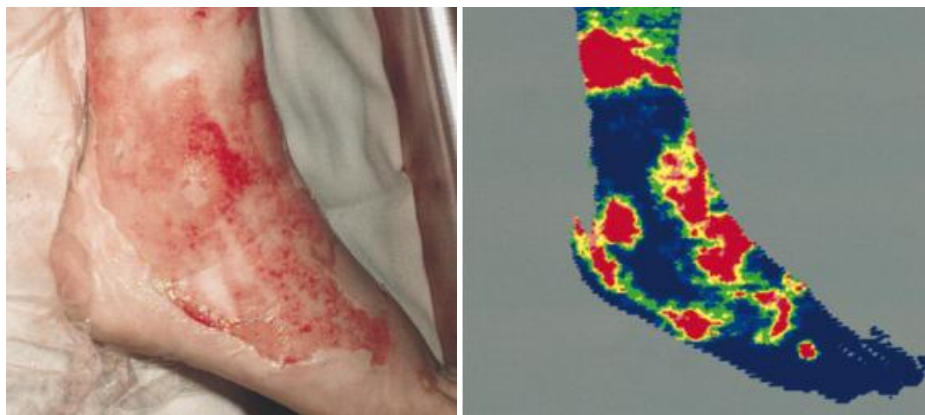
Fig.1.8. Caucasian patient with mixed depth burn of foot and ankle. (a) Clinical photograph. (b) Scanning Laser Doppler image. Areas of high perfusion (red and yellow) and low perfusion (blue)[32].

Other techniques, such as Planar Doppler velocimetry[33], [34], Optical Doppler Coherence Tomography (ODCT) have been also documented to biomedical or in-vivo measurement applications [5], [35]–[37].

After 50 years development, as one of the most mature optical flowmeter techniques of high spatial resolution and 2D scanning capability, LDV has been applied widely in biomedical measurements. However, the complicated beam paths system is still challenging for alignment and investigation in small embedded microfluidic systems.

1.2. Particle image velocimetry (PIV)

Particle image velocimetry (PIV) is one of the most advanced techniques in fluid velocity measurement which can provide a very high spatial resolution (<100nm) [6], [38]–[41]. This technique represents a quantitative extension of the qualitative flow-visualization of instantaneous velocity measurements in (2D or 3D) domains that have been practiced during the last three decades.

1.2.1. History

The first investigators that achieved PIV measurement used the method of laser speckle technique. In 1977, Barker[42], Dudderar[43], and Grousson[44], three different groups independently implemented the velocity profile measurement in a tube flow by means of measuring laser speckle phenomenon using double-exposure photographs and planar laser light sheet illumination. Later, Meynart applied this method to various measurements, including laminar and turbulent flow in gas and liquid [45]–[48].

Adrian[49] argued that apart from the laser speckle pattern, the image of the individual particle could be also the visibility of flow measurement. Since then, particle image velocimetry (PIV) has been proposed.

In 1998, Santiago et al.[7] reported a micro-scale Particle Image Velocimetry (µPIV). In µPIV, the optical and mechanical configurations are different than traditional PIV. In particular, a volume illumination is employed in µPIV instead of light sheet illumination. During the last two decades, µPIV has been a useful tool for fundamental research of microfluidics as well as for the detailed characterization in life science, lab-on-a-chip, biomedical research, microchemical engineering, analytical chemistry and other related fields of research[50].

1.2.2. Sensing principle

As illustrated in the Prasad et al. work [40], the basic requirements for the PIV technique include a laser source, a recording medium (film, CCD, or holographic plate), an optically transparent test-section, and a computer for image processing.
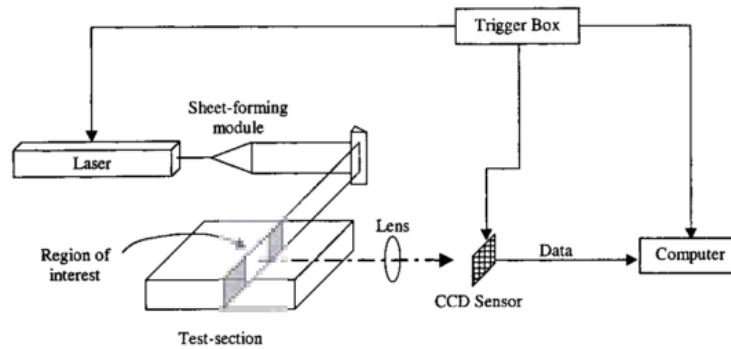
Fig.1.9. Basic setup of a PIV system [40].

Two widely used PIV methods in fluidic measurements are described in the following context: particle tracking velocimetry (PTV) and correlation-based PIV.

a. Particle tracking velocimetry

Particle tracking velocimetry (PTV) is an extension of flow visualization technique using tracer particles in fluid flows. When the tracer particles are illuminated by two successive bursts of light, two images are produced from the light scattered by the particles in Fig.1.10 (AHD, TU Delft, inc.). As a result, the distance between the particles on each image is determined by the local velocity of the fluid. Early measurements of particle displacements were made by hand using blow-ups of photographs of particle-laden flow fields. As technology advanced, these photographs are obtained using CCD or CMOS array cameras and the determination of particle displacements was automated.
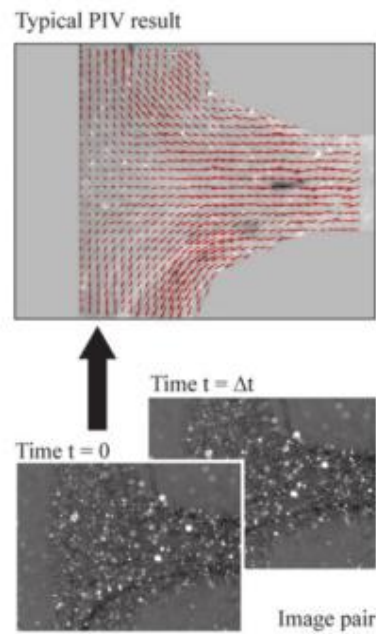
Fig.1.10. Exemplary image pair from flow in curved T-joint with corresponding velocity field in PTV method. (AHD, TU Delft, inc.).

b. Correlation-based PIV

In contrast to PTV, correlation-based PIV does not need to match individual images belonging to a pair. Rather than determining the displacement of individual particles, this PIV algorithm determines the average motion of small groups of particles. Essentially, the overall flow field is divided into a series of interrogation spots, and the correlation function is computed sequentially over all spots resulting in a displacement vector corresponding to each spot in Fig.1.11[40]. The process of averaging over multiple particle pairs within an interrogation spot makes correlation-based PIV remarkably more noise-tolerant and robust than PTV.
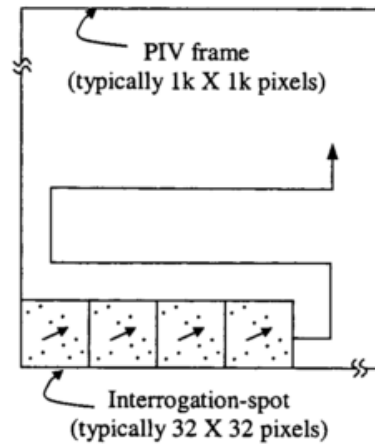
Fig.1.11. Correlation-based PIV process in a 32×32 pixel interrogation spot system, plotting the flow vectors[40].

1.2.3. Recent achievements

Since 21st century, PIV or μPIV has been applied to all the fluidic domains. Current applications includes: near-wall region velocity gradients characterization to study the shear-induced migration of particles and liquid-solid interactions [51], [52]; electrokinetic phenomenon study [53], [54]; gas-liquid or liquid-liquid two-phase mixing characterization [50], [55]–[57], etc... Lindken et al. developed a stereo-microscopic μPIV technique, by which one can determine the 3D flow field in a two-phase fluidic system. The technique has been successfully applied to a passive T-joint geometry (Fig. 1.12) at Re =120 for the reconstruction of the entire stationary volumetric flow field.
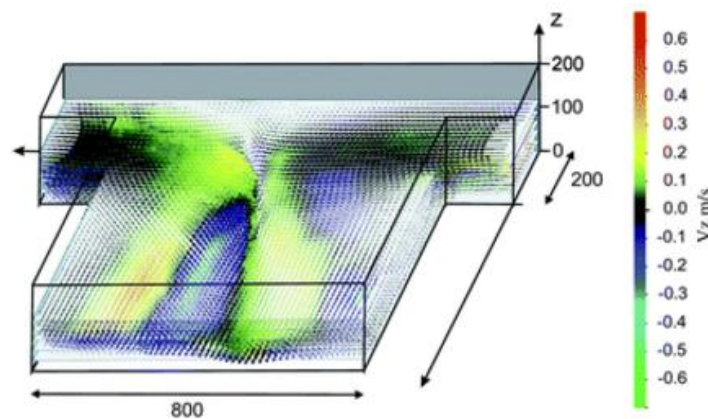
Fig.1.12. 3D reconstruction of the flow field in a micro-scale T-joint mixer where the flow is laminar (Re = 120) assessed by μPIV measurement. The z direction velocity component is color-coded represented[50].

16

1.2.4. Biological applications

A large portion of microfluidic applications of PIV is connected with biomedical measurements. Numerous related works have been proposed. First well-established biomedical application aspect is in-vivo blood velocimetry. Vennemann et al.[2] successfully measured blood velocity distribution in the developing ventricle of a chicken embryo (Fig.1.13). Using an intravital microscope and a high-speed digital imaging system, Sugii et al. [58] presented the measurement of red blood cell velocity distribution in arteriole in a rat mesentery. Hove et al. [59] measured blood velocities field in a zebra-fish. Jeong et al. [60] implemented the movement of liposomes suspended in blood flowing through rat mesenteric capillaries. Besides in-vivo experiments, μPIV has been widely used in in-vitro measurement investigation. Wong et al. [61]measured the velocity profile and extensional rate of the solvent flow in a microfluidic device for DNA molecules deformation. An in vitro model equipped with a side-view μPIV system was proposed by Leyton-Mange et al. [62] to obtain quantitative flow data over cells adhering to the endothelium. Gemmell et al. [63] presented PIV imaging ability to observe detailed kinematics simultaneously with fluid motion around free-swimming zooplankton. They work successfully exploited the important ocean processes governed by small-scale animal-fluid interactions.
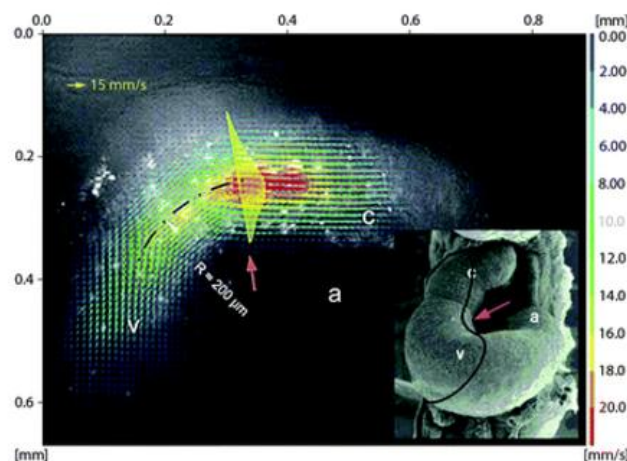
Fig.1.13. Blood velocity distribution in the developing ventricle of a chicken embryo after three days of incubation[2]
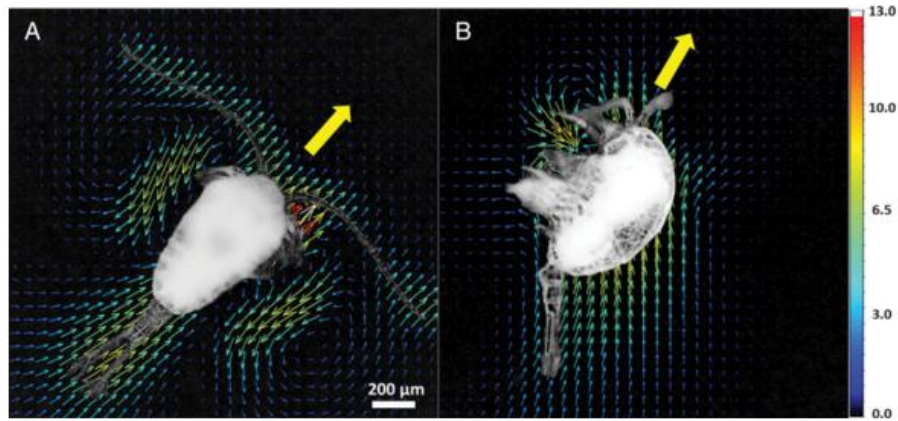
Fig.1.14. Velocity vectors generated by an adult Temora turbinata copepod during normal cruising. (A) dorsal view; (B) lateral view of copepod traveling with a mean swimming speed of 8.5 mm/s. Yellow arrows indicate swimming direction[63].

PIV or μPIV as one of the most advanced flow sensing techniques are extensively used in microfluidics. They allow the determination of velocity magnitude and direction with good spatial resolution. High frame rate or high imaging speed enables a satisfying temporal resolution as well in PIV systems. However, the bulky systems and expensive cameras limit such sensors to in-lab measurements rather than for industrial applications. Same as LDV, PIV is difficult to be integrated in embedded systems.

1.3. Optical feedback interferometry velocimetry

As a new method for the measurements of metrology, optical feedback interferometry (OFI), also known as self-mixing interferometry (SMI), is an interferometric scheme that can be seen as an evolution of the LDV.

This novel technique is based on laser feedback effect, which was first considered as a noise or laser disturbance source. Just after the invention of the laser in 1960 [64], an unwanted resonant laser mode due to the feedback from a third external mirror was observed [65]. In 1963, Steward reported the first use of the feedback effect for metrology applications [66]. Since then, feedback has been widely applied to all types of lasers, for example, solid-state lasers, fiber lasers, terahertz quantum cascade lasers (THz QCLs)[67]–[72].

In contrast to methods that employ the laser as the source and an optical interferometer to split and recombine the beam, OFI is based on the interaction of the laser cavity field with the field backscattered or reflected from the target. This technique has been implemented in many instrumentations works such as vibrometry, displacement measurement,…[11], [73]–[80].

1.3.1. History

In the last several decades, optical feedback has been used as an alternative tool allowing precise measurements of flowing velocity or volume flow rate. De Mul et al. [81] for the first time, measured the flow velocity with an OFI flow sensor. As shown in Fig.1.15, the instrument consists of a laser diode with a photodiode at the back facet, and the laser beam is pointed in a human fingertip. By calculating the ratio between the second and zeroth moment of the OFI spectra, the blood flowing velocity was detected. Moreover, human heartbeat frequency and blood perfusion in human fingertip were successfully measured using the same system, proving the capacity of OFI flowmeter in blood flow diagnosis. Since then, OFI flow sensors have been more and more implemented in biomedical engineering.
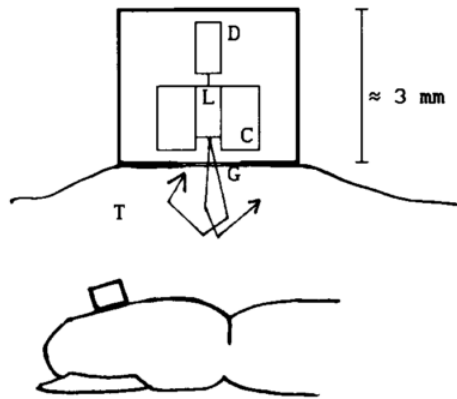
Fig.1.15. Experimental setup of microvessel blood flow measurement by Mul et al [81]. L: the laser, D: photodiode; C:cooling block; G: glass cover; T: a tissue of fingertip.

1.3.2. Sensing principle

As shown in Fig.1.16, when the laser beam is pointed to the seed particles flowing in a fluid. Light scattered by those tracer particles enters back in the laser and modulate its

lasing properties amongst which the output power [9] or the junction voltage [10] are the most widely used for sensing applications.
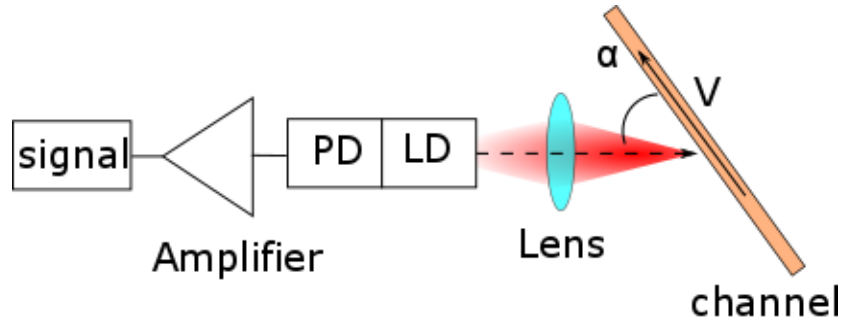
Fig.1.16. Schematic of a typical OFI flowmeter. The laser axis and the velocity vector are at an angle α; the amplified photodiode current is the OFI signal.

1.3.3. Recent achievements

During the last two decades, OFI has been widely applied to many fluid velocity sensing problems.

One of major OFI flowmeter applications is flowing velocity distribution reconstruction. Rovati et al.[82] for the first time implemented the velocity distribution reconstruction in multiple scattering regime inside a circular channel of a 12 mm diameter using an OFI sensor using a low-cost superluminescent diode. Campagnolo et al. successfully accurately measured the velocity profile inside a microchannel (320μm diameter) by means of OFI. The system was validated by extracting the flow profiles in both Newtonian and shear-thinning liquids, with a relative error smaller than 1.8% [83]. The previously mentioned velocity profile works are point-wise measurement, the sensor is driven by 2D stage. Thanks to the outstanding circular beam output of VCSEL, Lim et al. demonstrated a parallel readout OFI flow sensor based on a 1×12 VCSELs array, enabling high frame-rate and resolution full-field imaging systems [84] (Fig. 1.17). Nowadays, OFI-based velocity distribution measurement has been applied in a multi-phase system as well. Ramírez Miquet et al. [85] proposed OFI system for the analysis of the velocity distribution of parallel oil and water dual-phase fluidic system. The

experimental results exhibited good agreement with the theoretical results, providing a new tool for studying more complex interactions between immiscible fluids (Fig. 1.18).
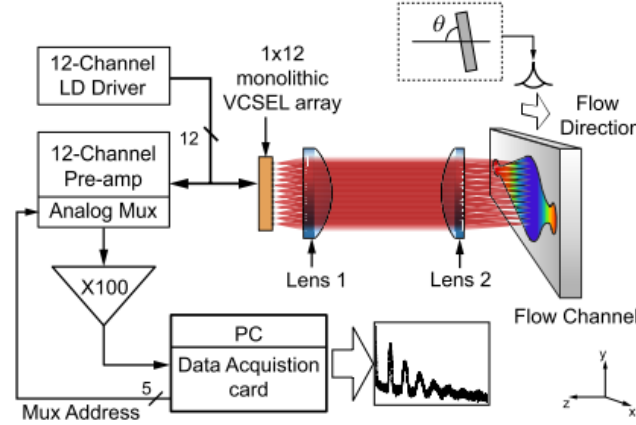
Fig.1.17. Schematic diagram of the flow measurement system based on a monolithic VCSEL array[84].
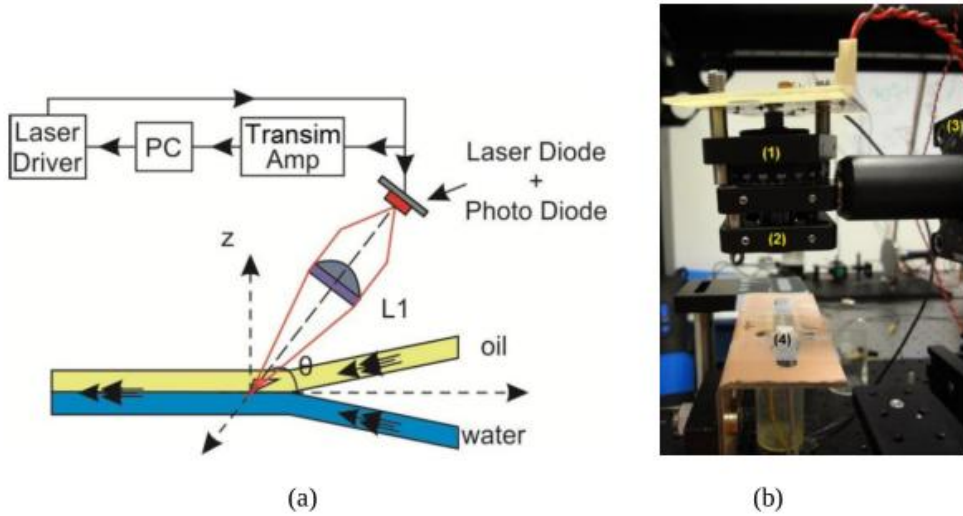
Fig.1.18. Set-up configuration of optical feedback velocity measurement of parallel oil-water flows[85]. (a) The schematic of the setup. (b) Photograph of the set-up: (1) laser(2) Lens, (3) Goniometer and (4) SU8 Y-shaped micro-reactor.

During the OFI-based flowmeter development, much effort has been made as well to improve OFI flowmetry capability in different aspects for fluidic measurements.

To enlarge the available flowing velocity measuring range, Kliese et al reported an OFI flow sensor based on a GaN blue ray semiconductor laser measuring an extremely low

flow rates down to 26μm/s which is not possible using near-infrared laser diodes [86]. To approach higher SNR, Contreras et al. presented an edge-filter enhanced OFI anemometry system (Fig.1.19). They utilized an acetylene edge-filter translating the Doppler frequency modulation of semiconductor laser into an intensity modulation as the laser wavelength is tuned to the steep edge of the absorption profile. They measured the flowing velocity of the aerosol particles of different sizes from 1μm to 10μm at a distance of 2.5 m. Their system yielded to about two orders of magnitude larger signal-to-noise ratio (SNR) than the typical OFI sensor [87].
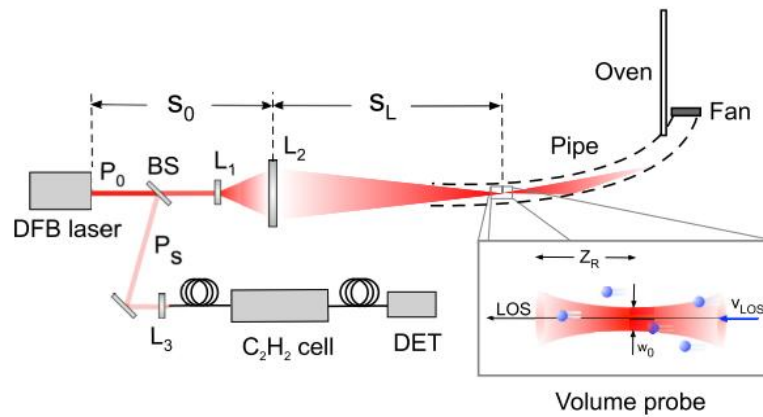
Fig.1.19. Experimental setup for edge filter enhanced OFI experiments[87].

1.3.4. Biomedical applications

Because of the increasing early diagnosis requirements, OFI has been extensively applied in blood flowmetry and skin cancer detection.

For blood monitoring measurements, Ozdemir et al. succeeded in validating the OFI capability of non-invasively measuring blood flow on the skin for assessment of scars and injuries on the skin [88]–[90]. They applied blood flowmeter system based on the optical feedback speckle interferometer to vitro and in-vivo blood flow measurement (as shown in Fig.1.20). Mul et al. [91] presented an OFI velocimetry of outstanding stability and SNR with the optical glass fiber inserted in the artery. Norgia et al.[92] presented both the theoretical and experimental studies of extracorporeal blood flowing velocity measurement in a 9mm diameter pipe. Figueiras et al. [93] evaluated the blood perfusion of local cerebral blood flow in rat brain by OFI sensor. Three different signal processing methods were compared and operated in the measurements. Reasonable

results proved OFI can be an alternative to monitoring local blood flow changes in the rat brain.

For other biomedical aims, Quotb et al. [94] proposed a new OFI based pressure myograph systems (Fig.1.21). Their work can be used for the study of pharmacological effects of drugs and other vasoactive compounds on small isolated vessels. Mowla et al. [95] proposed a new approach to measure confocal reflectance and the Doppler flowmetry signal simultaneously in a confocal OFI sensor system. This results in a new imaging technique of simultaneous probing for two abnormal cancer biological traits of distorted tissue optical properties and perfusion. They have examined this technique through a range of numerical simulations and conducted an experiment to image a dynamic turbid medium.

OFI has been an emerging strategy in biomedical diagnosis due to its self-aligned, compacity and simplicity. However, the existing OFI-based flowmeter systems still consist of bulk optical arrangement. This limits the OFI technique application in embedded system systems. Considering great interest of compact embedded systems and importance of flowing monitoring, an integrated OFI-based flow meter system discarding bulk optical components and assembling directly with the laser and the microfluidic circuits is desired.
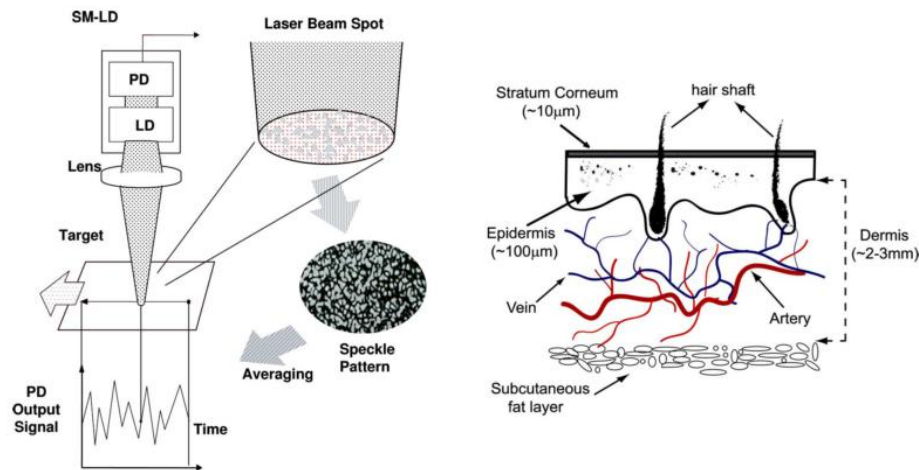
Fig.1.20. Schematics of (left) optical feedback speckle interferometry[90] and (right) the layers of human skin.
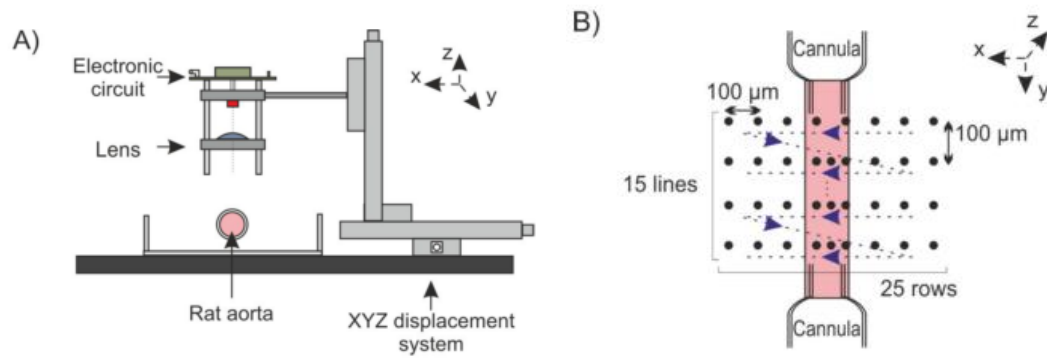
Fig.1.21. OFI based myograph system: A) Lateral view of setup. B) Top view of the aorta scanning[94].

1.4. Comparison and conclusion

Tab1.1 summarizes the three methods presented in this chapter, comparing the cost, spatial resolution, compacity, and feasibility in the embedded system.

Tab. 1.1.Comparison of the mentioned methods for flow measurements.

Methods	Resolution	Compacity	Costs	Feasibility in an embedded system
LDV	650nm	No	high	No
PIV	<100nm	No	high	No
OFI	~10μm	Yes	low	Yes

As shown in this table, the key features of each technique presented in this chapter are outlined:

Dual-beam LDV provides very high spatial resolution (up to 65nm [9]) thanks to a sensing volume defined by the intersection of the two incident beams. However, the need of tricky alignment for interference fringes production increases dramatically its complexity and cost, making it quite difficult to be applied to small embedded systems.

PIV allows the full-field determination of velocities at high accuracy all over the interesting flow region. Contrary to LDV or OFI, it can determine also local flow

direction. However, the use of bulky and expensive cameras system limits the price and portability in out-lab usage and embedded systems.

OFI is capable of high performance with an extremely simple and inexpensive experimental setup. The laser source also plays the role of the detector, making this technique self-aligned, compact and robust. Many applications require the manipulation of fluid, tending towards always smaller volume handling with precise flow and concentration control.

The compacity and simplicity advantages make OFI structure-friendly to usage for the embedded system applications. Due to the self-aligned property, OFI flowmetry sensor can therefore be easily investigated in a small fluidic platform. However, to our knowledge only a few established OFI based flow sensors in embedded fluidic system have been reported [20], thereby exploring OFI potential in such direction is of great interest and applied value in biomedical domain.

Throughout this thesis, we propose to evaluate optical feedback interferometry sensors capability in a microfluidic system, using in particular VCSEL compact laser sources. The simulations and experiments demonstrations are presented here to emphasize the potential of this technique as an alternative microfluidics. In next chapter, theoretical aspects are first discussed.

2 OFI signal modeling in microfluidic measurements based on multi-physics numerical simulation methods

2.1. Introduction

Considerable development of OFI flowmetry or anemometry sensors has been achieved since the last decades, various related research has been reported on this topic deploying channels with dimensions ranging from ten microns to several millimeters [96], [97]. In OFI flowmetry, the Doppler frequency shift imparted to the scattered light from the flowing tracers suspended in the channel is detected.

However, most of the OFI fluidic sensors concern millimeter scales systems, while only a few of them are treating micro-scale configurations. OFI-based microfluidic flowmeter sensor study remains indeed challenging because of many practical problems, especially with systems of dimension smaller than 100 μm.

First, when the laser is pointing onto the microchannel, a lot of particles with different velocities scatter the laser light back to the laser cavity and each of them contributes to the OFI signal with its own Doppler frequency shift. Thus it results in a complex signal with a continuous frequency spectrum.

Second, the scattered light power is very weak, thus the OFI signal is easily submerged in the noise.

Third, due to the extremely small size and construction complexity, the influences on the OFI signal of the optics and fluidic structure (e.g., reflection or interference occurring in the channel structure) have to be taken into account, as the laser beam suffers from various perturbations during the incident and backward propagation.

In order to improve the understanding and the design of future microfluidic devices by means of a more optimized OFI sensor in microfluidic measurement, a novel simulation method is presented here for prediction of the OFI signal in a micro-scale fluidic system. The modeling approach is based on the combination of four different aspects involved in the sensing method. First, based on the existing three-mirrors cavity (or "compound cavity") model describing the behavior of a laser diode under optical feedback from a translating target, a novel modeling is proposed that predicts the laser diode behavior in the case where feedback occurs from multiple scatterers. Second, in order to evaluate the feedback power strength from the tracing particles, their scattering behavior under illumination by a Gaussian beam is investigated theoretically. Third, using the commercial ray tracing software ZEMAX, the laser beam propagation inside the micro-scale reactor is simulated and both the laser illumination and collection of scattered light re-entering the laser diode (feedback light) are estimated by a Monte Carlo method. Thus it provides a complete analysis on how the reactor structure impacts the laser beam propagation. Using the commercial computational fluid dynamics (CFD) software Fluent, the 3D flowing velocity profile in the channel is plotted to reproduce the Doppler frequency spectrum. The simulation results are presented and discussed. Eventually, more aspects are taken into account in the model such as scattered light angular distribution and the particle concentration making our simulation more alike to reality.

Laser diodes behavior under feedback modulation has been well documented from the theoretical viewpoint. Lang and Kobayashi reported a basic but capable theoretical model to explain the laser dynamics in presence of feedback[98]. In their work, they showed the dynamical change of carrier density in semiconductor laser in presence of optical feedback. In spite of many approximations and assumptions applied in it, this basic model is remarkably appropriate for a wide range of lasers, predicting a great deal of complex behaviour that has been observed in practice. Most of the theoretical models presented in the literature are based on the Lang-Kobayashi equations[99], [100]. In 1988, Petermann proposed a three-mirror model [101] as an alternative to describe the laser diode behavior. He classified the feedback regions by the feedback strength and explained the feedback signal shapes in different regimes. De Groot et al. [102]

developed a theoretical model based on a three-mirror Fabry-Pérot cavity to explain OFI signal generation in OFI velocimetry and ranging.

One of the important outcome of these modeling is that OFI equations are in first approximation independent of the laser nature and OFI for sensing applications has been actually observed for many types of laser sources: from gas laser[103] to Quantum cascade lasers (QCLs)[71] and of course in all sorts of laser diodes from the basic Fabry-Pérot, to DFB or VCSELs. In the context of this thesis, targeting embedded sensing and lab-on-chip systems based on microlens integrated on VCSELs, we have decided to limit our modeling effort to VCSEL type devices.

Thanks to their vertical geometry leading to many specific advantages such as circular beam emission, ease of testing on wafer, parallel operation and extremely low current consumption, VCSELs (Vertical-Cavity Surface-Emitting Lasers) are nowadays strategic beam sources for an increasing range of applications, including short-distance data communications [104] optical mice [105], sensors particularly by OFI methods [106], laser trapping [107]and optical probe microscopy [108]. On the other hand, since the 1990s, LoC (Lab-on-Chip) biosensors have attracted increasing attention, and many related micro-optical systems based on VCSELs have been devoted to such topic [109], [110]. Among these works, VCSEL-based OFI velocimetry sensors implementations have been widely developed in the last two decades [84], [111]–[115], taking advantage of VCSELs features. In particular, detection capabilities of VCSELs diodes (thanks to an associated or integrated photodiode [116] or simply owing to the direct junction voltage measurement) is of great interest for OFI sensors considering their low power consumption as well as the possibility of designing arrays of interferometric sensors with high integration density with monolithic VCSEL arrays [116]

In this thesis two different types of GaAs-based VCSELs have been both tested and simulated: in chapter 2 and Chapter 3 a VCSEL emitting at 670 nm purchased at Optowell and several 850 nm Philips Photonics. The Optowell device was initially chosen because it was sold with a photodetector mounted in the laser package thus ensuring the best configuration for high signal-to-noise ratio in sensing conditions. 850nm is the standard working wavelength of devices studied by LAAS and the Philips Photonics devices were chosen because thanks to the long-term collaboration with this

company, unmounted and reproducible devices were available thus allowing for micro-lenses deposition.

The behavioral model of the VCSEL under optical feedback we have used here is limited to a transverse and longitudinal singlemode emission, without taking into consideration the light polarization aspects.

In the thesis manuscript, on the basis of Petermann's three-mirror cavity model, we develop a new model to describe the laser output power fluctuation in microfluidic context. The model is constructed as follows:

First, in subsection 2.2, the equivalent cavity is demonstrated in presence of a distant target, which interprets the laser diode behaviors including phase and oscillation frequency.

Second, in subsection 2.3, the laser diode output power expressions imparted by the feedback frequency modulation from both single translating target and multiple targets are formulated.

At last in subsection 2.7 and 2.8, a complete model involving scattered light angular distribution and particle concentration is developed and discussed.

2.2. OFI theoretical fundamentals

2.2.1. Free-running laser modeling

The laser Fabry-Pérotcavity (Fig. 2.1) consists of an active medium of length L_c, bounded by two interfaces *M1* and *M2*. The field amplitude reflection coefficients are r_1 and r_2, respectively.
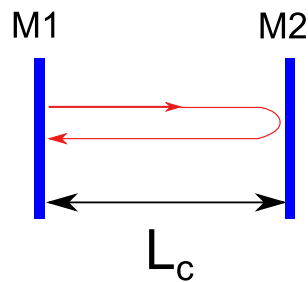
Fig.2.1. Schematic of the laser diode cavity.

The laser beam propagating from left to right (z direction) inside the cavity can be expressed as:

$$E(z) = E_o \exp(-jk_0 z) \exp(-\frac{1}{2}\gamma_0 z) \qquad (2.1)$$

with

$$k_0 = \frac{2\pi}{\lambda} \ , \ \lambda = \frac{c}{n_{eff} v_0} \qquad (2.2)$$

where n_{eff} represents the effective refractive index of the active medium, γ_0 is the propagation loss factor in the cavity, v_0 is the frequency of the wave and c the speed of light in vacuum.

In eq(2.1), the term in the first exponential term represents the wave propagation and the second exponential describes the losses during the propagation. The laser "self-consistency" property and lasing condition require that after a round-trip propagation through the laser cavity of length L_c, the new electric field E_1 should be identical in phase and amplitude with the initial value E_0. This implies that the phase shift between E_0 and E_1 should be a multiple integer M of 2π. The laser frequency v_0 values are delimited as a discrete series:

$$E_1 = E_0 r_1 \exp(-jk_0 L_c - \frac{1}{2}\gamma_0 L_c) r_2 \exp(-jk_0 L_c - \frac{1}{2}\gamma_0 L_c) \qquad (2.3)$$

Yielding,

$$r_1 r_2 \exp(-2jk_0 L_c)\exp(-\gamma_0 L_c) = 1 \qquad (2.4)$$

and

$$v_0 = \frac{Mc}{2L_c n_{eff}}, \text{ with } M = 1,2,3... \qquad (2.5)$$

2.2.2. Equivalent cavity in the presence of an external target

In the presence of a distant target, the free-running model described above can be extended to a three mirror model in Fig. 2.2 with an external cavity of length L_{ext} induced by the external target. r_{ext} is the ratio of the scattered light electric field amplitude re-entering the laser cavity over the initial laser output electric field. Since the target is a scattering particle in our case, the beam path propagation and the optical attenuation through the round trip are taken account in r_{ext}.

The three-mirror cavity system can be reduced to a single cavity as depicted in Fig.2.1 keeping the laser cavity length L_c but replacing the reflectivity coefficient r_2 by a new complex equivalent amplitude reflectivity r_{eq}.
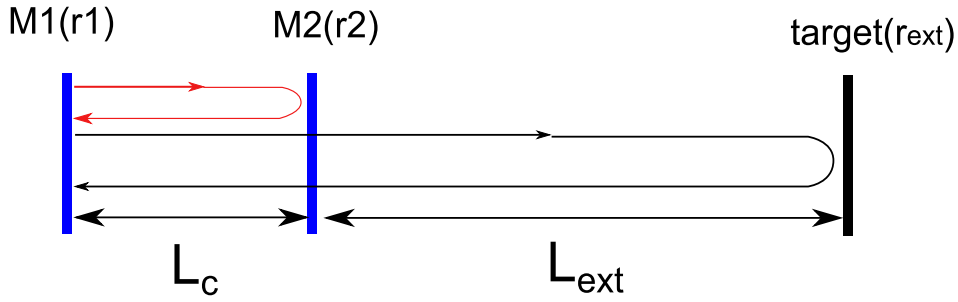
Fig.2.2. Schematic of the three-mirror cavity of a laser diode in the presence of an external target.

When $r_{ext} \ll r_2$, the multi-reflection round trips from the external cavity can be neglected [117], yielding the expression of the equivalent reflectivity r_{eq} to be a function of the laser frequency in the following form:

$$r_{eq} = r_2[1 + \xi \exp(-j2\pi\nu_f \tau_d)] \tag{2.6}$$

with

$$\xi = \frac{r_{ext}(1 - r_2^2)}{r_2} \tag{2.7}$$

where, ν_f denotes the stable laser frequency in the presence of the target, and τ_d is the external round-trip delay time within the external cavity of refractive index n.

$$\tau_d = \frac{2nL_{ext}}{c} \tag{2.8}$$

The phase change in the external cavity round trip $\Delta\Phi$ can be expressed in the well-established form as[118]:

$$\Delta\Phi = v_f - v_0 + \frac{C}{2\pi\tau_d}\sin\left(2\pi v_f \tau_d + \arctan\alpha\right) \tag{2.9}$$

with

$$C = \xi\frac{\tau_d}{\tau_l}\sqrt{1+\alpha^2} \tag{2.10}$$

where C is feedback parameter, which describes the strength of the changes due to optical feedback in changing the intrinsic behavior of the laser. α is the linewidth enhancement factor defined as the ratio of the change in the real part of the laser medium refractive index to the change in the imaginary part of the laser media refractive index[119], and τ_l denotes the round trip time in the laser cavity:

$$\tau_l = \frac{2n_{eff}L_c}{c} \tag{2.11}$$

To satisfy a laser stationary operation condition, the phase change should be zero or an integer multiple of 2π. Neglecting the multiple round trips in the external cavity, the expression of the laser frequency v_f can be written as:

$$v_f = v_0 - \frac{C}{2\pi\tau_d}\sin\left(2\pi v_f \tau_d + \arctan\alpha\right) \tag{2.12}$$

Besides the investigation of the laser frequency under feedback, the laser output power behaviour is also studied in detail. Lang-Kobayashi equations are employed here to describe the carrier dynamics of the semiconductor laser subject to optical feedback effects[75], [81], [98]. These detailed rate equations in laser diode can be written as:

$$\frac{dE}{dt} = \frac{1}{2}[G_N(N_c - N_0) - \frac{1}{\tau_p}]E + \frac{\xi}{\tau_d}\cos[2\pi v_f t + \Phi(t) - \Phi(t-\tau_d)] \tag{2.13}$$

$$\frac{dN_c}{dt} = \frac{J\eta}{e\Lambda} - \frac{N_c}{\tau_c} - G_N(N_c - N_0)E_0{}^2(t) \qquad (2.14)$$

Where G_N is the laser gain factor, N_c is the carrier density, N_0 is the inversion carrier density, N_{th} is the threshold carrier density, τ_p is the photon lifetime, τ_c is the carrier lifetime, η is the internal quantum efficiency, J is the pumping current density, Λ is the active layer thickness, and e is the electron charge.

Eq(2.13-14) investigate the carrier dynamic inside the laser diode in detail, often used for description of the feedback phenomena in semiconductor lasers.

Now let's link the laser output power performance to the injection current. The threshold current I_{th} of a semiconductor laser is the injected current at which the gain in the cavity becomes equal to the loss inside the cavity. Therefore, once the gain reaches the threshold gain, lasing starts to occur. The dependence of threshold gain deviation Δg_{th} on feedback can be expressed as in eq(2.15)[120]. Thus, the threshold current variation ΔI_{th} may be obtained from the Δg_{th}:

$$\Delta g_{th} = g_{th}{}' - g_{th} = -\frac{\xi}{L_{ext}}\cos(2\pi v_f \tau_d) \qquad (2.15)$$

$$\Delta I_{th} = \frac{eV_m}{T_s \kappa \Gamma}\Delta g_{th} \qquad (2.16)$$

Where g_{th} is the original threshold gain without feedback and g_{th}' is the new value under feedback. V_m is the active medium volume in the laser cavity, T_s is the spontaneous recombination rate, κ is the differential gain at the threshold, and Γ is the mode confinement factor.

The output power under feedback P_f can be obtained from the operating current I [121]:

$$P_f = \frac{\eta hv\left[I - (I_{th} + \Delta I_{th})\right]}{e} \qquad (2.17)$$

Yielding,

$$P_f = \frac{\eta hv(I - I_{th})}{e}\left[1 + \frac{eV\xi}{T_s \kappa \Gamma L_{ext}(I - I_{th})}\cos(2\pi v_f \tau_d)\right] \qquad (2.18)$$

Where h is the Planck's constant.

eq(2.18) can be simplified as in the literature[74]

$$P_f = P_0[1 + m\cos(2\pi v_f \tau_d)]$$
(2.19)

Considering eq(2.10), yielding:

$$m = C\frac{2\tau_p c}{L_{ext}\sqrt{1+\alpha^2}} = 4\xi\frac{\tau_p}{\tau_l}$$
(2.20)

m is feedback factor for feedback strength regime classification. .

In the microfluidic measurements, the scattered light power from the tiny seeding particles is so weak that the OFI flowmetry sensors in microfluidic measurements normally operate in the weak feedback regime.

2.2.3. Laser diode OFI behavior for a single translating target

When a target is a translating object, i.e., it does not move towards or away from the laser, the complex reflectivity r_{eq} will be modulated by the Doppler frequency shift due to the translating velocity:

$$r_{eq} = r_2[1 + \xi\exp(-j2\pi f_D t + \Phi_D)]$$
(2.21)

Where Φ_D is the phase difference resulting from the round trip through the external cavity:

$$\Phi_D = 2\pi\left(v_f + f_D\right)\tau_d$$
(2.22)

The Doppler frequency f_D is proportional to the scalar product of the vector difference

$\vec{k} = \overrightarrow{k_{sca}} - \overrightarrow{k_{inc}}$ and the velocity vector $\vec{V}$:

$$f_D = \left|\frac{\vec{k}\cdot\vec{V}}{2\pi}\right|$$
(2.23)

We assumed that scattered light propagates straightly backward with respect to the incident light, namely $\overrightarrow{k_{sca}} = -\overrightarrow{k_{inc}}$

yielding,

$$\left|\vec{k}\right| = 2\left|\overrightarrow{k_{inc}}\right| \tag{2.24}$$

$$f_D = \left|\frac{\vec{k} \cdot \vec{V}}{2\pi}\right| = \frac{2V \sin \theta_{inc}}{\lambda} \tag{2.25}$$

and

$$P_f = P_0[1 + m\cos(2\pi f_D t)] \tag{2.26}$$

where P_0 is the initial unperturbed laser output power and m the modulation index as described in (2.20). Apart from the laser output power P_f, the laser junction voltage variation ΔV is also related to the feedback modulation as in eq(2.27) :

$$\Delta V = -\chi \cdot \cos(2\pi f_D t) \tag{2.27}$$

where χ is a constant depending on the laser operating temperature.

Thus we can monitor junction voltage fluctuations of the laser diode even without the photodiode embedded in the laser package to simplify the sensor system [72], [122], [123]. In Chapter 4, the junction voltage measurement is applied to all our measurements.

2.2.4. Laser diode OFI behavior with multiple translating scatterers

In the flow measurement, the optical system collects the scattered light from a large amount of particles (scatterers) with various velocities as indicated in Fig.2.3. This induces a distribution of the Doppler frequency shifts that impact the LD output power fluctuation.
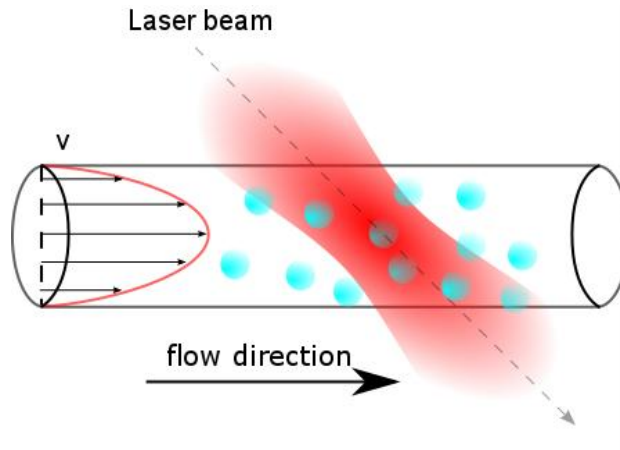
Fig.2.3.Schematic of OFI sensor applied to flow measurement. Various flowing particles of different velocities passing through the laser beam induce feedback signal.

2.2.5. Single scattering regime

In most fluidic sensing measurements, when the adjacent particles are sufficiently far from each other, single or independent scattering can occur. Thus, each photon is scattered by only one particle during its propagation from and back to the laser. The scattered light contributes to the Doppler frequency shift with the information of the unique scatterer particle's velocity. Many publications have been reported to identify the particle concentration limitation in single scattering regime[124], [125].

When the concentration of scatterers is high, the photons experience multiple laser-particle interactions which induce several Doppler shifts in the solution. We call this phenomenon as multiple scattering regime compared with single scattering regime. In this regime, the OFI output power signal is really random and the frequency distribution performs a complex random behavior.

Majority of the existing theoretical works are limited to flow sensing in the single scattering regime and neglecting the multiple scattering effects. In our flowing context, we assume the OFI system operates in single scattering regime.

2.2.6. Laser diode OFI behavior with multiple translating scatterers

To predict the OFI sensor behavior in fluidic measurement, a new model of OFI output fluctuation is depicted in Fig.2.4. This model is developed based on previous three-mirror cavity theory in subsection 2.2.
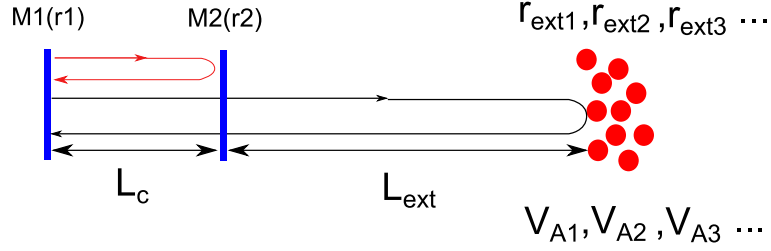

Fig.2.4. Three-mirror cavity when the target is a group of small particles.

In single scattering regime, we can calculate the equivalent cavity reflectivity r_{eq}' by summing up all the back-scattered contributions from each particle:

$$r_{eq}' = r_2[1 + (1 - r_2^2)\sum_i \frac{r_{exti}}{r_2}\exp(j2\pi f_{Di}t + j\Phi_{Di})] \tag{2.28}$$

$$f_{Di} = \frac{2V_i \sin\theta_{inc}}{\lambda} , \Phi_{Di} = 2\pi(\nu_{fi} + f_{Di})\tau_d \tag{2.29}$$

$$\|r_{eq}\| = r_2\sqrt{(1 + \sum_i \xi_i \cos(2\pi f_{Di}t + \Phi_{Di}))^2 + (\sum_i \xi_i \sin(2\pi f_{Di}t + \Phi_{Di}))^2}$$

$$= r_2\sqrt{\begin{aligned}&1 + 2\sum_i \xi_i \cos(2\pi f_{Di}t + \Phi_{Di}) + (\sum_i \xi_i \cos(2\pi f_{Di}t + \Phi_{Di}))^2\\&+ (\sum_i \xi_i \sin(2\pi f_{Di}t + \Phi_{Di}))^2\end{aligned}} \tag{2.30}$$

$$\xi_i = \frac{r_{exti}(1 - r_2^2)}{r_2} \tag{2.31}$$

Considering $\xi_i \ll 1$, we can obtain:

$$\xi_i \cos(\omega_{Di}t + \Phi_{Di}) \ll 1, \ \xi_i \sin(\omega_{Di}t + \Phi_{Di}) \ll 1 \tag{2.32}$$

So the third and fourth terms in the square root can be neglected, and the absolute value of the equivalent reflectivity can be derived as:

$$\left\| r_{eq} \right\| = r_2 \sqrt{1 + 2\sum_i \xi_i \cos(2\pi f_{Di} t + \Phi_{Di})} \tag{2.33}$$

The new modified P_{OFI}' from different scattering particles can be expressed as:

$$P_f = P_0 [1 + \sum_i m_i \cos(2\pi f_{Di} t + \Phi_{D_i})] \tag{2.34}$$

From eq(2.34), it can be concluded that in a fluidic system, the laser output power P_{OFI}' is determined by m_i and $f_{D,i}$ which are related respectively to the feedback light amplitude ratio of each particle $r_{ext,i}$ and the velocities component in the laser direction $\overrightarrow{V_{A,i}}$ of the ith particle. In the next section, both parameters are investigated through numerical simulation.

2.3. Ray-tracing simulation of OFI system

Modeling a laser-based system by ray tracing software has been treated in previous studies [126], [127]. However, to our knowledge, a Monte Carlo method based simulation of the OFI system has never been published. Here we present the numerical modeling of an OFI microfluidic flowmetry sensor system based on a commercial ray-tracing software Zemax-EE.

First, the 3D model of the whole OFI sensor system (including the laser source, lens arrangement, microfluidic chip and tracer particle) is built in ZEMAX, and then both the laser beam illumination and the feedback propagation through the system are simulated in Monte Carlo analysis methodology. Second, the light scattering behavior of small particles is predicted by the ZEMAX simulation. Third, the feedback light power ratio from different particle positions is computed based on the previous simulation results. This relative ratio profile is depicted in order to be implemented into the laser output power behavior model for OFI signal reproduction.

2.3.1. Setup modeling

In the ray-tracing simulation, the complete optical arrangement has been modeled, including the laser source, the doublet lenses, the microchannel, and the tracing particles. The simulation 3D layout is shown in Fig. 2.5.

The laser source is a commercial VCSEL laser diode (Optowell Co., Ltd) which exhibits good lasing performances at a wavelength of 670 nm with 5° divergence angle (HWHM) and a circular beam with an intrinsic waist diameter at $1/e^2$ of 4.6μm. In the simulation, we define the VCSEL source as a circular surface of the same diameter. This surface is also used to define the light collecting capacity of the sensor: after the laser-particle scattering, only the scattered rays passing through such surface can be coupled inside the cavity, contributing the feedback modulation.
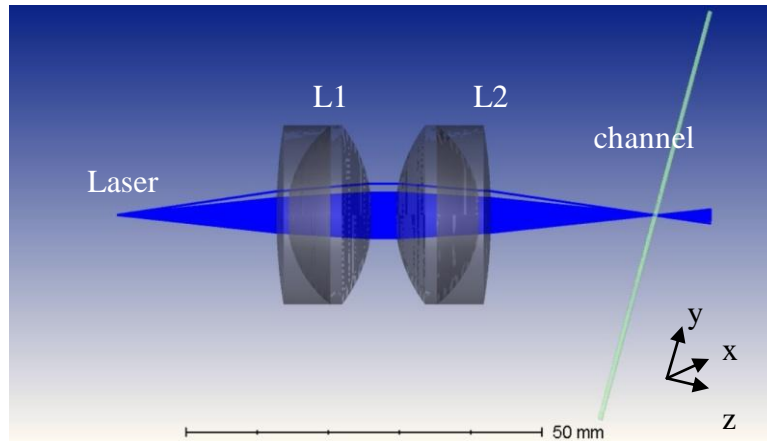

Fig.2.5. 3D layout in ZEMAX simulation of the experimental setup. The system consists of VCSEL considered here as a Gaussian source of diameter 5.8 μm, a doublet lens pair (Thorlabs MAP103030-B) and a SU-8/glass microfluidic channel chip.

Since the scattered light power is proportional to the power density, in order to enhance the feedback signal, high illumination power density is required. Tightly focused incident laser beam to minimize the laser spot area is a good way to increase the power density. Here we use a doublet lens pair constituted by two lenses that have the same focal length of 30 mm (Thorlabs MAP103030-B), so that the imaging magnification ratio is 1:1, the beam waist inside the channel should be of the same diameter (4.6 μm).

A lab-made compact microfluidic chip fabricated by photolithography on SU-8 photoresist is employed here as the fluidic reactor[128]. As shown in Fig.2.6, a SU-8

40

film of 5μm thickness is placed and laminated on the glass wafer as the channel ground floor, 100 μm thick SU-8 layer etched by UV photolithography technique is placed on the first SU-8 film building the channel wall. A 25μm thick SU-8 film is placed as the roof layer above all system. Polystyrene (PS) microspheres (MicroParticles, GmbH) are used as the scattering particles. PS microspheres can be suspended very uniformly in aqueous solution after proper mixing due to their 1.05 g/cm^3 mass density which is similar to water. The solution flows along the Y direction.
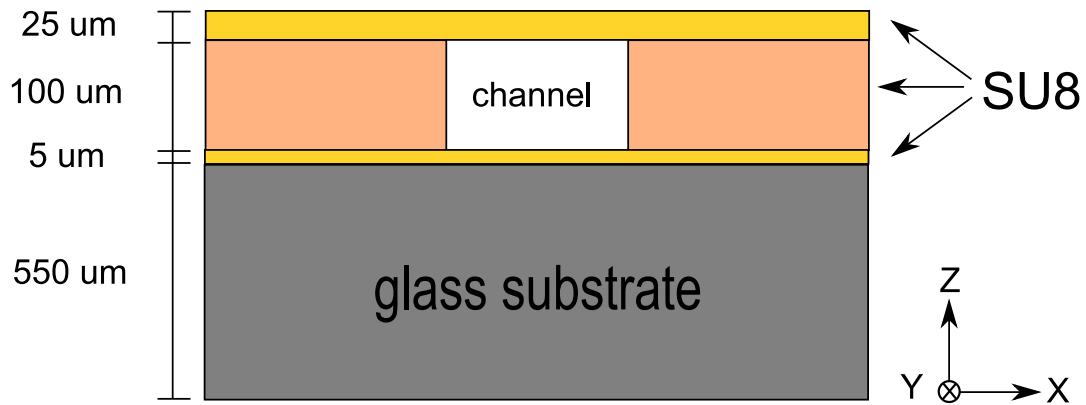
Fig.2.6. Cross-section view of the microfluidic channel chip.

Here in order to make the model more accurate, we choose the non-sequential tracing mode operation for our ray-tracing simulation, in this mode the rays are traced like in the actual physical order they hit various objects or surfaces. All parameters (e.g., geometrical sizes, materials, lens film coatings) are chosen to be in a realistic agreement with the experimental parameters (see Tab 2.1).

Tab.2.1.ZEMAX basic modeling parameters settings.

Simulation parameters	Value
Wavelength	$\lambda = 670$ nm
tracing ray number	$N = 10^6$
Laser output $1/e^2$ radius	$w_0 = 2.3$ μm
Half divergence of laser	$\beta = 5°$
Lens focal length	$f_1 = f_2 = 30$mm
Refractive index of water	$n_0 = 1.33$
Refractive index of SU-8	$n_s = 1.59$
Refractive index of glass substrate	$n_{glass} = 1.51$
particle diameter	$D = 4.89$μm
Refractive index of PS particles	$n = 1.58$

We place the laser source and the channel exactly at the front and back focal plane of the doublet lens making the incident beam focused tightly at the channel center. Fig.2.7 depicts the simulated beam size in the channel center, where a 4.4 μm $1/e^2$ diameter is calculated after Gaussian fitting which is quite coherent with the expected value 4.6 μm.
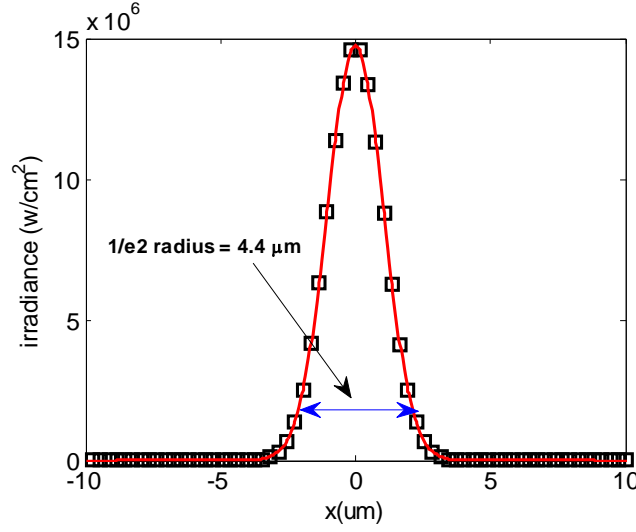
Fig.2.7. Simulated illumination profile at the channel center and beam waist $1/e^2$ diameter estimation by Gaussian fitting.

2.3.2. Feedback power ratio profile

As a very first step, we checked that the ZEMAX algorithm was calculating a well-defined Gaussian irradiant profile in the channel center. To control the focal point position, the incident irradiant 2D profile from a moving detector surface is first simulated. Thus the channel position is set so that the focal point is at the channel center. Then a cuboid mesh (10μm×10μm×100μm) is built in the channel for 3D mapping, the three dimensions grid intervals are set: dx=dy=1 μm, dz=0.5 μm. For each coordinate, a 4.89 μm PS microsphere is placed at the node position and the ray tracing is performed to calculate the scattered light power fraction R_{ext}

$$R_{\text{ext,i}} = \frac{P_{\text{in,i}} - P_{bg}}{P_0} = \frac{P_{\text{back,i}}}{P_0} \tag{2.35}$$

$$r_{ext,i} = \sqrt{R_{\text{ext,i}}} \tag{2.36}$$

where P_0 is the unperturbed average emitted power, $P_{\text{in,i}}$ is the total power measured by the feedback detector, $P_{bg,i}$ is the feedback power without moving scatterers (particles), and thus $P_{back,\text{i}}$ is the power contribution of the ith particle.

The resulting 2D R_{ext} profile in the channel is indicated in Fig. 2.8(a). The width of the 2D R_{ext} profile is approximatively 8 μm, more than the one of the illumination volume

profile. One reasonable explanation is that particles that are partially inside the illumination volume still induce a considerable scattered power contribution so that the particle size impacts the R_{ext} profile.
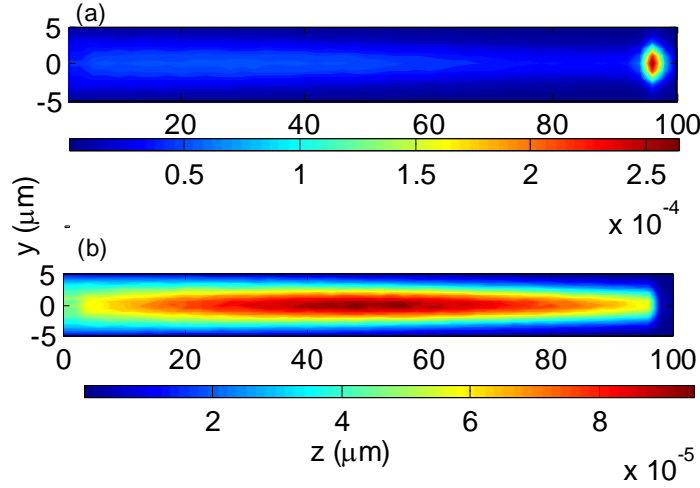

Fig. 2.8. Power fraction of the back-scattered light profile in different particle positions with (a) the actual SU-8 rear interface (b) the case of an absorbing rear interface.

As can be observed in Fig.2.8(a), the reflectivity distribution in the channel shows a maximum at a very short distance from the rear interface. This is the result of the forward scattered power that is in a second time back-scattered by the rear interface.

In Fig. 2.9, the angular distribution of the scattered light intensity from a single particle of diameter 4.89 μm is plotted, the scattered intensity in the forward direction (0°) is more than 10^4 times higher than that the one in the backward direction (180°). Though the reflectivity of the rear interface is very low (less than 1% with Fresnel equations), there is still some forward scattered light reflected on the rear interface. When the particle is close enough from the rear interface, a significant portion of them will re-enter the LD cavity in the same way as the direct back-scattered light. This phenomenon is enhanced by the focusing behavior of the PS spheres that can be described using Debye series decomposition, and the "focal length" is related to the spherical particle diameter.
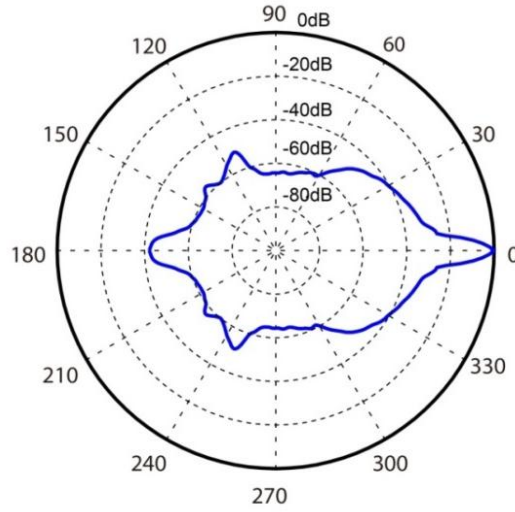
Fig.2.9. Normalized scattered light irradiant profile simulated as a function of scatter angle.

To confirm the impact of the secondary back-scattered light, we have simulated the rear interface as a perfect absorbing medium. The direct back-scattered light from the microsphere is the only light feedback source as can be observed in Fig. 2.8(b).

The simulated reflectivity distribution in this case and along the propagation axis is presented in Fig. 2.10 as well as the one of the actual SU-8 rear interface. In the two hypotheses, a maximum reflectivity position is located at the channel center where the incident irradiance gets its maximal value. In the case of the SU-8 rear interface (solid line), a very visible peak of reflectivity is observed with a maximum for particles center located at a distance of 5 μm from the rear interface. As expected it does not exist with the perfect absorber rear interface (dashed-dotted line).
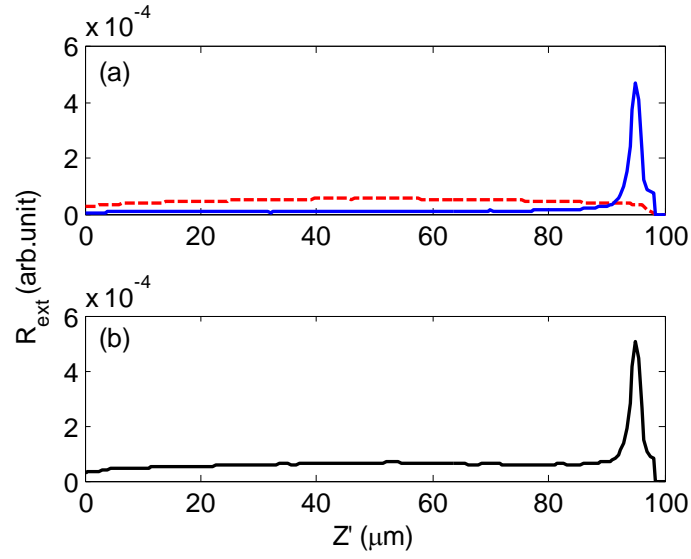
Fig.2.10. Profile of power reflectivity R_{ext} as a function of particle positions along laser emission direction (i.e., Z' direction). (a) The red dashed line and the blue solid curves correspond to the cases only considering the direct back-scattered light and the reflection of the forward scattered light on the rear interface, respectively. (b) The black curve describes the profile in the case of the realistic SU-8 rear interface, where both R_{ext} contributions are taken into account.

2.4. Fluent simulation

Nowadays, computational fluid dynamics methods are well described in many books and applied routinely in microfluidics application, such as lab-on-chip. In this subsection, for OFI signal reproduction considering the velocity variation in a spatial measurement volume, flowing velocity distribution of high accuracy in micro-scale channel is required as well. Here this hydrodynamic phenomenon is conducted with the commercial computational fluid dynamics (CFD) software ANSYS Fluent based on CFD methods.

The 3D modeling of our microfluidic channel is plotted in Fluent as shown in Fig.2.11. After an appropriate mesh building, the node interval is set to be 10μm in 3 dimensions guaranteeing the highest meshing quality.
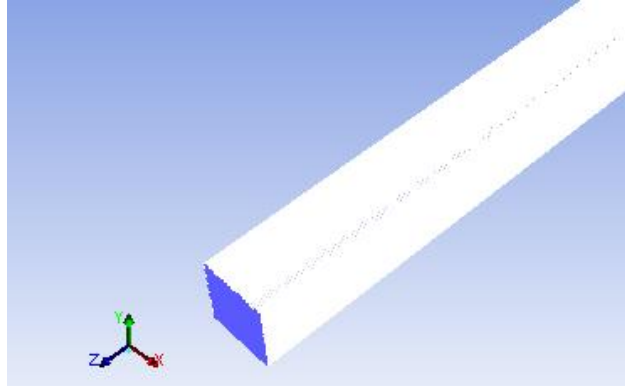
Fig.2.11. 2D modeling and meshing of square SU-8 channel chip in Fluent.

To implement the simulation with our realistic experimental condition, here we set the boundary conditions in simulation as：

First, the flow is in the laminar regime, i.e., the Reynolds number is small, any turbulent case is negligible. Second, the flowing liquid and the channel inner wall are incompressible. Last, considering that a mechanic spring-pressing pump is employed to pump the fluid liquid, the inlet boundary condition is set as constant volume flow rate.

Fig. 2.12 depicts the velocity profile across a 100μm ×100μm square channel when the flow rate is 10μL/min. As expected, the maximum velocity is found at the channel center.
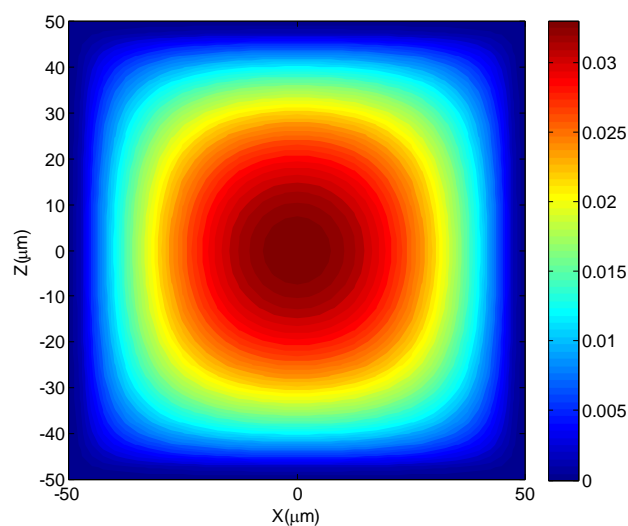
Fig.2.12.2D flowing velocity profile of the cross-section plane in a 100μm×100μm channel when the flow rate equals 10μL/min.

While computing the Fluent algorithm for various flow rates, we can observe that the maximal velocity V_{max} (mm/s) is proportional to the flow rate Q (μL/min). The evolution of the maximum velocity V_{max} as a function of the flow rate can be calculated from eq(2.37)[129].

$$\frac{V_{max}}{\overline{V}} = \frac{3}{2}\left(1 + 0.546688\beta + 1.552013\beta^2 - 4.059427\beta^3 + 3.214927\beta^4 - 0.857313\beta^5\right) (2.37)$$

Where $\overline{V}$ the mean velocity is the ratio flow rate Q divided by the cross-section area $A_{channel}$:

$$\overline{V} = \frac{Q}{A_{channel}} \qquad (2.38)$$

yielding, in a square duct where $\beta = 1$, $\dfrac{V_{max}}{\overline{V}} = 2.09$.
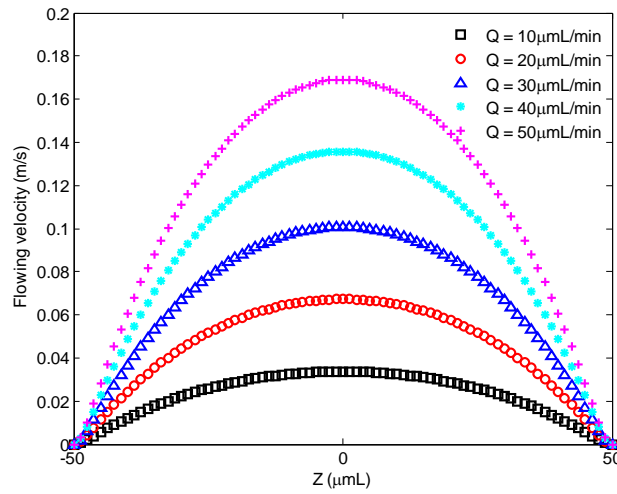
Fig. 2.13. Flowing velocity profiles along Z axis direction at different flow rates.
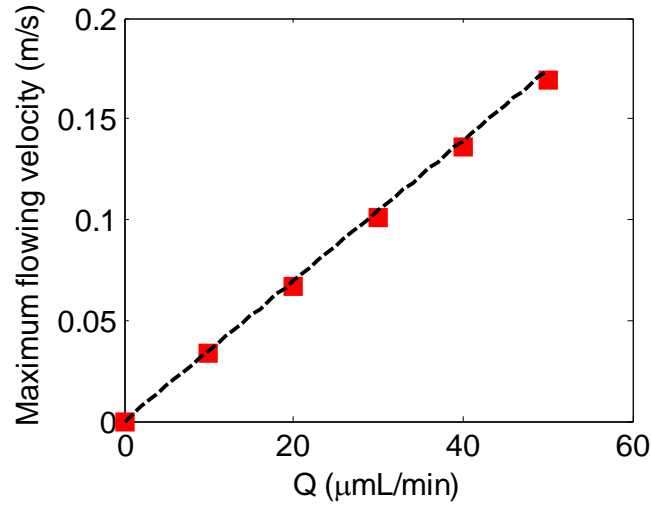
Fig.2.14. Maximal flowing velocities as a function of flow rate ranging from 0 to 50 μL/min. The red square markers denote the simulated results, and the black dashed line represents the calculation from eq(2.38).

Fig. 2.14 depicts the maximum flowing velocity through the center linearity trend of a function of the volume flow rate. As expected, the maximum velocity is found at the channel center and the maximal velocity V_{max} (mm/s) is proportional to the flow rate Q (μL/min):

$$V_{\max}(Q) = 0.0336Q \qquad (2.39)$$

2.5. Model implementation with Matlab algorithm

The function in eq(2.26) is implemented with Matlab^{TM} taking into account the $r_{ext,i}$, $\omega_{d,i}$ and $\tau_{d,i}$ calculated from previous simulation steps (Zemax, Fluent). The other parameters used are shown in Table 2.2. All the OFI signals from each particle in different positions inside the channel are calculated, and then summed up.

Tab 2.2. Rate equation OFI signal simulation parameters

Simulation parameters	Value
Photon lifetime in laser	$\tau_p = 10^{-12}$ s
Distance from laser to channel	L =76 mm
Incidence angle	$\theta = 15\,°$
VCSEL aperture diameter	DA=6μm
laser output cavity mirror reflectivity	$r_2 = 0.9995$

The final OFI time domain signal is transformed to the frequency domain via Fast Fourier Transform (FFT). The simulated spectra for 20μL/min and 40μL/min are plotted in Fig. 2.15. One of the most important results of this simulation is that there are two well-defined peaks in each spectrum. The low frequency (*fd1*) peak results from the forward scattered reflected light, and the frequency at the maximum of the peak corresponds to the Doppler shift induced by the velocity of the particles flowing at the R_{ext} peak position. The second frequency peak (*fd2*) corresponds to the velocity at the other R_{ext} maximal position that is located at the center of the channel.
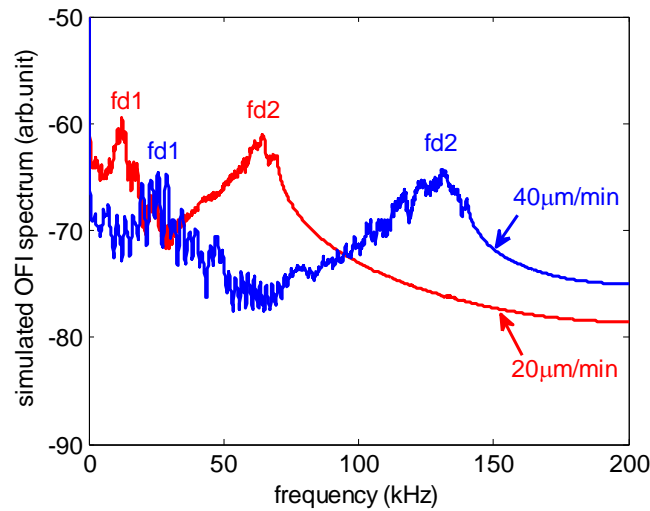

Fig.2.15. Simulated OFI power spectra obtained for different flow rates (Q = 20 μL/min in red and 40 μL/min in blue).

While increasing the flow rate at 20μL/min and 40μL/min in the simulation, both spectral peaks shift towards higher frequencies while they tend to broaden because of a larger velocity dispersion.
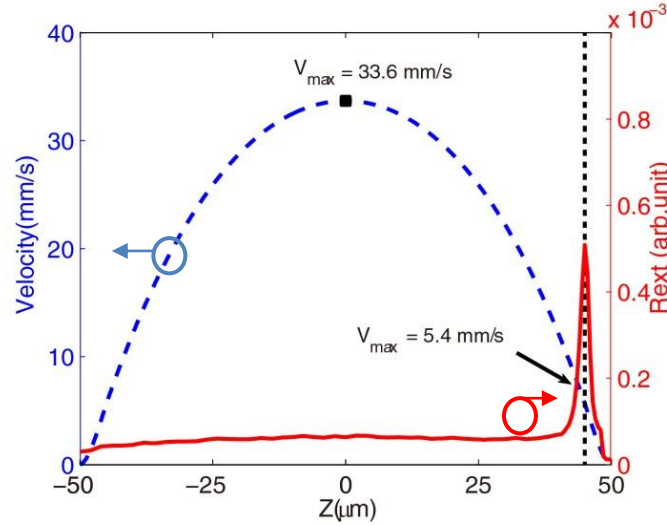

Fig.2.16. Fluent-based velocity simulation profile (blue dashed line) along the laser axis z' (flow rate Q=10μL/min) yields to a maximal value 33.6mm/s at the channel center. The power reflectivity profile coupling in laser (red solid line) along the same axis yields a sharp reflectivity peak where the OFI signal is enhanced by the reflection of forward scattered light on the rear interface. The peak center position (black point line) corresponds to a velocity of 5.4mm/s.

2.6. Improvement of the modeling

In former subsections, we succeed to propose a model for the OFI microfluidic flowmetry Doppler frequency spectrum evaluation by summing up all the feedback perturbations from a great amount of flowing particles in a microchannel. However, there are two factors we have not taken into account:

1. Due to the incident and back-scattered propagation angle distribution, the Doppler shift induced by a single particle is a distribution of frequencies centered at the Doppler frequency shift taken into account in the previous section.

2. The light power extinction due to the turbidity of the solution during the laser propagation in the channel.

In this subsection, after a detailed theoretical work in order to analyze the influence of these two phenomena on OFI flowmetry measurement, a modified numerical simulation method based on our previous work is presented and compared with the previous simulation results.

2.6.1. Single particle scattering behavior

When the laser beam impinges on a moving object, the absolute value of the Doppler frequency f_D is proportional to the scalar product of the vector difference

$\vec{k} = \overrightarrow{k_{sca}} - \overrightarrow{k_{inc}}$ and the velocity vector $\vec{V}$ as presented in eq(2.16).

In the former model, we have assumed that the scattered light propagates straightly backward with respect to the incident light without any angular distribution,

$\overrightarrow{k_{sca}} = -\overrightarrow{k_{inc}}$, yielding,

$$\left|\vec{k}\right| = 2\left|\overrightarrow{k_{inc}}\right| \tag{2.40}$$

The Doppler frequency shift f_D and the laser output power under feedback modulation P_{OFI} can be written as:

$$f_D = \frac{2\left|\vec{V}\right|}{\lambda}\left|\sin\theta_{inc}\right| \tag{2.41}$$

and

$$P_{OFI}(t) = P_0[1 + m\cos(2\pi f_D t + \Phi_D)] \tag{2.42}$$

In fact, when the laser beam impinges on a target and in particular a particle, the scattered light vector $\overrightarrow{k_{sca}}$ presents a considerable angular distribution rather than a single directional propagation. This complexity can link to the $\overrightarrow{f_D}$ variation Δf_D by imparting an absolute value distribution of the difference $\vec{k}$.

$$\Delta f_D = \frac{\left|\overrightarrow{\Delta k} \cdot \vec{V}\right|}{2\pi} \tag{2.43}$$

Thanks to Zemax's ray-tracing simulation capability, the individual particle scattering performance is investigated by means of geometrical optics (GO) in our work. As a well-documented method of scattering calculation[130], GO is widely applied to particle scattering study because of its clear interpretation of the scattering mechanism and its simplicity, especially when the wavelength is much smaller than the particle size ($\lambda \ll D_p$). In this method, the incident beam is considered consisting of a great amount

of rays, and the interaction between each ray and the particle is calculated using the rules of geometrical optics. Finally, the resulting field can be calculated by a superposition of all of rays' fields of the different scatter orders indicated by the factor p as:

$p = 0$ corresponds to external reflection plus diffraction.

$p = 1$ corresponds to direct transmission through the sphere.

$p = 2$ corresponds to 1 internal reflection, and so on…

In the particle scattering simulation that is shown in Fig.2.17[131], we consider a perfect TEM$_{00}$ Gaussian beam with an intrinsic waist radius ω_0 at $1/e^2$, propagating along z direction. Its waist is located at $O_G(0,0)$ in the Z-Y coordinate system. The particle is considered as a homogeneous sphere of which center is located in $O_P(0,d)$.
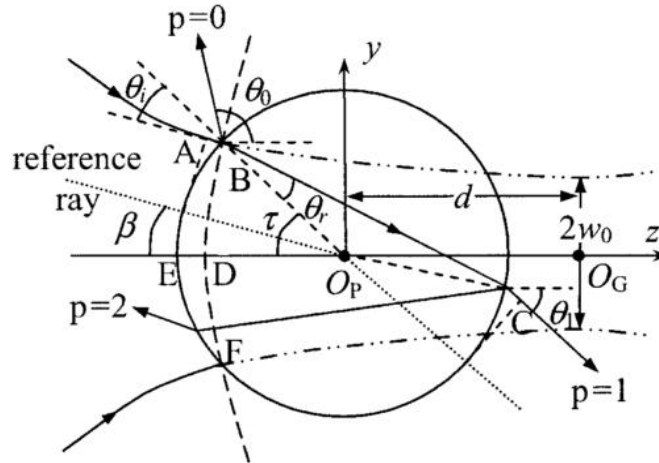
Fig.2.17.Schematic of the laser-particle interaction. The particle is located on the z axis of the incident beam. O_p is the particle central position, O_G the Gaussian beam waist central position.

In Fig. 2.18, the simulated angular distribution of scattering intensity from a single particle is plotted. One can observe that the scattered light propagates mainly in three directions. The most prominent peak is in the backward direction (180°) and can be attributed to the reflection (p=0). The two smaller peaks are located symmetrically at around +/- 14° from the backward direction and can be explained as arising from refraction after one internal reflection (p=2).
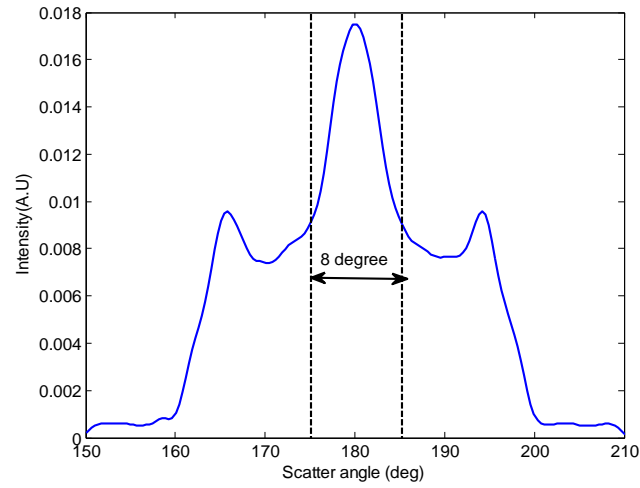
Fig. 2.18.Normalized scattered light irradiant profile simulated as a function of scattering angle in ±4degrees from the backward direction (180°) in Zemax simulation.

But not all the scattered light can be collected into the laser cavity, the specific scattered light collecting angle range is limited to the lens numerical aperture (NA). In the simulation NA=0.39(~40°) as shown in Fig.2.19, thus angle limitation is from 160 to 200°.
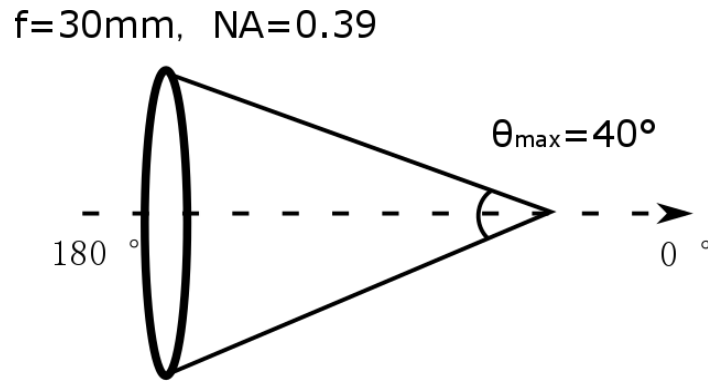
Fig. 2.19.Schematic of the focusing lens numerical aperture. 0° and 180° denote the forwards and backward scattering direction, respectively.

It should be noted as well that apart from the optical system aperture, the scattered beam is also confined by the laser diode structure which plays the role of the photon receiver. Here we assume that the "laser aperture" is identical with the emission one. Considering the paraxial approximation, the beam incident aperture Ψ can be calculated as the laser

output divergence angle θ_D scaled by the optical system magnification $\dfrac{f_1}{f_2}$ and the

refractive index of the liquid medium (here is water) n, yielding $\Psi = \dfrac{\theta_D}{n}\dfrac{f_1}{f_2} = 3.7°$.

Considering both confinements, lens aperture and laser cavity aperture, only the scattered rays in the direction range from 176° to 184° can re-enter the laser diode, and contribute to the feedback perturbation (dashed line in Fig.2.18).

Considering that the incident laser beams exhibit a Gaussian spatial and angular intensity profile, the scattering properties of the particle are dependent on its position in the incident beam. To investigate the scattering performance dependence on particle position, the previous simulations are repeated in different coordinates denoted as in Fig. 2.20 (a), and all the resulting scattering profiles are illustrated in Fig.2.20(b).

In e(0,0) where the particles exactly in the laser beam waist center, the incident beam is of the maximum power density, producing the dominating peak produced from reflection(p=0) with maximal enhancement. The side peaks arising from the 2nd scattering order shift slightly. In other positions, there is a dominating scattering peak due to reflection (p=0) constantly existing in each figure as ate(0,0). However, one of side peaks (p=2) is eliminated considering that the incident profile is not symmetric anymore. Since we just consider 8 degrees range of scattering light direction (denoted by the black dashed line in each subfigure), most of the back-scattered power re-entering the laser cavity is the dominating peak (p=0). In order to simplify the model calculation, we ignore the angular profile deviation in different positions, assuming they are all similar to the one ate(0,0).

(a)

(b)
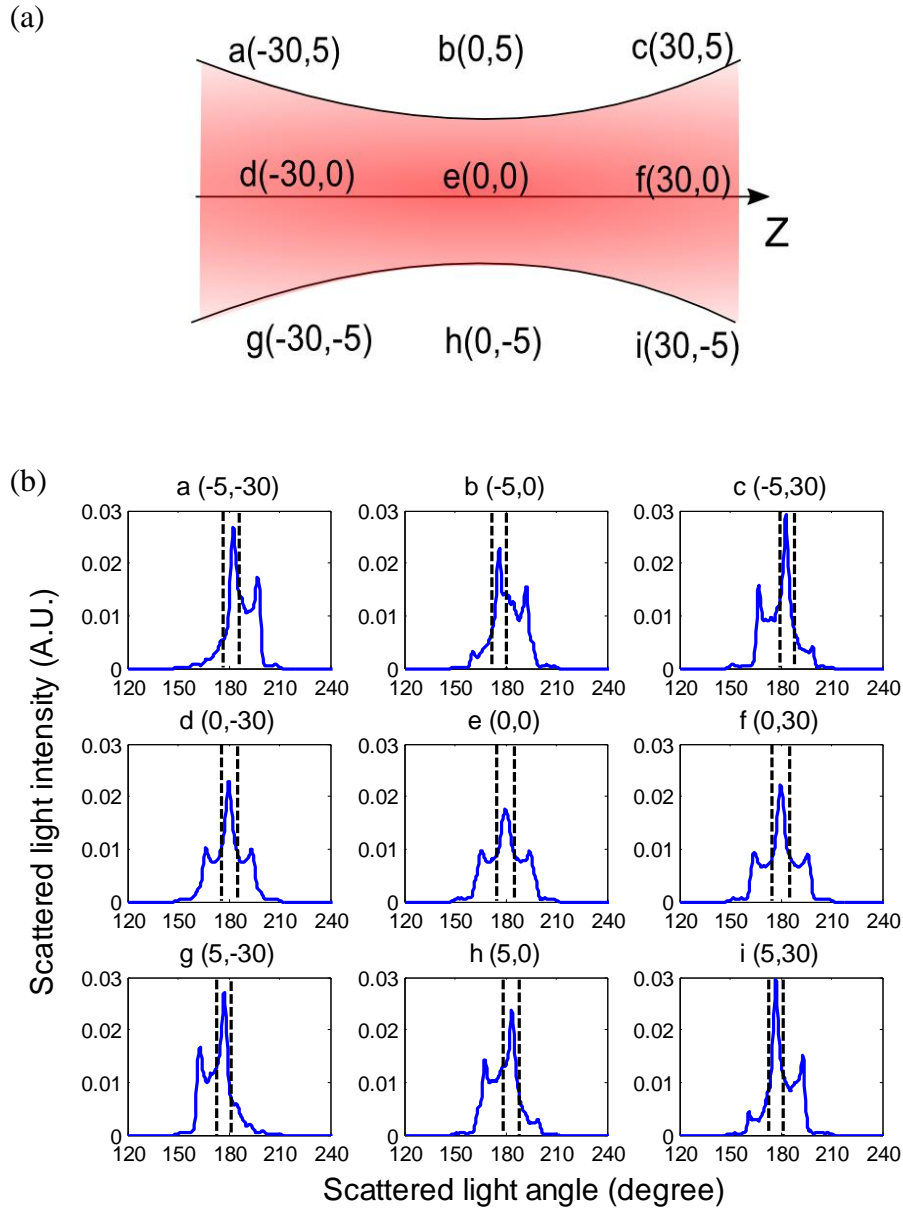
Fig. 2.20. Scattering simulations in different particle Z-Y coordinates. (a) Sample central position arrangement with the Z-Y coordinates in μm. (b) Scattering angular profiles corresponding to each position. The dashed lines denote the scattered light angle range from 176 to184 degrees where the scattered light can be collected into the laser diode.

2.6.2. Modified OFI output power including scattering angle dispersion

The scatter radiation angular dispersion can lead to a measurable spectral broadening, thus a mathematic effort has been made in order to take into account this effect.

Let's first consider a unique particle in the sensing volume.

As sketched in Fig.2.21 one incident wave with wave vector $\overrightarrow{k_{inc}}$ the corresponding scattered radiation vector $\overrightarrow{k_{sca}}$.

Fig. 2.21. The schematic of $\overrightarrow{k_{inc}}$, $\overrightarrow{k_{sca}}$ and $\vec{k}$.

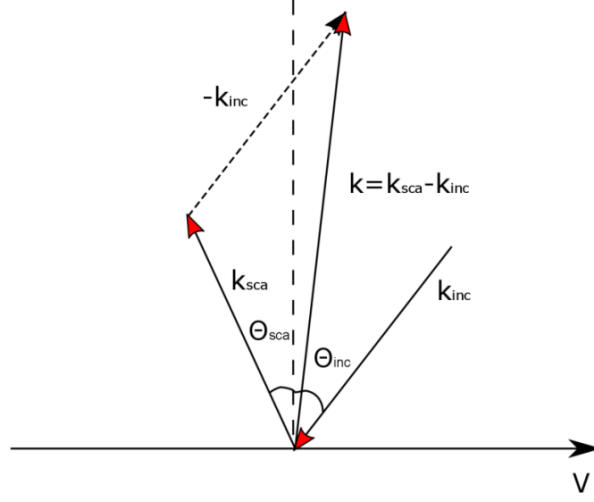Both incident and scattered angle are defined with reference to the perpendicular axis to the vector $\vec{V}$. Thus $\vec{k} \cdot \vec{V}$ is expressed under the following form:

$$f_D = \left| \frac{\vec{k} \cdot \vec{V}}{2\pi} \right| = \frac{|\vec{V}|}{\lambda} \left| \sin\theta_{sca} + \sin\theta_{inc} \right| \tag{2.44}$$

When the translating particle with velocity V_i passes into the sensing volume, the Doppler frequency shift is a combination of angle distribution projection of both the incident and scattered wave vector.

In our modeling we will limit to considering the scattered angle distribution so that the Doppler shift is the sum of all $f_{D,k}$:

$$f_{D,k} = \frac{|V_i|}{\lambda} \left| \sin\theta_{sca,k} + \sin\theta_{inc} \right| \tag{2.45}$$

The OFI signal in time domain bursts from i^{th} particle is defined by:

$$P_f(t) = P_0 \left[1 + \sum_k m_k \cos(2\pi f_{D,k} t + \Phi_{D,k}) \exp\left(-\frac{(t - t_0)^2}{2\tau^2} \right) \right] \tag{2.46}$$

57

where τ is the time of travel of the particle in the sensing volume and where the exponential term is a ponderation of the optical power back-scattered due to the Gaussian distribution of the photon density in the laser beam.

The modulation index along the kth angle vector m_k is calculated from the previous scattering simulation. We set the particle velocity to be 3 mm/s, the burst arising from a single particle is depicted in Fig.2.22(a). The power spectrum is also presented by applying Matlab FFT in Fig.2.22(b) with a frequency broadening frequency variation Δf_D due to the scatter vector distribution:

$$\Delta f_D = \frac{V \sin \Delta\theta_{sca}}{\lambda} \qquad (2.47)$$
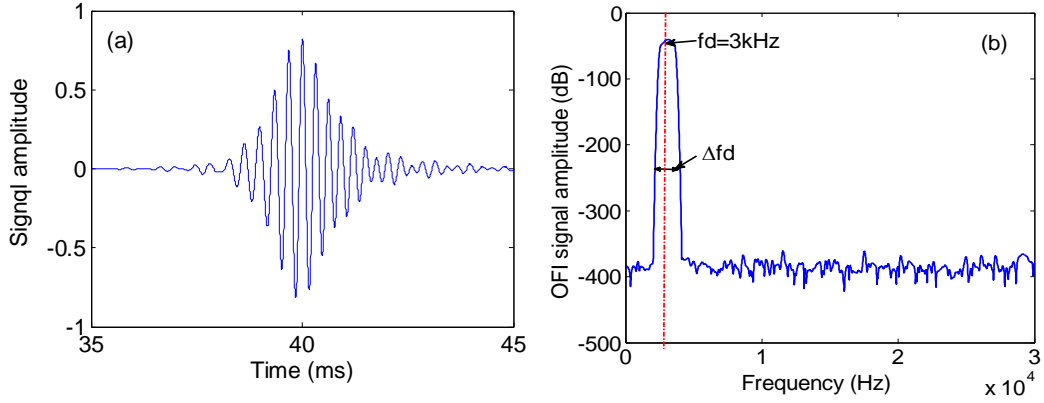
Fig.2.22.Simulated OFI for one flowing particle of velocity of 3 mm/s while taking into account the scattered light angular dispersion. (a): the burst produced by the particle passing the sensing volume in a period of τ=4ms. (b): the frequency spectrum retrieved by FFT from the burst signal, exhibiting a spectral broadening Δf_D.

Now let's consider the multiple particle case.

The temporal OFI signal is a continuous fluctuation rather than discrete burst. In practical measurement, we apply a long acquisition and average routines, so we can assume that all the discrete location inside the sensing volume are occupied by a particle, each of them contributes to the OFI signal continuously and simultaneously. The OFI output power can be derived as:

$$P_f(t) = P_0[1 + \sum_i \sum_k m_i \cos(2\pi f_{D_{i,k}} t + \Phi_{D,k})] \qquad (2.48)$$

The frequency spectra with or without considering the scattered vector deviation are depicted in Fig. 2.23.
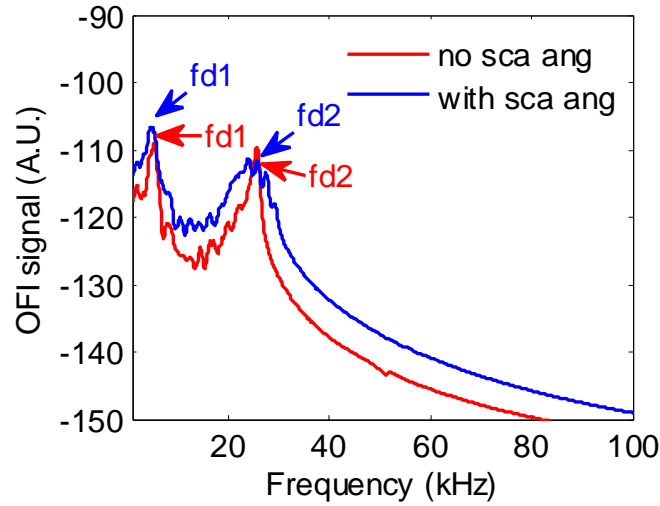
Fig. 2.23.Simulated OFI spectra in 20μL/min and40μL/min.

The frequencies of *fd2* correspond to the maximal velocities as a function flow rate is presented in Fig.2.25. The this linear trend is in good agreement with the theoretical results.

One can observe that the new simulation model presents a broader Doppler frequency width due to the scattered light angular distribution which should be more consistent with the reality. The abrupt peak in the former model (red line) results from the numerous Doppler frequency segments superposition from the particles passing close to the channel center where the velocity varies gently Fig.2.15.

The spectra in different flow rates are shown in Fig.2.24, and the *fd2* peak frequencies responding to the maximum velocity are measured.
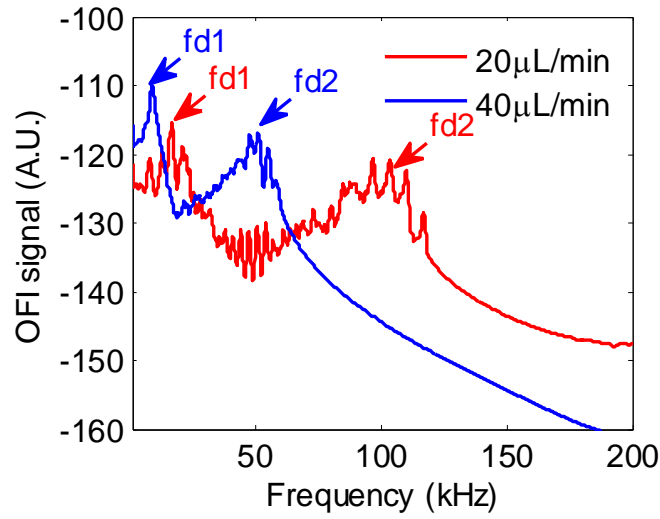
Fig. 2.24. Simulated OFI spectra in 20μL/min and40μL/min.

The frequencies of *fd2* correspond to the maximal velocities as a function flow rate is presented in Fig.2.25. This linear trend is in good agreement with the theoretical results.
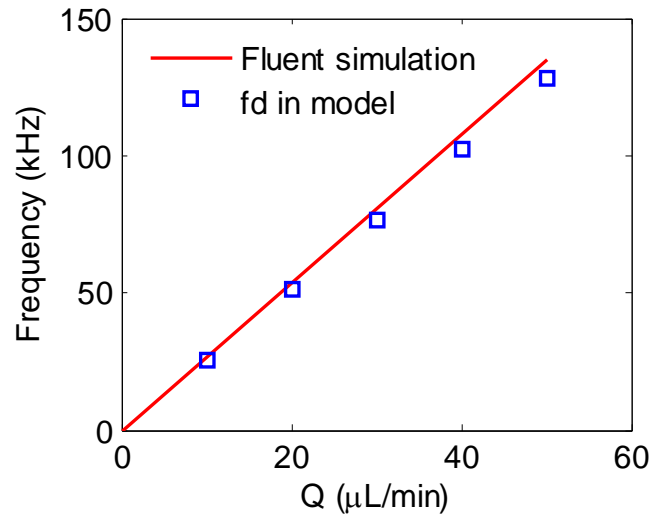
Fig. 2.25. Linearity dependence of the maximal Doppler frequencies *fd2* with flow rate. The blue square marks denote the simulation results, and the red curve is the theoretical calculation.

To conclude on this part, the model is quite efficient. As can be seen in Fig. 2.23, the simulation of the OFI signal while taking into account the scattering angle divergence is very similar to the one obtained not taking it into account. Considering that the simulation with this parameter is very long (several days) we have decided not to use this modeling in the further chapters and we will restrain ourselves to the model described in section 2.2.6.

2.6.3. Modified OFI signal model subjected to attenuation

In many OFI based biomedical detection applications such as blood diagnosis, the attenuation of the liquid agent impairs significantly the laser power through the beam propagation[132]. This phenomenon resulting in the OFI signal drastic corruption has been under study so far. As a laser beam propagates through a medium [133], its power P experiences an exponential attenuation, and the attenuation strength depends on the propagation distance z.

$$P = P_0 \exp(-\delta z) \tag{2.49}$$

where, P_0 is the initial power before propagation, and δ denotes the extinction coefficient which depends on the particle number in unit volume N_p and the particle cross-section σ_{ext} at the considered wavelength that accounts for both the absorption and the scattering losses.

$$\delta = N_p \sigma_{ext} \tag{2.50}$$

$$\sigma_{ext} = \sigma_{abs} + \sigma_{sca} \tag{2.51}$$

Where, σ_{abs} and σ_{sca} are efficient absorption cross-section and scatter cross-section, respectively.

Particle's extinction cross-section depends on the wavelength, particle dispersion relationship natures and particle size. The extinction cross-section values of polystyrene spherical particles of different particle sizes are calculated using software *mieplot* in Fig.2.26.
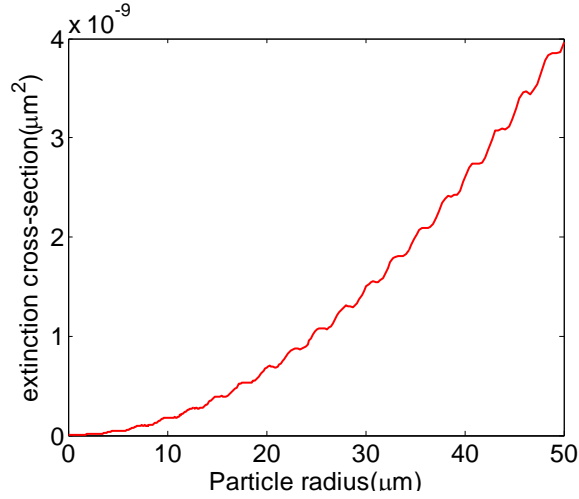
Fig.2.26. Dependence of extinction cross-section on the polystyrene particle radius via *mieplot*.

Now let's revisit the OFI signal simulation in 100μm×100μm channel which is filled with a solution of the 4.89μm polystyrene particle in water. The power attenuation ratio (P/P_0) through the 100μm channel in different particle densities is shown in Fig.2.27. One can observe that when the particle density is high enough like 10^9/mL(blue), the laser beam power is corrupted completely when the beam approaches the rear interface of the channel. Otherwise, when the particle density is lower than 10^7/mL(black), the attenuation can be negligible in such a short distance. In our experimental condition which will be presented in Chapter 3, the maximal attenuation factor is still less than 4% after the propagation in the solution, thereby this aspect will be negligible in all further measurement.

Fig.2.27. Relative power corresponding to the propagation in polystyrene solution with a particle number of 10^7/mL(black) ,10^8/mL(red) and 10^9/mL(blue).

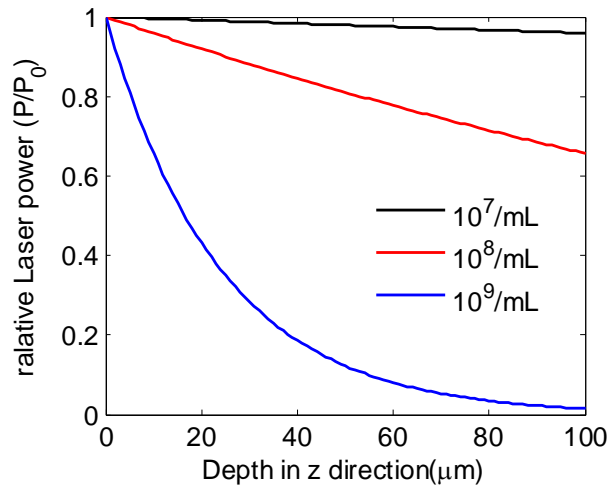The OFI cosine function from the ith particle in eq(2.48) can be corrected by accounting the extinction factor. Because of the round-trip light propagation in OFI measurements, the radiation is attenuated twice through the solution, thus a factor of 2 should be added in the right side term.

$$P_f(t) = P_0[1 + \sum_i \sum_k \exp(-2\delta z_i) m_i \cos(2\pi f_{D_{i,k}} t)] \qquad (2.52)$$

Besides influencing the attenuation factor, particle density also determines the signal level. In the case of higher particle density, in the unit time period, more particles can be captured. During a given data acquisition time period the OFI signal level increases proportionally. In Fig.2.28, the simulated OFI spectra via the latest OFI signal model eq(2.52) at different particle densities are depicted.
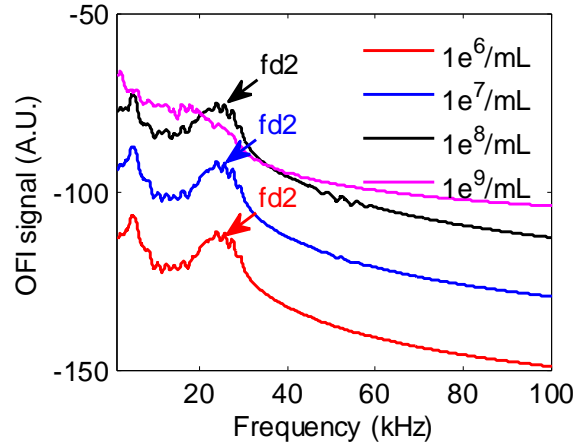
Fig. 2.28. Spectra of different PS concentrations (1e^6/mL,1e^7/mL,1e^8/mL and 1e^9/mL).

The particle density impacts on the OFI signal level via both attenuation through the beam path and the total particle acquisition number. When the density is 10^5/mL, even with the lowest attenuation which can be neglected, the OFI signal is still too poor due to the infrequent particle capture. On the other hand, in the case of 10^9/mL, the OFI signal gets the maximum level since plenty of particles contribute to the OFI signal. When the particle density increases continuously, the laser beam cannot enter further, only the particles passing through the top area of the channel can contribute to the feedback light.

2.7. Conclusions

In this chapter, a novel numerical modeling approach of OFI sensing scheme in micro-scale fluidic systems has been developed by merging simulations results of the fluid flow velocity, the optical propagation and the laser rate equations.

For this purpose, a new laser output power expression involving all the feedback perturbations from each scatterer is developed from the typical three-mirror cavity model. Thanks to numerical simulation methods, both optical propagation and fluid flow velocity distribution are investigated exhaustively, thus the velocity and feedback power ratio of each particle are calculated. Finally, OFI flowmetry sensor output power signal is simulated via a home-made MATLAB algorithm based on the mathematic expression and simulation results.

Moreover, based on the theoretical principle of both laser-particle interaction and laser extinction through the medium, the dependences of OFI signal upon the scattering vector angular distribution and particle density are demonstrated to improve our model further.

This new modelling method is a crucial first step to the design of really compact integrated OFI sensors enabling precise flow rate or fluid velocity monitoring.

3 Experimental validation: VCSEL-based OFI sensor applied to fluid flow monitoring in micro-channels

3.1. Introduction

In Chapter 2, thanks to multiple numerical simulation software, we proposed a new method to simulate the signal of an OFI based velocimetry sensor. Such method enables the assessment of the OFI velocimetry sensor performance. In the current chapter, we exhaustively investigate the OFI flowing velocity measurements implementation by comparing the simulation results to the measurement ones in order to validate our method. We also discuss the importance of the parameters of the experimental conditions on the OFI signal spectrum.

This chapter is constructed as the following: first, the laser source OFI signal-current characterization experiment is demonstrated for OFI sensor designing, second, flowing velocity measurement is performed, and the experimental results are compared with the simulation results. Moreover, several important factors that influence the OFI signal spectrum are investigated: the particle size, the particle concentration, the waist position and the channel dimension.

3.2. Characterization of the laser diode used for the experimental validation

As can be seen in the model developed in Chapter 2, the OFI sensor performance strongly depends on the optical performance of the laser source (mode behavior, linewidth, emitted power, …), so that the laser source is a critical factor in OFI sensors. Compactness and multipoint measurement capability that VCSELs offer are also important parameters for sensing applications. Consequently, in this work, we used a

commercial VCSEL emitting at 670nm for the approporiate output performance and ease of alignment with the micro channel due to the visible wavelength.

First, we employed a commercial 670nm VCSEL for the model validation. This VCSEL is referred as PS67-F1P1U-4U-AC (Optowell Co., Ltd) and is mounted in a TO-46 package where a monitoring photodiode is embedded, from which we can measure the considerable OFI signal. To our knowledge, the polarization behavior of this VCSEL is not specially controlled; however, no polarization flip was observed in the operation range we used. Despite polarization flips can enhance in some cases the OFI signal level [134], this effect was not exploited in this work as we did not include polarization effects in our model.

Before applying microfluidic measurements, we investigated the injection current dependence of the OFI signal amplitude[135].

3.2.1. Setup description
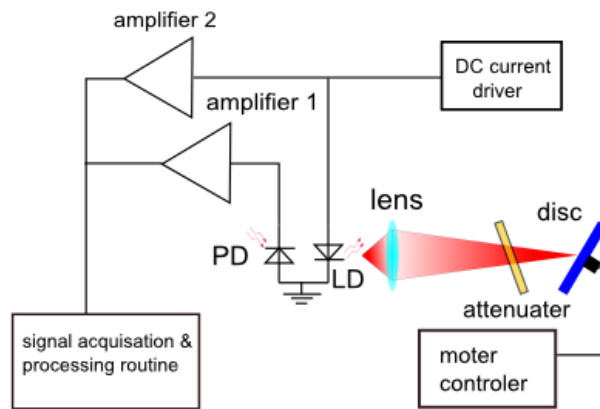
Fig.3.1. Schematic of OFI signal for the injection current sensitivity characterization setup.

The setup employed for the OFI signal versus injection current characterization is sketched in Fig. 3.1. The laser beam is focused on a metallic rotating disk which is driven by a step motor associated with a custom-made proportional-integral-derivative controller ensures a constant velocity. The laser driver is based on MOSFET as the current source. The monitoring photodiode amplified current is the OFI signal. The photodiode current amplification is ensured by a multistage amplifier based on low-

noise operational amplifiers. The first stage is standard transimpedance amplifier where the operational amplifier is fedback by a 1 kΩ resistor. This stage amplifies the DC photocurrent and the output is connected to an output SMA connector in order to perform the light current measurement. Two other voltage amplifier with band-pass filtering allow full recovery of the OFI signal. The gains of each stage are 60 dBV/A, 26 dB and 26 dB achieving a total gain of 112 dBV/A.

As a first step in the laser characterization, the light-current relationship is measured by monitoring the photodiode current of the VCSEL. It allows a good identification of the threshold current which value is approximately 1.6mA (see Fig.3.2).
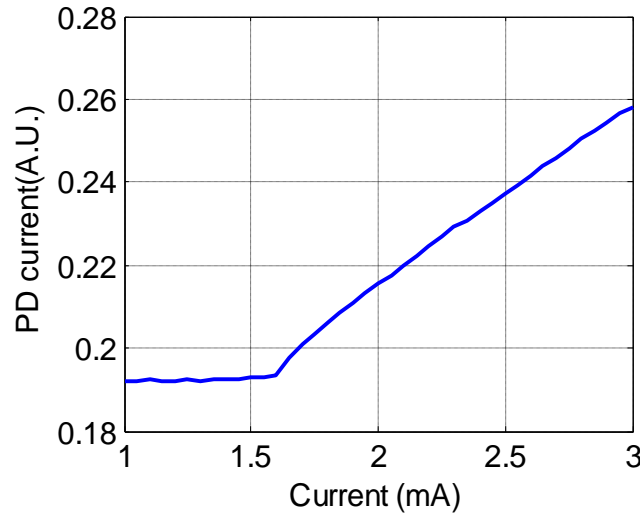
Fig.3.2.The light-current characteristic of the PS67-F1P1U-4U-AC 670 nm VCSEL.

3.2.2. SNR-current characterization

The OFI signal frequency spectrum at 3mA current is illustrated in Fig.3.3, a clear frequency peak indicates the velocity on the rotating disc surface.

The evaluation of the Doppler frequency peak being fully automatized, a Gaussian fitting is applied to the spectrum in the vicinity of the peak. The Gaussian fitted function is:

$$Amp(f) = Af + B\exp\left[-\frac{(f - f_{max})^2}{2FWHM^2}\right] + C$$

(3.1)

67

The variable is the frequency f, *Amp* is the signal amplitude, f_{max} is the maximal frequency depending on the motor velocity, FWHM is the full-width at half maximum of the OFI signal. *A* and *C* are the fitting parameters denoting the floor noise of the spectrum and *B* weights the Gaussian profile amplitude and thus represents the visibility of the signal.
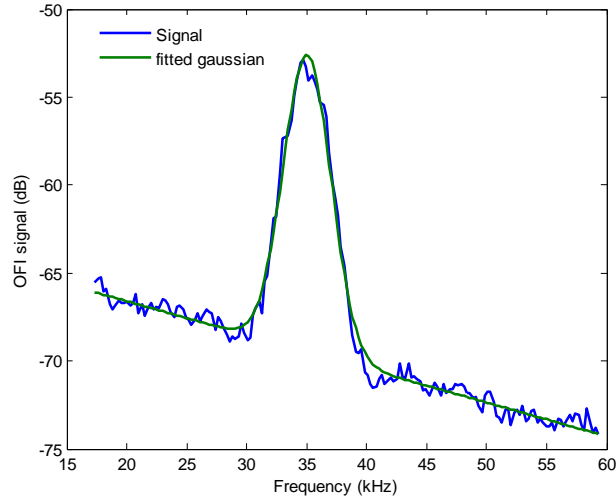
Fig.3.3. Gaussian fitting applied in 670nm VCSEL laser diode characterization (applied current: 3mA).

Then, we repeat the data processing to evaluate the visibility over the achievable current range to find the optimal current value at which the OFI velocimetry sensor can lead to the maximal SNR. The visibility dependence to the current curve is plotted in Fig.3.4, and we can conclude that above the threshold current value 1.6mA, the SNR increases almost linearly with the current. Moreover, we observed this trend for current up to 4mA. The current in all the following velocimetry measurements was thus set to be 3.5mA, for which the laser was still emitting in the singlemode regime.
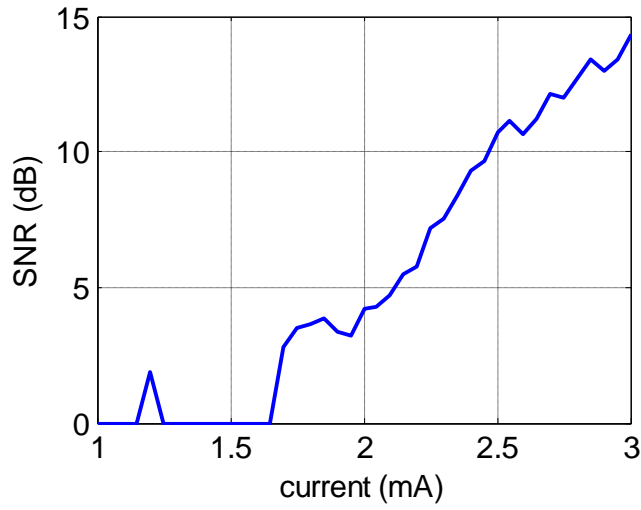
Fig.3.4. Visibility dependence on injection current of the OFI signal from 670 nm VCSEL.

3.3. Flow measurement description

3.3.1. Setup description

The schematic of the experimental setup is illustrated in Fig.3.5.
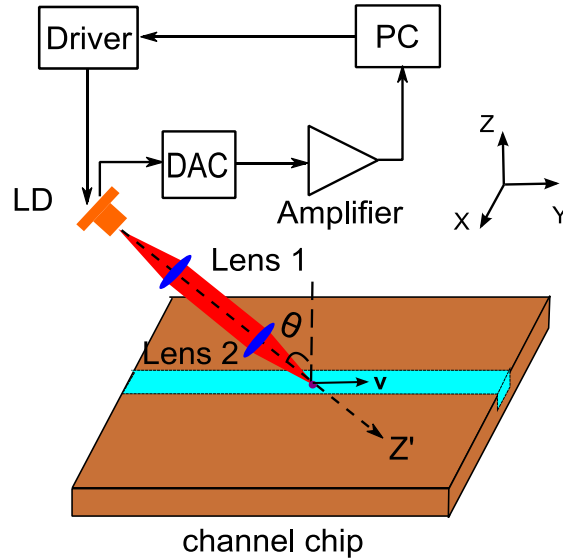
Fig.3.5. Schematic of the microfluidic measurement system.

The OFI sensor is based on the PS67-F1P1U-4U-AC 670nm VCSEL which has been presented in the previous characterization. The laser operates at a constant bias current of 3.5 mA fed through a custom designed laser driver. The incident angle θ between the

laser emission axis Z' and the perpendicular to the plane of the channel chip is set to 15°, as it is a good trade-off that allows maintaining a good signal-to-noise ratio and a sufficient Doppler shift frequency that fits our acquisition electronics.

We use a bulky doublet lens pair (MAP103030B, Thorlabs Co., Ltd) constituted by two lenses of the same focal length of 30 mm so that the imaging magnification ratio is 1:1. Considering the VCSEL beam parameters, the focused $1/e^2$ laser beam waist in the microchannel is calculated to be about 4.6 μm which should be the same as the laser output waist dimension. The VCSEL and the lens pair are assembled on a 3D translation stage (T-LSR300A-KT03, Zaber Co., Ltd) which allows adjusting the focus location.

The OFI signal is acquired through the monitor photodiode embedded in the VCSEL package. The photodiode current is amplified using the same custom-made trans-impedance amplifier that was used for the laser characterization. The output voltage is acquired using a National Instrument acquisition card (Ni USB 6251) at a sampling frequency of 400 kHz. Processing of the signal consists in averaging of 30 consecutive Fast Fourier Transform (FFT) of 2^{15} samples. All the data acquisition procedure and processing is automated by means of a dedicated LabVIEW VI.

3.3.2. Channel and seeding particle description

Three different sizes fluidic channels are used in this part as the micro-reactors:

1. A SU-8 photoresist-based channel with a 100μm × 100μm square cross-section.
2. A PDMS channel with a 1mm × 1mm square cross-section.
3. A dry film photoresist (DF)-based channel with a 96μm×96μm square cross-section.

All channels have been fabricated in the LAAS-CNRS clean room facility. The third channel was designed and manufactured specifically for the present thesis, using dry resist DF films that have similar optical and mechanical characteristics than SU-8 but are easier to implement. Its fabrication details will be presented in Chapter 4.

Polystyrene (PS) microspheres (MicroParticles, GmbH) of different diameters (196nm, 552nm, and 4.89μm) are used as the scattering particles. Such microspheres can be suspended very uniformly in aqueous solution after proper mixing due to their 1.05

g/cm^3 mass density which is similar to water. The PS solutions are pumped into the channel by a syringe pressing pump (PHD 22/2000 Harvard Apparatus).

3.4. Measurement results and discussion

In this subsection, all the OFI signals extracted in the flow velocity measurement are compared with the simulated ones. In each measurement, simulated laser incident irradiance profile and feedback power ratio profile inside channel is presented to estimate the sensing volume. To produce the most realistic model results, all the simulation parameters, variables, and features are based on experimental physical realistic values. Then both simulated and measured spectra are plotted to facilitate the comparison.

3.4.1. Effect of channel size

The channel size strongly affects the OFI signal spectra: when the dimensions of the sensing volume are comparable or even larger than the channel dimension, the distribution of velocities that are included induces that the Doppler frequency peak becomes broader and the spectrum exhibits a continuous distribution [27], [96].

The simulation and measurement results in 1mm×1mm PDMS channel and 100μm×100μm SU-8 channel are demonstrated, respectively. The simulation and measurement parameters are shown in Tab.3.1.

Tab.3.1. Simulation and experiment parameter settings

Parameter	Numerical value
Laser	670nm VCSEL
Lens	MAP103030-B (f1=f2=30mm)
PS diameter	4.89μm
Concentration	0.1w/t%
Channel	1mm×1mm PDMS & 100×100μm SU-8 channel
Incident angle	15 °
Laser current	3.5mA

The incident profile and feedback power ratio (R_{ext}) through the 1mm×1mm PDMS channel are illustrated in Fig.3.6. In Fig.3.6 (a), one can observe that the laser emission spot is located in a small area close to the center of the channel. Consequently, only the particles passing through a spatially limited area as in Fig. 3.6(b) can contribute significantly to the feedback signal into the sensor.
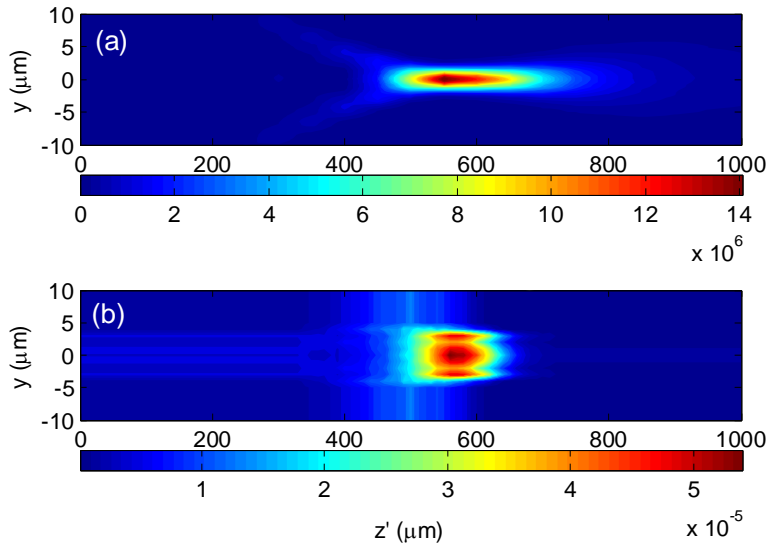
Fig.3.6. 2D simulation profile Inside 1mm×1mm PDMS channel. (a) Illumination power density profile (b) Feedback power ratio profile.

Such small sensing volume compared to the channel dimension results in a Doppler frequency peak in the power spectrum. In Fig.3.7 and Fig.3.8, the simulated and measured OFI signal spectra at Q=100μL/min are plotted. Both of spectra exhibit similar shapes, and in each figure, there is a broad but well-defined frequency peak (with maximum intensity around 2.7 kHz) denoting the maximal velocity since the beam waist has been set at the channel center. The Doppler shift value is consistent with the theoretical value calculated with Fluent.
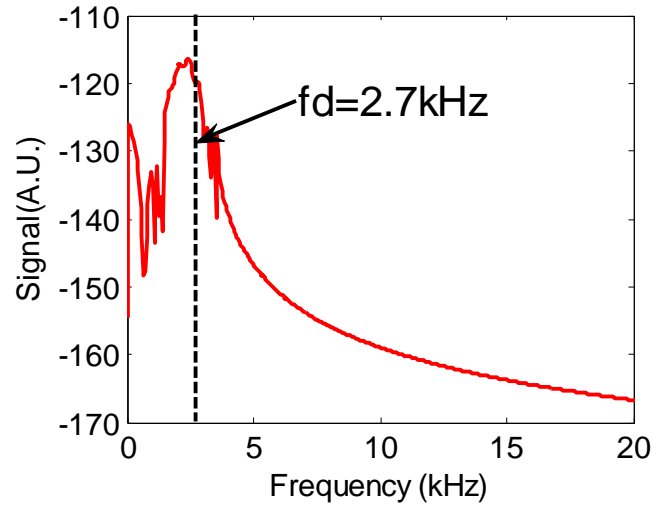
Fig.3.7. Simulated OFI spectrum with the laser focused at the 1mm×1mm PDMS channel center with a flow rate Q=100μL/min.
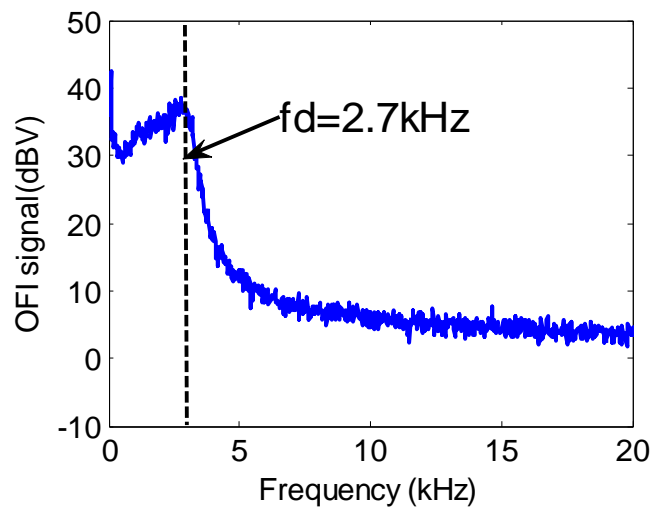
Fig.3.8. Measured OFI spectrum with the laser focused at the 1mm×1mm PDMS channel center with a flow rate Q=100μL/min.

Over the flow rate range from 0 to 400 μL/min, each spectrum exhibits a frequency peak. One can easily extract the maximal velocities at each flow rate by considering the frequency of the maximum peak amplitude. The frequency trend versus flow rate in both simulations and measurements are plotted in Fig.3.9, performing a good agreement with the theoretical value. The simulated values are slightly smaller than the experimental ones, this phenomenon could be attributed to Fluent simulation and experimental uncertainties.
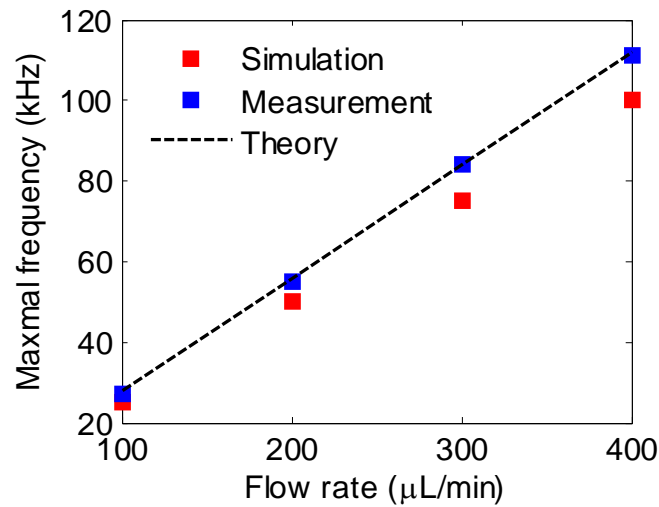
Fig.3.9. Maximal frequency trend versus flow rate inside 1mm×1mm PDMS channel. Simulations are the red square marks, measurements are the blue square makers. Black dashed line expresses the theoretical value.

Same work is applied inside the smaller SU-8 channel, the incident profile and feedback power ratio profiles are also illustrated in Fig.3.10.

The confocal parameter (twice the Rayleigh range) of the laser being around 80 μm and thus comparable with the SU-8 channel dimension, the laser beam inside the channel can be approximated as a collimated beam. Thus, with a very low change of photon density from one wall to the other, the irradiance profile does not vary significantly along the Z' axis.

As can be observed in Fig.3.10(b), the feedback power reflectivity distribution in the SU-8 channel shows a maximum at a very short distance from the rear interface. The

explanation was given in Chapter 2 already, this is the result of the forward scattered power that is in a second time back-scattered by the rear interface.
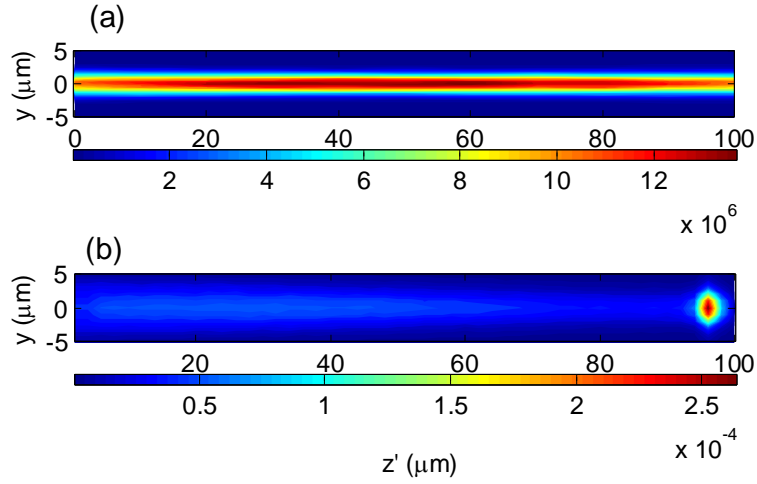

Fig.3.10. 2D simulation profiles inside the $100\,\mu m \times 100\,\mu m$ SU-8 channel. (a) Illumination power density profile. (b) Feedback power ratio profile.

In Fig.3.11-3.12, both the simulated and measured OFI spectra at Q=10µL/min are depicted, respectively. The two spectra quite resemble. In particular, both spectra have two visible frequency peaks: the lower frequency peak *fd1* that corresponds to the reflection of the forward scattered light on the rear interface and the higher frequency *fd2* that gives the velocity at the focus point, which is set in the channel center. Because of the small area of the enhancement region compared to the channel width in Fig.3.10(b), *fd1* related peak is much sharper than *fd2*.
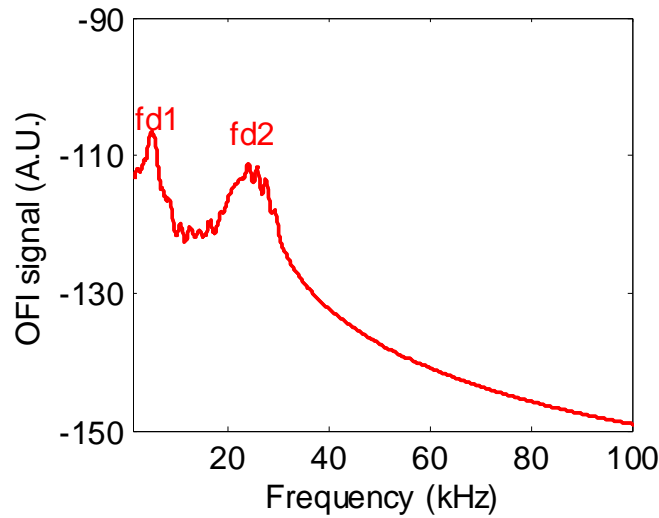
Fig.3.11. Simulated OFI spectrum inside the $100\,\mu m \times 100\,\mu m$ SU-8 channel at Q=10µL/min.
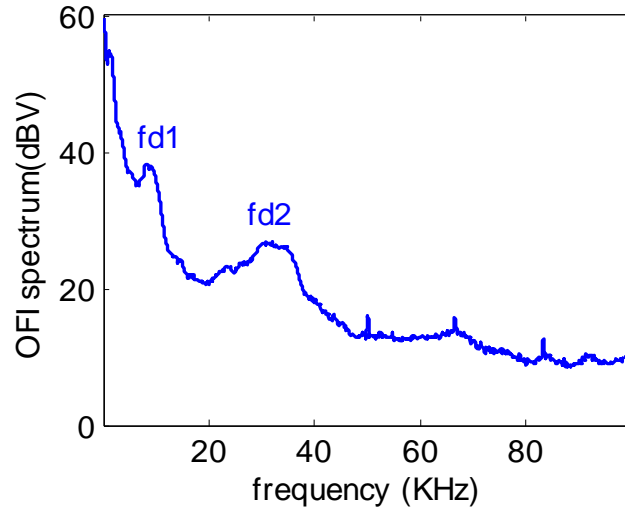
Fig.3.12. Measured OFI spectrum inside the 100μm×100μm SU-8 channel at Q=10μL/min.

As can be seen in Fig. 3.13, the OFI spectra measured at different flow rates (Q = 0 μL/min, 5 μL/min, 20 μL/min, 50 μL/min) are illustrated, respectively. Both *fd1* and *fd2* can be extracted from each spectrum.
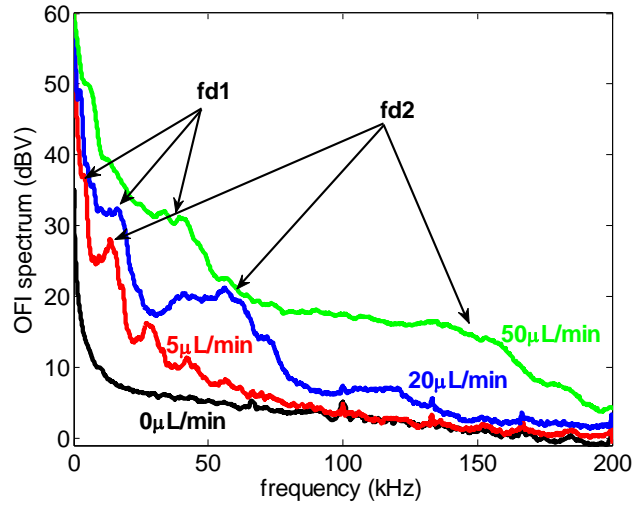
Fig.3.13. Measured OFI spectral of various flow rates: Q=0 μL/min (in black), Q=5 μL/min (in red), Q=20 μL/min (in blue) and Q= 50μL/min (in green). Both *fd1* and *fd2* in each flow rate case are denoted as well.

The Doppler frequency peak *fd1* trend as a function of Q is shown in Fig.3.14: the values in simulation (black squares) and measurement (blue circles) are in good agreement over the whole given flow rate range, and both of them are consistent with

the calculation frequency profile corresponding to the enhancement peak position in Fig. 3.10(b). This fact validates that *fd1* is linked to the particle velocity within this region where the OFI signal is enhanced by the forward scattered light reflection on the rear interface.

The Doppler frequency peak *fd2* evolution versus Q profile is plotted in Fig.3.15. Both *fd1* and *fd2* exhibit a linear dependence with the flow rate Q, as a result, the ratio between the two frequencies remains constant (about 5 in our experimental conditions). While the simulation results are very close to the directly calculated value, the experiment results are here slightly smaller than the simulation results. The position of the laser beam in the channel being controlled with an accuracy not better than 10μm, a shift of the laser beam from the channel center is the most credible reason for this small discrepancy. Thus taking this hypothesis into account, and according to the Fluent simulation, the shift of the laser beam position can be estimated to 12 μm.
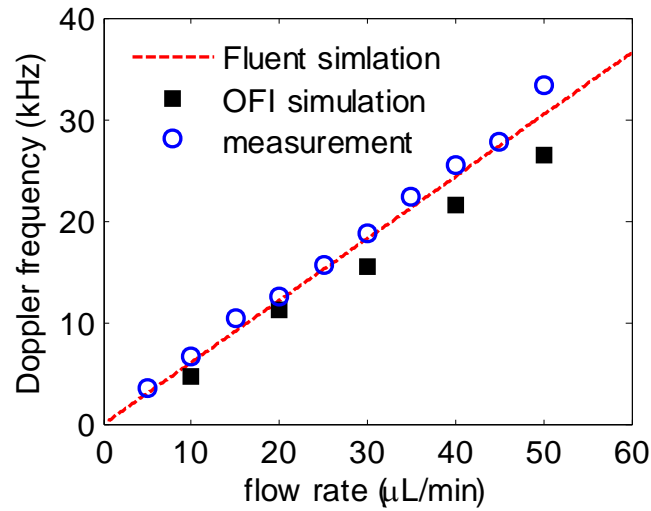
Fig.3.14. Doppler frequency *fd1* trends as a function of the flow rate. The black solid markers correspond to the simulated values, and the blue hollow circles illustrate the measurement results. The red dashed line is the calculation result associated with the Fluent simulation velocity value.
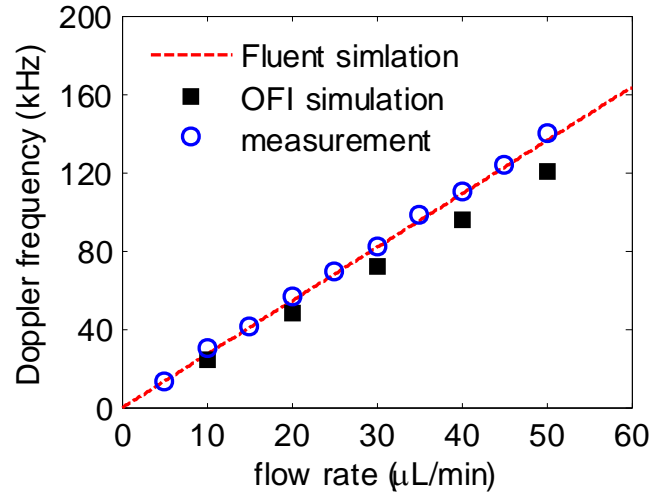
Fig.3.15. Doppler frequency *fd2* profile versus different flow rates. The black solid markers and the blue hollow ones correspond to the simulated values and the measured value, respectively. The red dashed line is the calculation frequency curve associated with the maximal velocity values in channel center based on the result in Chapter 2.

3.4.2. Effect of particle size

In microfluidic applications, the particle size identification is a major issue and many optical techniques have been developed for this aim. Among them, phase Doppler interferometric technique extending from typical dual-beam laser Doppler velocimetry has been widely used for the simultaneous measurement of droplet size in the microfluidic study[136]–[138]. However, phase Doppler interferometry needs a complicated system, while OFI could be a potential alternative method. So far, few OFI-based particle sizing technique has been documented. In the existing publications, the researchers used complex data processing methods to obtain particle size information with particle size ranging from 20nm to 200nm [139], [140]. Here, the OFI spectra from different size particles (in Tab.3.2) are simulated and measured in order to explore the potential of the OFI technique in microparticle size classification.

Tab. 3.2. Simulation and experiment parameters settings.

Parameter	Numerical value
Laser	670nm VCSEL
Lens	MAP103030-B (f=30mm)
PS diameter	0.196/0.552/4.89 μm
Concentration	0.1w/t%
Channel dimension	96μm×96μm DF channel
Incident angle	15 °
Concentration	0. 1% w/v

The irradiance profile is plotted in Fig.3.16(a) and the feedback power ratio profile with different size of PS particles are illustrated in Fig3.16(b)-(d). Because the scattered light power is proportional to the particle scattering cross-section which directly depends on the particle diameter, the feedback power ratio value with the 4.89μm diameter PS particle is constantly much higher than the two nanoparticles. In the cases of nano-scale PS particle, 1 million incident rays pointed on the particle, only a few of them can hit the nano-particle and even less actually scatters back towards the laser cavity. Thereby the feedback power ratio is as low as 10^{-9} order approaching ZEMAX simulation ray tracing approach limitation. As a result, in Fig.3.16 (b) and (c), the feedback power ratio profile is not as smooth as the one in 4.89 μm (d), due to the strong fluctuation induced by 1 or 2 rays in the Monte Carlo method. Fig.3.16 (d) is a reproduction of Fig. 3.10(b).
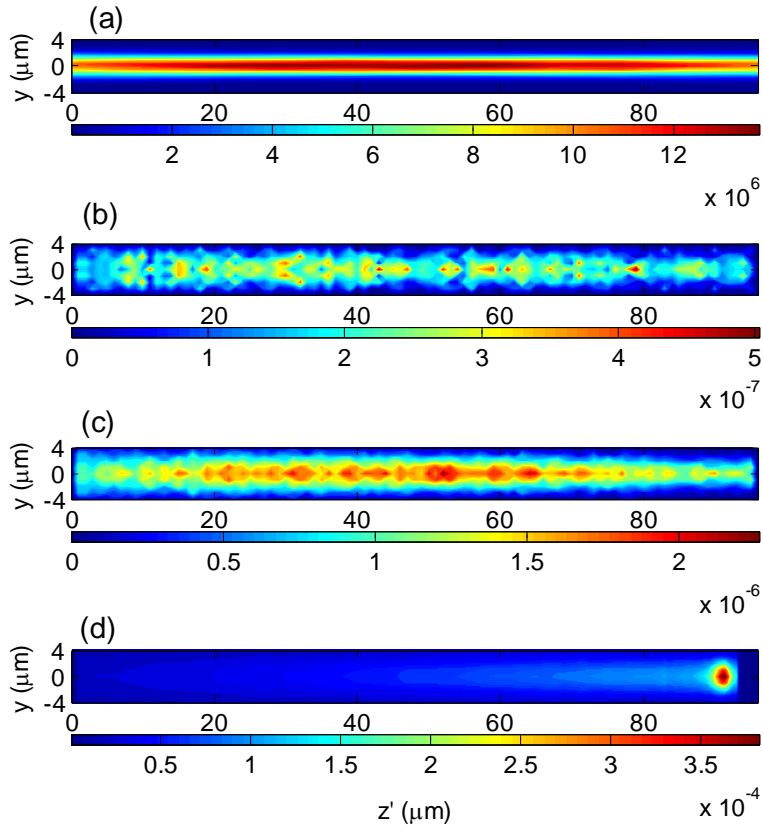
Fig.3.16. 2D simulation profiles in 96×96μm DF channel. (a) The illumination irradiance profile. (b) Feedback power ratio profile of 196nm PS particle. (c) Feedback power ratio profile of 552nm PS particle. (d) Feedback power ratio profile of 4.89μm PS particle.

The spectra of three different diameters PS particles are simulated based on the parameters settings given in Tab.3.2. As shown in Fig.3.17, all the three measured spectra are illustrated. A low frequency peak $fd1$ corresponding to the reflection of the forward scattered light on the rear interface appears again in 4.89μm particle case (black line). The spectral SNR of 552nm PS is ~20dB higher than the one of 4.89μm diameter. This signal level difference can be explained by the influence of the particle density. In the same weight concentrations (0.1% w/v), the particle density (number in unit volume) is the inverse proportional to the individual particle volume. In 4.89μm PS particle solution, the particle number density is ~5×10^6/mL, while the value for the 552nm PS particle solution is around 1000 times more, and for 196nm even around 4000 times. In spite of its larger scattering cross-section due to the particle area, in the case of 4.89μm, the lower particle number leads to fewer particles contributing to the OFI signal during the limited data acquisition period and thus in a much lower power scattered back.
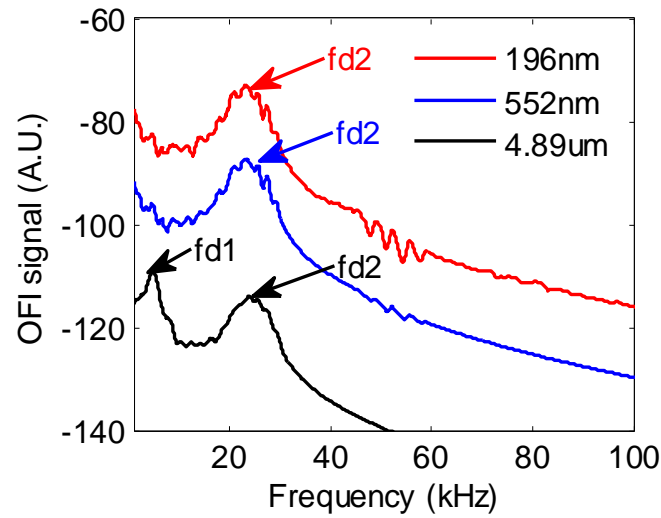
Fig.3.17. Simulated spectra of different diameters PS particles in Q=10µL/min. Red: 196nm;blue:552nm; black:4.89µm.

Measured OFI signal spectra of the same realistic configurations are also illustrated in Fig.3.18. The simulated signals for the three different particle dimensions (Fig.3.17) are not in good correlation with the measurement ones (Fig.3.18). As can be observed, only the 4.89µm have the low-frequency peak which is in good agreement with the measurements, but the amplitude difference between each spectrum is much higher in simulation than in the experiment. At that stage, we believe that either the model is incomplete, either something went wrong while implementing the model. Thus, work is in progress to understand where this difference comes from. The possible reason is in ZEMAX simulation for small particle size, due to the such low feedback power ratio values approach ZEMAX software minimal calculation capability limitation, we cannot grantee the simulated spectral amplitude accuracy quantitatively. Also in measurement, the particle concentration controlling is tricky, the measurement result cannot be ensured to be much reliable either.
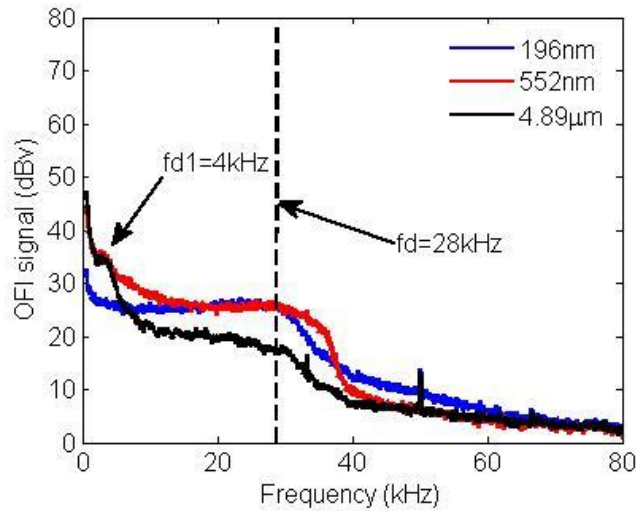
Fig.3.18. Measured spectra of different diameters PS particles in Q=10μL/min. The dashed line denotes the theoretical maximal frequency ~28kHz.

3.4.3. Effect of channel wall coating

We observed a very high feedback contribution in the back-scattered power ratio profiles in both SU-8 channel (Fig.3.10 (b)) and DF channel (Fig.3.16 (d)) and for particles with diameters higher than 552 nm. This phenomenon is most likely the result of the feedback light enhancement resulting from the forward scattering light reflection on the rear channel interface. To prove this hypothesis, we fabricated a dedicated 96μm×96μm DF channel with the same characteristics than the basic DF channel but with a gold coating on the rear interface(50nm Cr/100nm Au). This coating is expected to enhance the reflection of the forward scattering effect. Both simulation and measurement are operated with the same method in order to investigate the extra peak origin. The feedback power ratio profiles in the channels without and with Au coating are illustrated in Fig.3.19.
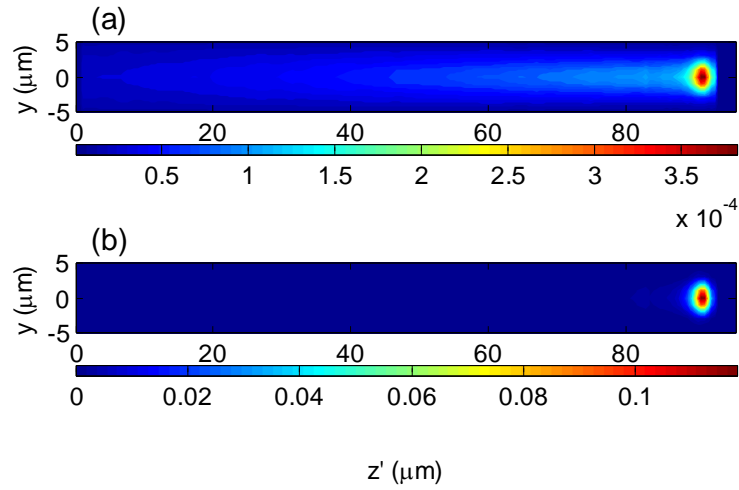
Fig.3.19. 2D Feedback power ratio of4.89μm PS particle calculated in 96μm×96μm DF channel.(a) Without coating (b) With Au coating on the rear interface.

In Au coating channel as in Fig.3.19(b), a feedback enhancement point appears in the same position, but the power ratio of the peak point is 300 times higher than in the channel without coating, due to the much higher reflectivity on the gold surface, as expected.

The higher feedback power enhancement induces a higher signal level of the extra peak *fd1* in the OFI spectra. As shown in Fig.3.20, the *fd1* peak is very high in Au coating simulated spectrum (blue line), compared with the ones in the channel without coating (in red). Besides the extra peak *fd1*, the fundamental peak *fd2* exists in each spectrum indicating the maximal velocity at the channel center.
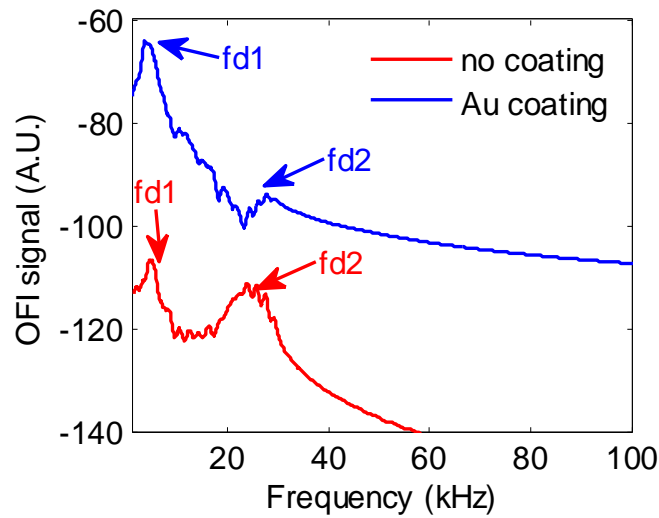
Fig.3.20. Simulated spectra of 4.89μm PS particles inside DF channels in Q=10μL/min. Blue: Au coating; red: non-coating.
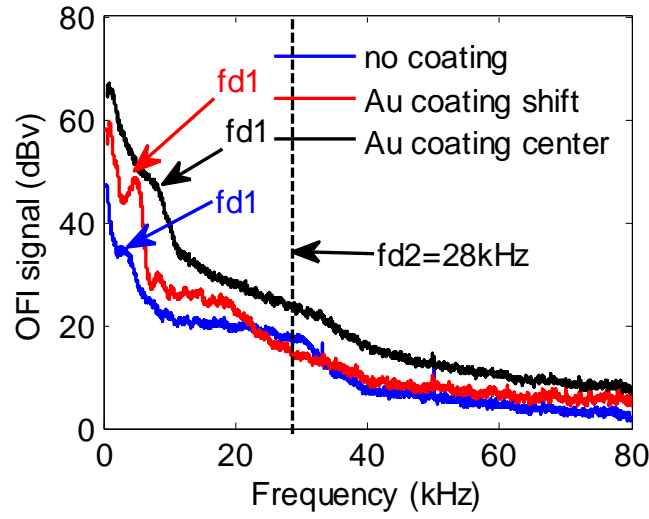
Fig.3.21. Measured spectra of 4.89μm PS particles inside DF channels in Q=10μL/min. Blue: non-coating channel center; black: Au coating at channel center; red: Au coating with a lateral position shift; The dashed line denotes the theoretical maximal frequency 28 kHz.

Unfortunately, because of manufacturing process issues, the gold coating was partly damaged on the channel rear interface during channel wall and roof fabrication and it has been impossible so far to find a large enough exploitable gold area located exactly in the center of the channel. So we had to perform a measurement with the laser beam shifted by 20μm from the channel central axis (red in Fig.3.21). Fig.3.21 presents the OFI signals with gold coating and no coating in the channel center (black and blue curves respectively) and with the gold coating at the shifted position (red curve). As can be seen, especially on the nicer gold surface the low-frequency peak is very visible with the reflective coating while it is hidden by the noise in the uncoated channel.

3.5. Depth direction scan

OFI based 1D velocity profile measurements in a 320μm circular PDMS channel were reported[141] as well as a 300×100μm rectangular channel with multiphase flow profiles. These profiles were all performed by moving the sensor perpendicularly to the laser propagation direction from one wall to the other. To achieve 2D profiles, it is required to interrogate the velocity in the two dimensions of the channel section thus scanning the flow in depth. Depth direction scan is still challenging in microchannels since the sensing volume dimension in along the laser propagation axis is considerably

large leading in a poor spatial resolution. We try to evaluate the OFI sensor capability for in-depth velocity profile measurement inside the SU-8 100μm×100μm microchannel. The scanning was performed using the automated translation stage. The laser head moves over1200μm in the Z direction from bottom to the top with a 2 μm displacement step. The measurement principle is depicted in Fig.3.22.
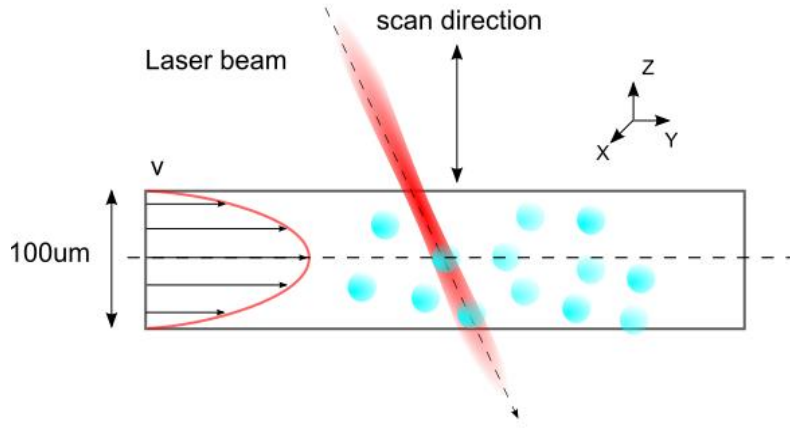
Fig.3.22. Scheme of depth direction scanning measurement inside 100×100μm SU-8 channel.

The simulated spectra in different depth positions are shown in Fig.3.23, plus and minus positions denote respectively higher and lower than the channel center (z=0μm). We can observe that the spectral signal amplitude changes considerably versus z positions, with a maximum at the channel center (black dashed line in Fig.3.22) as expected. However, the spectral shape does not vary significantly with the beam waist position, the frequency peak fd=28 kHz corresponding to the maximal velocity remains pretty much constant all over the scan.
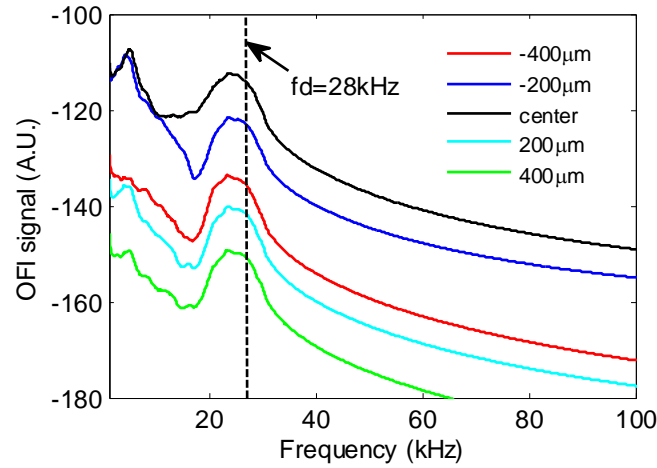
Fig.3.23. Simulated OFI spectra in different laser focus depth positions (from -400, -200, 0(center), +200, 400μmreference to the channel center) at Q=10μL/min. The black dashed line denotes the frequency corresponding to the maximal velocity.

Depth scan measurement spectra are plotted in Fig.3.24. The channel center is located at around 780μm. Just as with the simulation, the waist location only changes the OFI signal level, while the Doppler frequency shift remains constant.

Thus, if it is not possible to perform an actual depth scan with such a small dimension channel, the model can be used to determine precisely the location of the waist in such channel. Such issue is a permanent problematic in microfluidic measurement by means of laser devices while very few solution to address it. To evaluate the OFI signal level variation during the scan, OFI signal amplitudes at fd=28kHz in different z positions are plotted from both simulation and measurement. The evolution of the signal level for both the simulation and the measurement are plotted in Fig.3.25, where a consistent trend all-over the z position range is demonstrated.
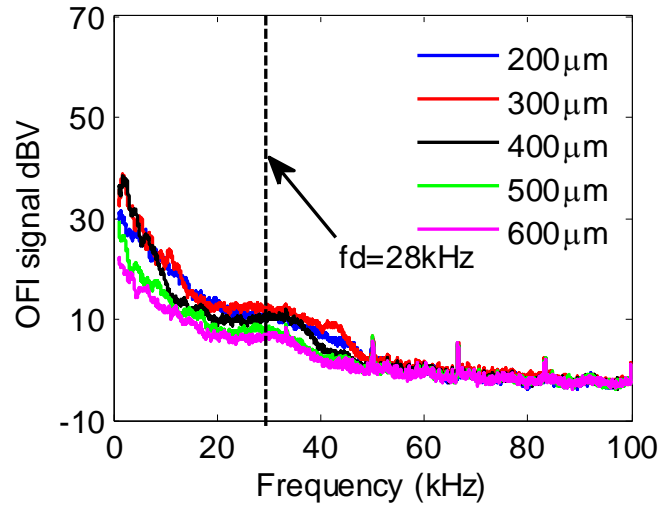
Fig.3.24. OFI signal spectra at different laser focus depth. The black dashed line denotes the frequency corresponding to the maximal velocity.
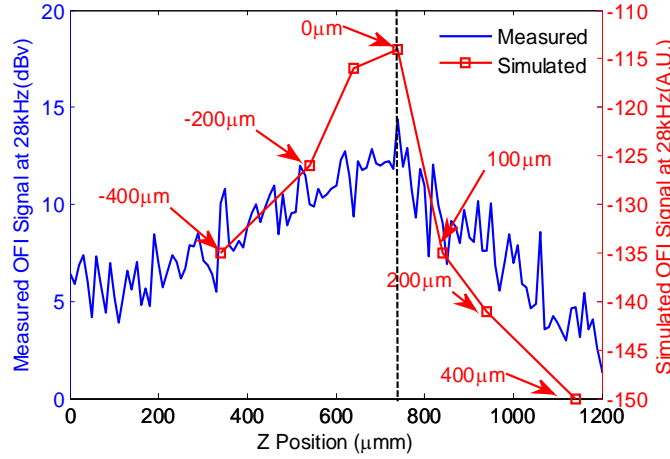
Fig.3.25. OFI signal levels at the maximal Doppler frequency (*fd*=28kHz): simulation: red line (the red square markers show the simulation positions refer to the channel center).Measurement: blue line; the channel center position: the black dashed line.

3.6. Conclusions

In order to validate the multiphysics modeling described in Chapter 2, series of OFI signals in flows are acquired in different configurations. The measurement is compared with the simulation to analyze different parameters effects on the OFI signal, such as the channel size, the particle size and the depth location of the laser beam waist. The measurement results are most of the time in good agreement with the simulation results, successfully proving our numerical method capability[142].

Particularly, for the first time, we predicted a low-frequency Doppler shift induced by the reflection at the back of the channel which has been experimentally validated. Thanks to thin film coating techniques, DF channels with a different interface reflectivity were fabricated to help us confirm the secondary frequency peak origin.

With our model, one can predict the OFI sensor signal in any given microfluidic system even in the case of complicated reactors or flow regions, taking into account channel dimensions or particle size. Furthermore, our method provides a promising tool to optimize the OFI flow sensor performances while designing micro-reactors with indicated optical properties. We believe this modeling tool is a first step to the design of future Lab-on-a-Chip devices requiring precise flow rate or fluid velocity monitoring.

4 Towards compact optical systems with integrated optics

4.1. Introduction

In the previous chapters, we succeeded to simulate the VCSEL-based OFI flowmetry sensor signal in a microfluidic channel and to validate the result in series of experiments. The methodology we deployed offers the possibility of a novel efficient sensor design. We propose here to apply our methodology to the design of a microscale VCSEL-based OFI system thanks to integrated micro-optical elements.

Most of the laser sources used in micro-optical sensing systems require beam collimation (with beam divergence~1°) or beam focusing with a fixed waist size around few tens of microns and working distances ranging from 10µm to few mm. However, the natural beam divergence of a singlemode VCSEL without any extra lenses is often too large (full divergence ranges from 10º to 22º, depending on the technology), which limits its use. To solve this problem, many methods exist to improve the VCSELs output beam shape.

Most of these techniques are based on a hybrid assembly of commercial microlenses arrays on the VCSELs surface, leading to strong requirements on the control of the position of the lenses plane. Consequently, microlenses directly integrated on the VCSEL surface are often preferable. The most typical subject among the VCSEL beam shaping is polymer microlens fabrication due to low cost and ease of use. Various approaches have been reported, such as thermal photoresist reflow[143], deep lithography by protons[144], LIGA process[145], photopolymerization[146] or ink jet[147]–[150]. In all cases, it is necessary to first insert a transparent top-flat pedestal between the VCSEL chip and the microlens in order to superpose the back focal plane of the lens with the VCSEL plane. Similar methods have been proposed by several groups [151], [152].

Pedestal and microlens can be realized with the same or a different material (polymers). A trade-off has to be found on the pedestal height dependence of the VCSELs array density and of the initial and the aimed optical properties of the laser beam. Taking into account the respective numerical apertures of the VCSEL source and of the microlens that can be usually fabricated, the typical pedestal height has to be at least higher than 90µm (see Fig. 4.1).
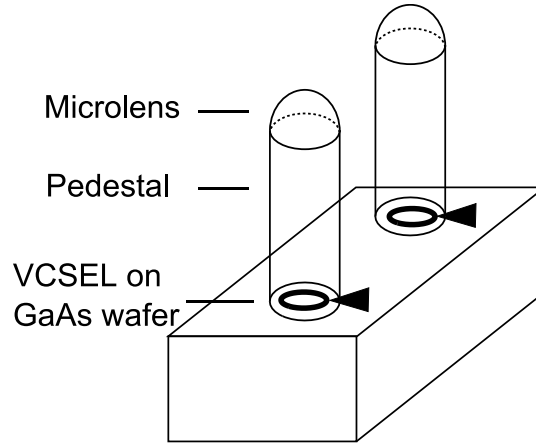
Fig.4.1. Principle of lens integration on VCSEL wafer using a local dispending method coupled to high aspect ratio cylindrical SU-8 pedestals: the low viscosity polymer is self-centered on the top of the pedestal owing to surface tension properties.

The most efficient methods for lens integration on VCSELs are based on liquid polymer drop-on-demand techniques, as they offer numerous advantages such as high flexibility, wafer-level and maskless technology, as well as high surface quality (no contact with a mold). In 2005, A. Nallani et al. first associated ink-jet printing technique to SU-8 cylindrical pedestals priorly defined by photolithography for VCSEL beam focusing and exploited lens self-positioning [17]. More recently, V. Bardinal et al. developed an alternative low-volume liquid deposition technique based on a simple robotized silicon-cantilever spotter and also demonstrated precise positioning and self-alignment of the curable microlens on SU-8 pedestals [18]. In 2010, using the same micro spotter deposition technique, the LAAS-CNRS successfully manufactured polymer microlenses to reduce VCSEL beam divergence down to 1.2° (half angle at 1/e²) [19]. However, with this "passive" method, the only way to tune the focal length for a given diameter was to change the lens material or the applied surface treatment. Inkjet printing is more

versatile, as large changes in lens shape are possible by simply modifying the number of printed polymer droplets.
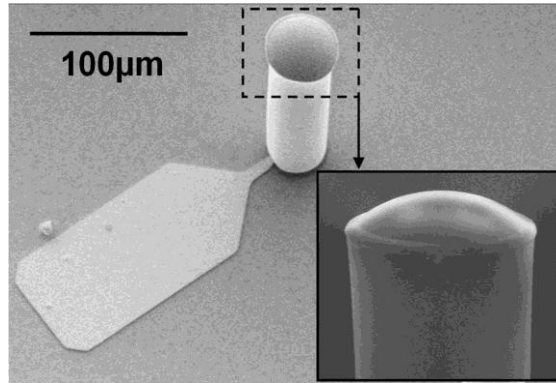
Fig.4.2. SEM image of a spotted lens on a SU-8 pedestal on a singlemode VCSEL. Inset: SEM image of the microlens self-centered on SU-8 cylindrical pedestal

Considering the existing microfabrication techniques and the fact that inkjet printing technique is now available at LAAS, in this work we implemented a miniaturized optical component involving a microlens jetted on a polymer pedestal integrated directly on a VCSEL chip as a real compact OFI flowmetry sensor system. A compact and robust microfluidic platform including micro-scale channel chip including also integrated microlenses and metallic shell is also designed as the microfluidic reactor.

The chapter is constructed as follows: first, Gaussian beam propagation and transformation theoretical principles through the optical elements are presented. Second, for microlens designing, the sensor system is simulated using ZEMAX-EE software to optimize VCSEL beam collimation. Third, the fabrication procedure of each micro-scale component is described in detail. We emphasize on the technological issues we had to solve to fabricate all parts. In particular, we discuss the use of commercial dry epoxy photoresist films (DF-1000 series) instead of standard SU-8 photoresist and of direct laser writing instead of standard photolithography. Fourth, the electronic and optical characteristics are investigated to analyze the system performance. At last, the OFI flowmetry measurement is performed with this new compact system.

4.2. Optical design and ZEMAX simulation of integrated optics based OFI flowmetry sensor

In order to decrease the complexity and to reduce the system size, the whole miniaturized OFI sensor system is designed as Fig.4.3. The system involves two parts: first, a collimated VCSEL-based integrated optical arrangement on a printed circuit board (PCB); second, a custom platform involving a microfluidic chip and a metallic frame.
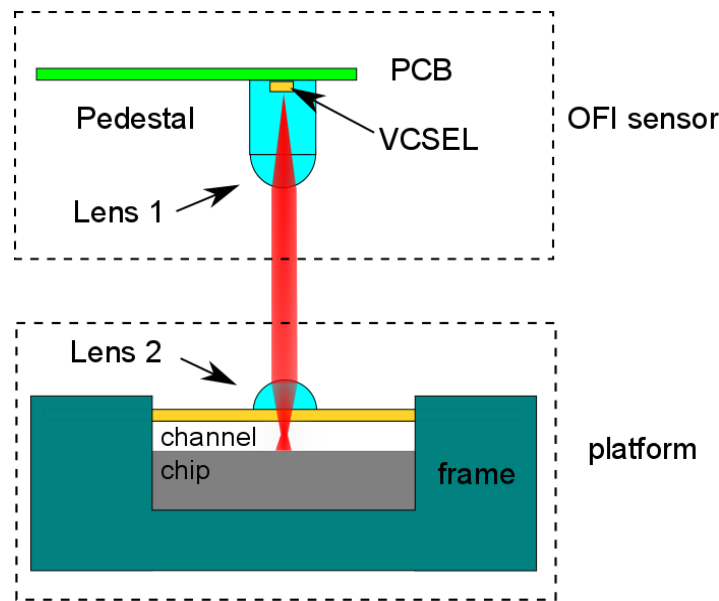
Fig.4.3. Schematic of the miniaturized OFI flowmetry sensor system involving the integrated optical arrangement on VCSEL and a microfluidic platform based on a microchip. Miniaturized OFI sensor includes the PCB, an 850nm VCSEL laser chip with polymer pedestal and collimating microlens. Fluidic platform involves a focalizing microlens, photoresist channel chip, and metallic frame.

This geometry presents many advantages. First, it is very compact as it does not require any macro-optical elements. Second, as the VCSEL beam is collimated, the distance between the source and the channel is not critical to get very easily a well-focused spot (size < 20µm) at the channel center.

4.2.1. Gaussian propagation and transformation fundamentals

Here, the laser beam propagation and transformation fundamentals are presented to give a theoretical framework for the VCSEL-based optical system designing. The Gaussian

beam propagation and transformation through the optical system in the paraxial optical system is well known. The $1/e^2$ intensity spot size $w(z)$, the radius of curvature $R(z)$ at an axial position, and far-field divergence angle θ (half-angle at $1/e^2$) are related to the waist size w_0 and the distance from the waist z:

$$w(z) = w_0 \sqrt{1 + \left(\frac{z}{Z_R}\right)^2} \tag{4.1}$$

$$R(z) = z\left[1 + \left(\frac{Z_R}{z}\right)^2\right] \tag{4.2}$$

$$Z_R = \frac{\pi w_0^2}{\lambda} \tag{4.3}$$

$$\theta \approx \frac{\lambda}{\pi w_0} \tag{4.4}$$

Z_R is the Rayleigh length of the laser, where the beam size $w(Z_R)$ is $\sqrt{2}$ times of the waist radius w_0.

When a Gaussian beam passes an optical element, the spot size and radius of curvature can be specified with a single $q(z)$ parameter which is described by transforming its parameters in ABCD law[154], [155].

$$\frac{1}{q(z)} = \frac{1}{R(z)} - j\frac{\lambda}{\pi w^2(z)} \tag{4.5}$$

$$\frac{1}{q'} = \frac{Cq_0 + D}{Aq_0 + B} \tag{4.6}$$

$$M = \begin{bmatrix} A & B \\ C & D \end{bmatrix} \tag{4.7}$$

Where q_0 and q' are the complex parameters at the input and output planes, respectively. A, B, C, and D are the characteristic constants of the transform matrix M between the input and output planes.

As illustrated in Fig.4.4, the laser diode output radiation experiences the polymer pedestal and the microlens. The matrixes M_1, M_2 corresponding to both elements:

$$M_1 = \begin{bmatrix} 1 & L/n_{ped} \\ 0 & 1 \end{bmatrix} \tag{4.8}$$

$$M_2 = \begin{bmatrix} 1 & 0 \\ -1/F & 1 \end{bmatrix} \tag{4.9}$$

L and n_{ped} are the height and refractive index of the pedestal, respectively. F is the microlens focal length.

The new waist radius following the lens can be calculated as:

$$w' = \sqrt{\frac{F^2 w_0^2}{(F - L/n_{ped})^2 + Z_R^2}} \tag{4.10}$$

When $\dfrac{L}{n_{ped}} = F$, w' reaches its maximal value, while the far field divergence θ' gets to its minimum:

$$w'_{max} = \frac{F}{Z_R} w_0 \tag{4.11}$$

$$\theta'_{min} \approx \frac{\lambda}{\pi w'} = \frac{Z_R}{F} \theta_0 \tag{4.12}$$

For collimation, the system parameters should meet the conditions eq(4.13) and eq(4.14):

$$\frac{L}{n_{lens}} = F \tag{4.13}$$

$$\frac{\theta'}{\theta_0} = \frac{Z_R}{F} \ll 1 \tag{4.14}$$
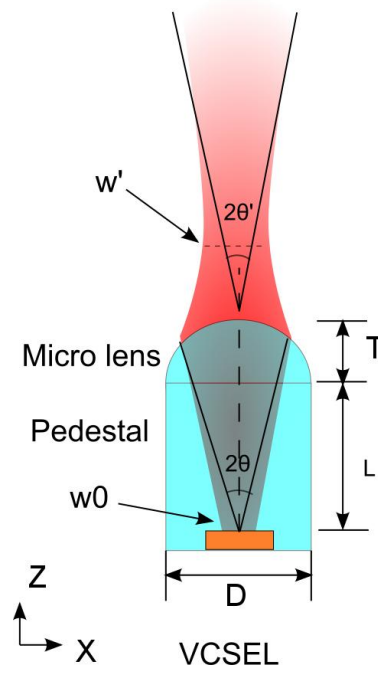
Fig.4.4.Laser propagation through the micro-scale VCSEL-lens system(pedestal + microlens).

We assume that the micro-lenses geometry as plano-convex ones of the perfect spherical profile as shown in Fig.4.5, the radius of curvature ROC and focal length F can be calculated easily with the values of lens thickness T and lens diameter D. The equations are shown below:

$$ROC = \frac{T^2 + \frac{D^2}{4}}{2T} \tag{4.15}$$

$$F = \frac{ROC}{n_{lens} - 1} \tag{4.16}$$

By substitution of eq(4.14) into eq(4.16), the constraint of ROC can be expressed as:

$$ROC \geq (n_{lens} - 1)Z_R \tag{4.17}$$

where n_{lens} is the refractive index of the lens material.
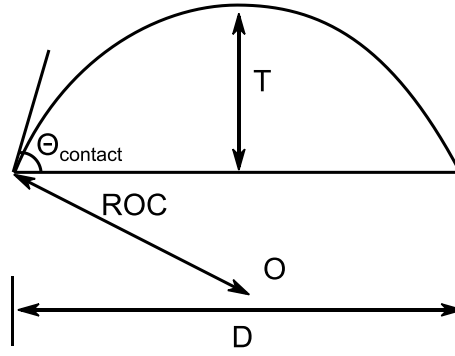
Fig.4.5.Geometrical parameters of the microlens.

Fig.4.6 depicts the relationship between the radius of curvature *ROC* and the lens sag (or height) *T* considering a given diameter *D*.
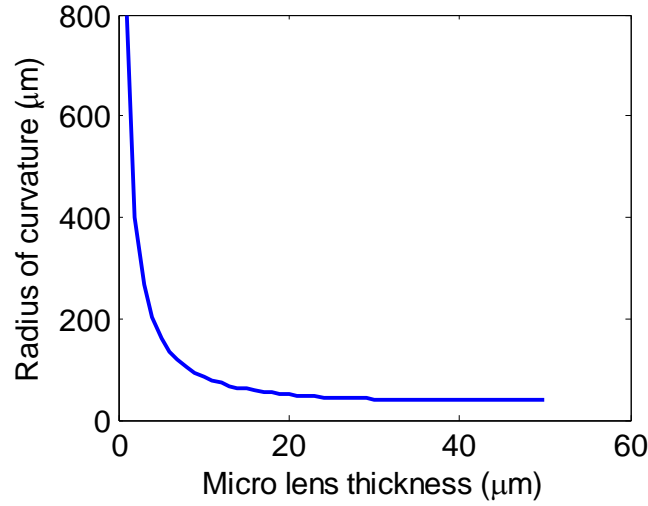
Fig.4.6. *ROC* as a function of *T* for a fixed *D* of 80μm.

The radius of curvature of lens performs a hyperbolic-like trend versus the lens thickness in case of 80μm lens diameter, *ROC* value decreases dramatically when *T* is in the range from 0 to 10 μm, and then the value decreases gradually. Accounting for the lens fabrication technique limitations that will be described later, *T* can vary from 8μm to 35μm. This condition is crucial for lens designing and optimization.

4.2.2. Collimating microlens designing and optimization

The laser collimation condition implied in eq(4.13) is limited to the case of a thin lens. However, in our study the whole system dimension is within 500μm, thus the lens thickness which is in order of several tens of microns indeed affects the laser beam

propagation. Moreover, the aberrations of the microlens should be also taken into account. To solve these practical problems and optimize the VCSEL collimation, a Zemax model is constructed to simulate the VCSEL laser beam propagation in the micro-scale optical system and optimize beam collimation by adjusting the lens geometry.

The whole microsystem is depicted in Fig.4.4, and modeled by ZEMAX-EE software. The system is assumed as a perfect rotationally symmetric system about Z-propagation direction where all the tilts and decenters during the beam propagation are negligible. Accounting the features of the VCSEL chips we used in this study, the microfabrication technical conditions and the material optical characteristics, all the parameters are set as in Tab.4.1. Based on the *ROC* dependence on *T* in eq(4.15), we pick up *ROC* value with *T* by a user-defined ZEMAX-EE programming language (ZPL) macro.

Table.4.1. Parameters values and ranges used in ZEMAX simulation.

Parameters	Values
n_{ped}	1.58
n_{lens}	1.59
λ	850 nm
D_{lens}	80 μm
w_0	2.4μm
θ_0	6.5°
L	90μm to 150μm
T	10μm to 50μm

Geometry ray tracing often requires the dimensions of the objects are much bigger than the wavelength. In such optical simulation approach, interference and diffraction are ignored. However, in our micro-scale system, the effect due to the diffraction cannot be neglected, so the ray-tracing simulation method which has been investigated in Chapter 2 is not of sufficient capability. For the highest accuracy, we employ an alternative simulation function named Physical Optics Propagation (POP) of ZEMAX-EE software

which uses diffraction calculations to evaluate a wavefront transformation. In POP, the beam wavefront is viewed as an array of points and each point offers the complex amplitude information.

Thanks to merit function (MF) in ZEMAX-EE, we can optimize the system by using appropriate operands and targets in the merit function editor. We invoke the Gaussian beam propagation divergence operand "GBPD" (Gaussian beam paraxial divergence) which returns divergence θ' (in Fig.4.4) to assess the lens collimating performance. To approach the operand target to be zero for the desired minimum divergence, MF automatically changes the pedestal height L and lens thickness T to satisfy the target.

Considering the collimating dependence on ROC in eq(4.17) and fabrication technical limitations, the polymer optical elements dimensions constraints are also taken into account. All the necessary operands and targets selected in the merit function editor are shown in Tab.4.2.

Tab.4.2.Merit function operands setting.

Operand	Meaning	Target value
POPD	Physical optical beam propagation (POP)	-
GBPD	Gaussian beam divergence angle	0 °
MNCG (T)	Mini lens thickness T value	10μm
MXCG(T)	Max lens thickness T value	180μm
MNCG(L)	Mini pedestal thickness L value	90μm
MXCG(L)	Max pedestal thickness L value	150μm

The best configurations corresponding to different pedestal dimensions are presented in Tab.4.3.

Tab.4.3. Optimal lens geometry configurations of different pedestal heights retrieved by ZEMAX optimization (assuming an initial $1/e^2$ full divergence angle equal to 13°)

Pedestal height $L(\mu m)$	Pedestal diameter D (μm)	Lens ROC (μm)	Lens height T(μm)	beam diameter at 1mm 2ω (μm)	$1/e^2$full divergence angle2θ (°)
90	80	45	25	66	3.6
95	80	46	22	62	3.5
100	80	48	22	60.8	3.42
105	80	49	21	60.2	3.32
110	80	51	20	58.2	3.24
115	80	52	19	56	3.2
120	80	54	18	54	3.1
125	80	56	17	54	3.01
130	80	57	16	53	2.86
135	80	58	16	50	2.86
140	80	60	15	49	2.76
145	80	62	15	47.5	2.7
150	80	63	14	46.5	2.6

The divergence θ' trend after the optimization against the pedestal height L valuesis plotted in Fig.4.7, we can conclude that the far field divergence decreases with the pedestal height gradually. For optimal collimation, high values of L and ROC should be selected. However, L cannot be increased above 150µm due to technological fabrication limits. The micro-optical element (lens+pedestal) should not have indeed a too high aspect-ratio otherwise it would become mechanically unstable. Therefore, we decided to target the range from 90µm to 130µm for the pedestal height. For these values, a divergence of 3.5° (full angle) should be obtained as well as a spot size of ~60µm at the distance from the lens equal to 1mm (in free space).
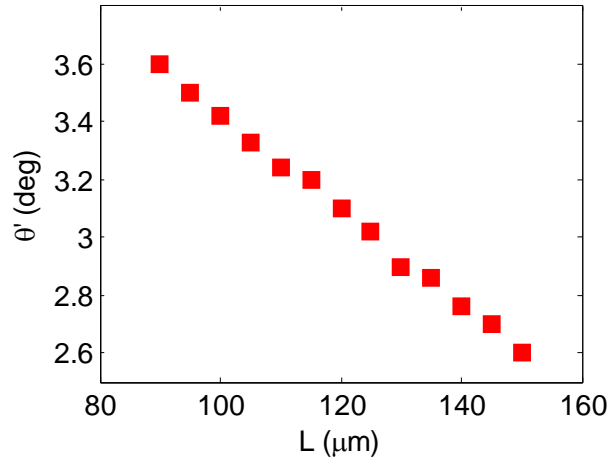
Fig.4.7. Optimized full divergence angle as a function of pedestal height.

4.2.3. Focalizing microlens designing and optimization

Like the collimating lens on the pedestal, we intend to use a similar microlens for the DF channel roof surface to focalize the laser incident beam at the channel center. With the same parameters for collimating lens in Tab.4.1, we simulate the laser incident propagation through the channel as shown in Fig.4.8. Several channel thickness are considered in this study. The best lens geometry configuration is chosen to optimize the focusing spot focused at the center in Tab.4.4. The size of the spot at the channel center can be reduced this way to less than 20μm, thus allowing a spatially-resolved measurement.
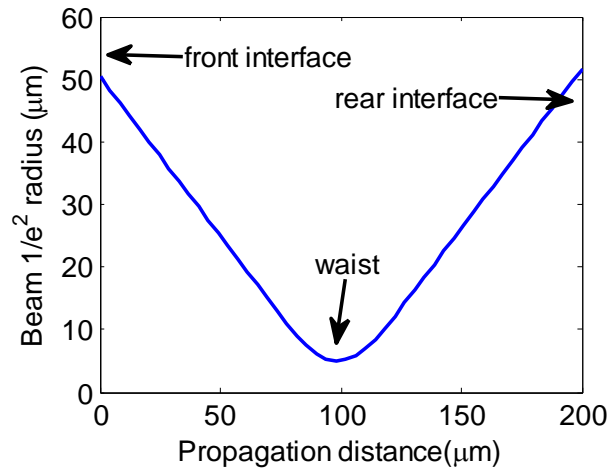
Fig.4.8. Simulated $1/e^2$ radius profile during the laser beam propagation inside the 200 μm height channel full of water with a micro-scale focusing lens of 80μm diameter 16μm thickness and 53μm curvature radius.

Tab.4.4. Optimal lens ROC value for focusing microlens at the middle of the channels (3 different thicknesses tested).

Channel thickness (µm)	ROC (µm)	Lens thickness (µm)	Beam $1/e^2$ diameter at channel center (µm)
50	35	45	15
100	41	33	14
200	53	18	12

4.3. Integrated optics devices fabrication

After the design of the optimal system, we describe and discuss in the following parts all the procedures of the system fabrication.

In this study, we used commercial 850 nm singlemode VCSELs provided by Philips-Ulm (already diced single chips). We decided indeed to integrate the microlens above single chips after dicing and mounting steps, i.e., a post-processing stage, in order to avoid weakening of high aspect-ratio pedestals observed during dicing steps when already fabricated on a whole VCSEL wafer. In the literature, only wafer-scale fabrication based on photolithography was reported up to now. Here we develop a new kind of process that makes the use of small-sized commercial VCSELs chips possible. With this approach, the dicing step occurs before pedestal fabrication with a lower risk of delamination from the VCSEL chip.

The VCSELs we use are referred as ULM850-A4-PL-S46XZP in Fig.4.9(a). This VCSEL is an oxide-confined top emitting GaAs diode performing a singlemode emission at 850 nm. The full $1/e^2$ far-field beam divergence angle is measured to be about 13°. It presents the advantage of having a stabilized polarization thanks to a shallowly etched surface grating (see Fig.4.9(b)), avoiding polarization switching at different injection currents[156]. We first mount the VCSEL on a homemade PCB as depicted in figure 4.9 (c), so that the system can easily be inserted in a wide variety of sensing systems.
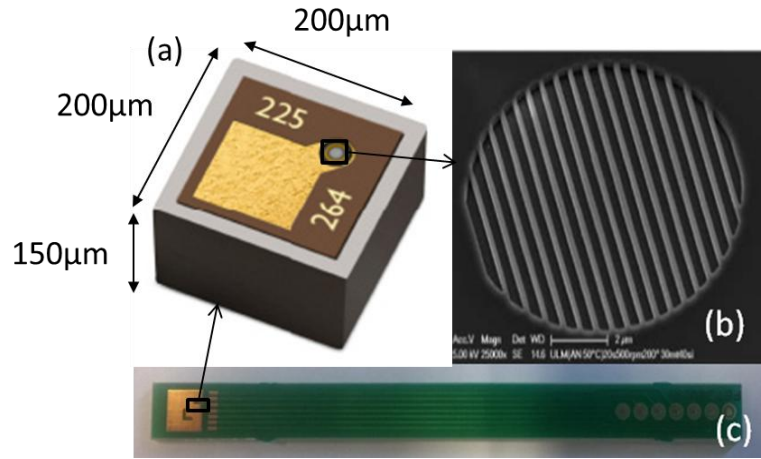
Fig.4.9. (a) Top view of the VCSEL chip. (b) Photograph of the polarization stable grating on the top VCSEL surface before lens fabrication. (c) Custom made PCB on which the VCSEL chips are mounted.

4.3.1. VCSEL based micro-scale lens fabrication

We developed a new fabrication process to integrate a collimation lens at a post-processing stage on a mounted single chips with reduced dimensions (length 200µm, width 200µm, depth 150µm) thanks to combined micro-optical fabrication technologies: soft thermal printing, direct laser writing and inkjet printing,

The complete procedure of the micro-optical system fabrication on a single VCSEL chip is illustrated in Fig.4.10. The chips are first mounted on a PCB (a) and two dry thick photoresist films (2XDF-1050/nominal thickness of each film: 50µm±3µm) are deposited and printed on the VCSEL surface by a new technique named Soft Thermal Printing (b and c) to get a 96µm high pedestal. Then, thanks to the accurate alignment and to direct UV laser writing provided by the DILASE 750 setup we used, high aspect-ratio cylindrical pedestals are photo-patterned at the top of VCSEL chips (typical diameter: 80 µm, typical height: 120 µm) (d) with a good centering with the VCSEL source located underneath (±1µm). After pedestal development and curing, polymer lenses can be fabricated on the top of pedestals by inkjet printing of thermocurable liquid droplets (f), as for the case of large wafers. After lens thermal curing (g), the VCSEL chips are bonded to the PCB circuitry (h) and tested.
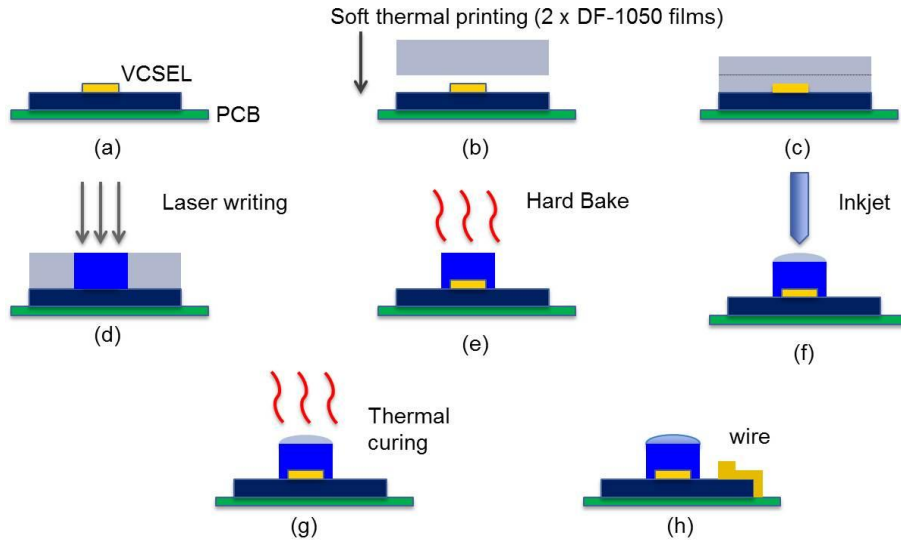
Fig.4.10. Procedure of VCSEL based micro-optical system fabrication: (a) mounting the VCSEL chip on the PCB (b) place the DF-1050 films on VCSEL surface (c) soft thermal printing (d) UV laser writing for pedestal definition (e) develop and thermal curing (f) droplet inkjet for polymer lens fabrication (g) thermal curing (h) wire bonding.

4.3.2. DF-1050-based pedestal fabrication on single chip

The standard way to fabricate the flat pedestal layer is using spin-coating of highly viscous resists, such as SU-8 photoresists[25]–[27]. However, during the spinning process, undesired annular edge beads at sample periphery arise that can be higher than 30 µm for a targeted height of 100 µm. This induces a great thickness inhomogeneity of the resist layer and the creation of an air gap between the photomask and the resist, leading to optical diffraction effects during the UV photolithography step and to poor pattern definition. Moreover, in our work, the VCSEL chips are quite tiny (length 200µm, width 200µm, depth 150µm), and standard spin-coating is not applicable at all.

a. Soft thermal printing of dry films instead of spin-coating

To fabricate such a high aspect ratio polymer pedestal together with good thickness uniformity for lens positioning convenience, we choose a commercial dry film photo resists(DF-1050) as the pedestal material. DF-1000 series is more and more used for microfluidics fabrication as they offer many advantages, such as good flatness, good conformability, excellent adhesion to any surface, no formation of edge beads, low cost, short processing time and near vertical sidewalls[160]. However, these films are

normally deposited using lamination that consists in passing the film stacked on the sample between two rotating rollers under pressure. This standard film lamination is not applicable to small and fragile VCSEL chips. A method called "soft thermal printing" (STP) has been thus developed at LAAS to satisfy this tricky technical problem thanks to the use of a nano-printing set-up equipped with soft flexible membranes (Fig.4.11). Temperature and pressure applied to the membranes were optimized (16 psi/ 40°C) to lead to the best thickness profile with no delamination of the film. Compared with the traditional liquid resists spinning technique, the resulting thickness deviation of a micro layer based on DF-1050 is only 3% (for a 25×25mm² surface sample) compared to more than 40% for SU-8 standard spin-coating (Fig.4.12) [161]. Besides the perfect thickness uniformity, this technique also induces other advantages such as safety for the VCSEL chip, less time-consuming and less cost.
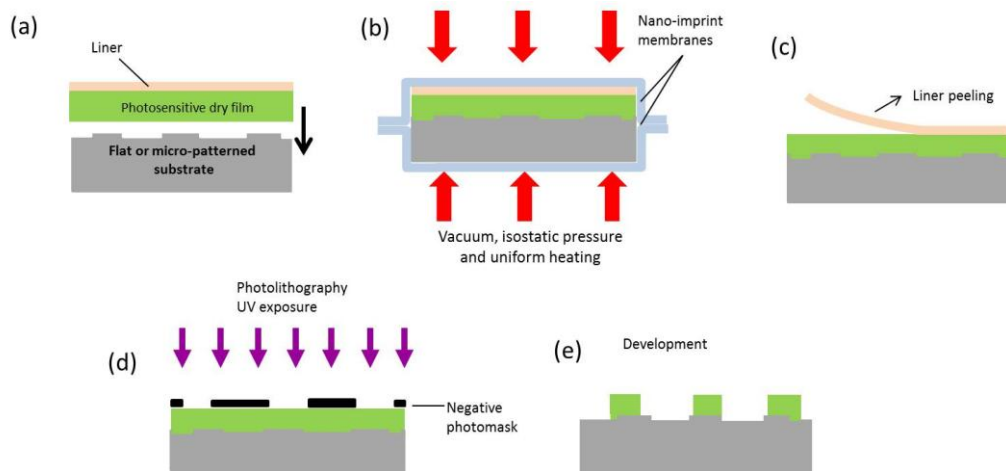
Fig.4.11. Principle of soft thermal printing of a dry film using nano-imprint equipment with a double membrane system: (a) Film cutting and positioning on the sample, (b) soft thermal printing between the two flexible membranes, (c) liner peel off, (d) UV photolithography, and (e) development.
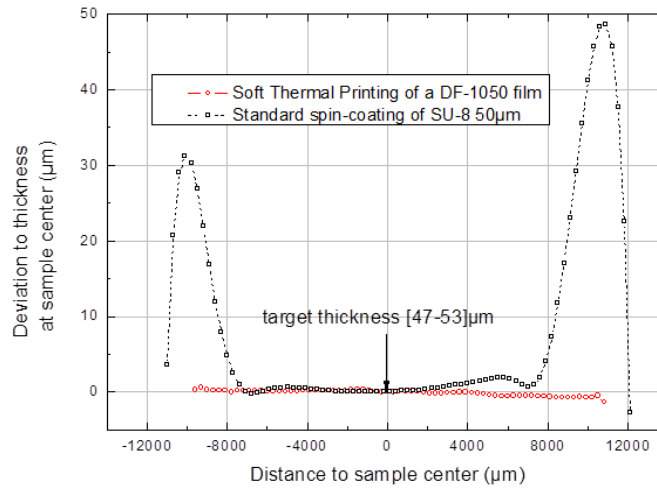
Fig.4.12.Typical uniformity profiles obtained with STP compared to spin coating on a 25×25mm² sample in optimal printing conditions (pressure: 16psi, temperature: 40°C).

b. Laser writing instead of photolithography

After film transfer, a direct UV laser writing technique is used for pattern definition as standard photolithography is only applicable on large wafers. Laser writing can be applied to unconventional samples and lead to similar precision in pattern definition than photolithography (±1µm) provided the film thickness is well known. The vertical position of the laser beam during writing is indeed a critical parameter to get the aimed shape. Prior to this study, preliminary tests have been led by J.B. Doucet and P.F. Calmon from TEAM service at LAAS-CNRS on VCSEL multimode arrays including 20 adjacent devices fabricated at LAAS-CNRS (of length 3mm, width 500µm, depth 500µm). The results can be seen in Fig. 4.13. A good control of pedestal's height and shape is achieved. This is the first time that microlenses are integrated at a post-processing stage on a VCSEL array already mounted on a PCB.
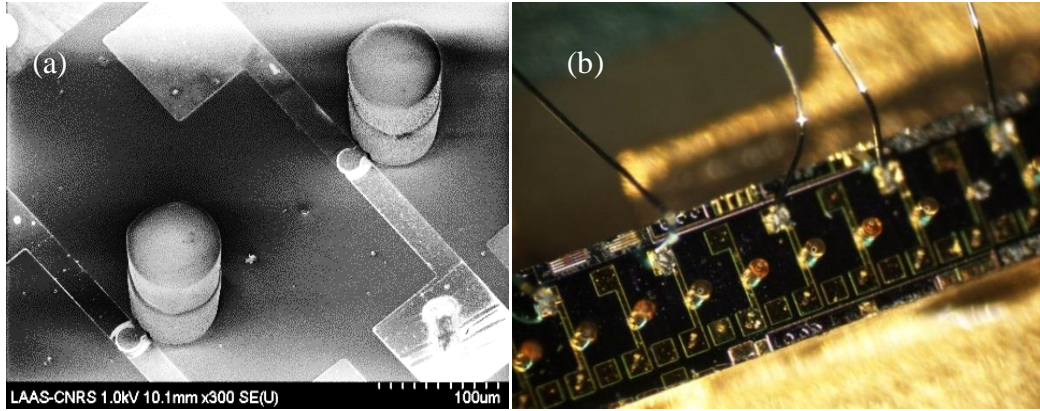
Fig.4.13. (a) SEM image of pedestals integrated on 1×20 VCSEL array mounted on a PCB thanks to double soft thermal printing of 2 DF-1050 films and to laser writing. (b) Optical image of the array after bonding.

c. Problems encountered on single chips

Before the present study, soft thermal printing and laser writing have not been tested on sample surfaces as low as those of the single VCSEL chips (surface: 200μm×200μm). Applying the above-mentioned optimized conditions, we obtained a much lower thickness than expected (~60μm instead of 96μm) and laser writing conditions were not appropriate anymore (Fig 4.14).
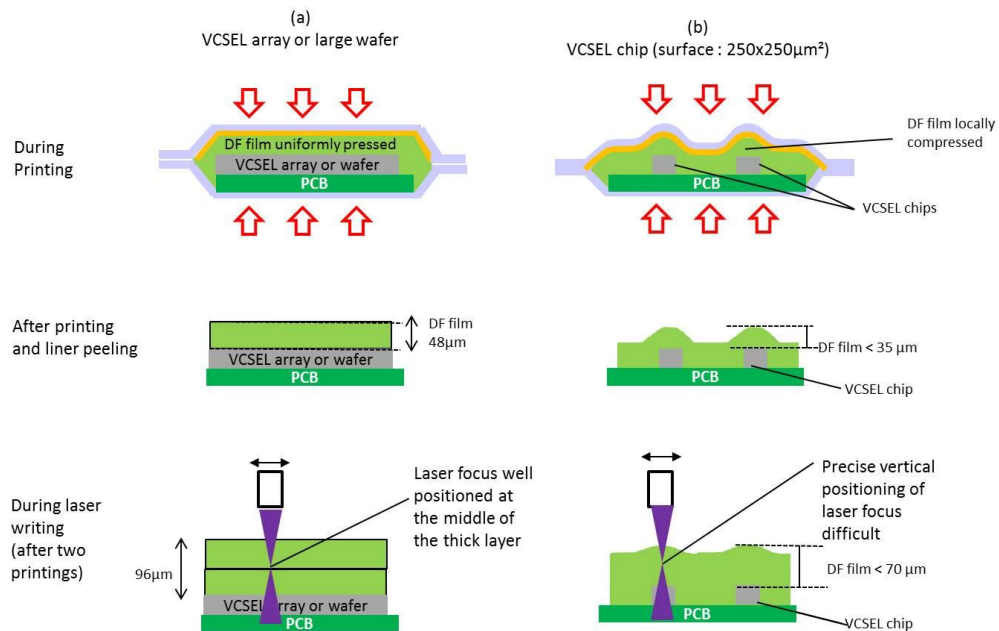
Fig.4.14.Comparison between fabrication on a large sample (a) and on a single VCSEL chip (b). In the last case, printing conditions are modified and as a result, the final film thickness is smaller and laser writing conditions are disturbed.

This problem was accounted for the higher equivalent pressure applied to the chip's small volume during printing, leading to a strong film deformation above the chip. Decreasing the printing pressure helped to increase the final thickness. However, we observed a lack of adhesion in case of a too low pressure. Finally, we found a tradeoff by printing 3 DF-1050 films, instead of 2, at the lowest pressure possible (5 psi). In this new method, cylinder pedestal of high aspect ratio can be fabricated. The first fabricated pedestals on the VCSELs chips are depicted in Fig.4.15, the shapes are not yet a perfect cylinder. The top part diameter is slightly bigger than the one of the lower part. This peg-top shape can be attributed to a non-optimal vertical position of the laser focal point during writing due to uncertainties on the final thickness during process optimization. However, this imperfect shape does not disturb the laser beam propagation. Further optimization of laser writing conditions is under progress since now a reproducible pedestal height is achievable and can be taken into account (Fig. 4.16).
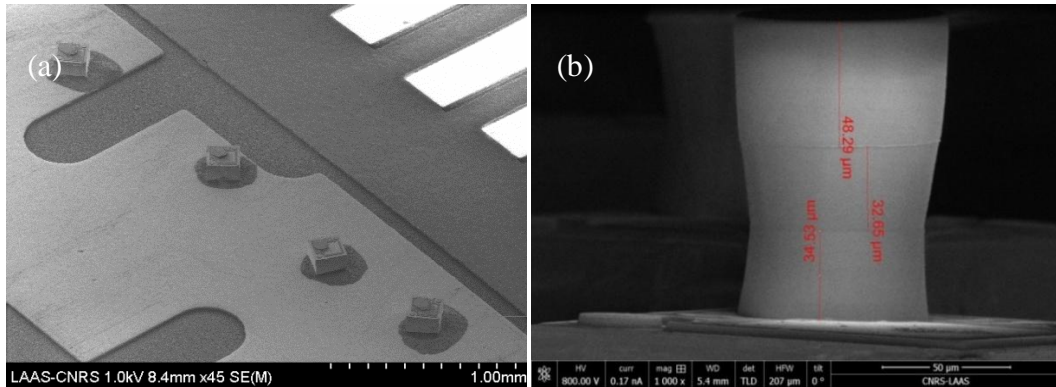
Fig.4.15. SEM images of the single chips mounted on the PCB.(a) general view (b) Pedestals fabricated with 3 printed films on each VCSEL chip.
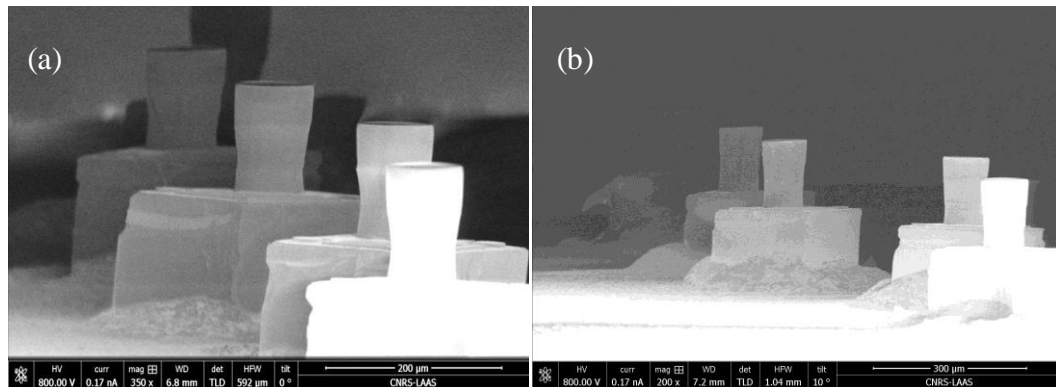
Fig.4.16. (a) SEM images of the single chips mounted on the PCB after optimization of laser writing. (b) The pedestal shape is closer to the one of a cylinder.

4.3.3. Microlens deposition

We employed inkjet printing technique to fabricate the microlens on the top surface of DF-1050-based pedestals for laser output beam shaping. Inkjet printing technology has attracted significant attention in microfabrication domain[162] because it reduces the number of manufacturing process steps and material use, thus offering an efficient, simple and a cheap alternative to the conventionally used photolithography technique. Many related publications based on this technique have been reported in microlens fabrication[147]–[149], [163]–[165]. The printing setup is shown in Fig.4.17. We use the piezoelectric-actuator-based, "drop-on-demand" (DOD) mode of ink-jet printing, where a volumetric change of the ink is induced by applying a voltage pulse to a transducer coupled to the ink fluid. This volumetric change produces a small ink droplet from the nozzle of 30 μm in diameter (MicroFab technology, inc., http://www.microfab.com/). The printing may be accomplished using a translating stage to move the substrate to desired locations. Finally, the microlenses with good spherical profile is printed on the top of the pedestal.
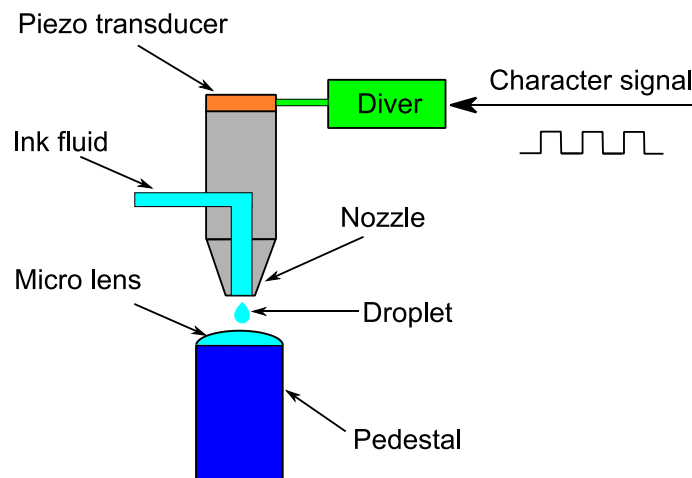
Fig.4.17. Schematic diagram of the inkjet printing setup used to fabricate microlenses (http://www.microfab.com/).

SU-8 photoresist cannot be used as the ink in our inkjet set-up, because it can lead to nozzle clogging. As a result, we had to develop a home-made thermocurable formulation with a low viscosity designed to be suitable for our set-up. This formulation called Cipol T leads to a hard polyester material after curing and is based on organic

acids and alcohols derivatives. My main contribution to this work consisted in taking part in the thermal curing optimization in order to obtain solid and high-quality hemispherical droplets. After this step, droplet deposition has been tested on pedestals and lens dimensions were measured as a function of the number of printed droplets.
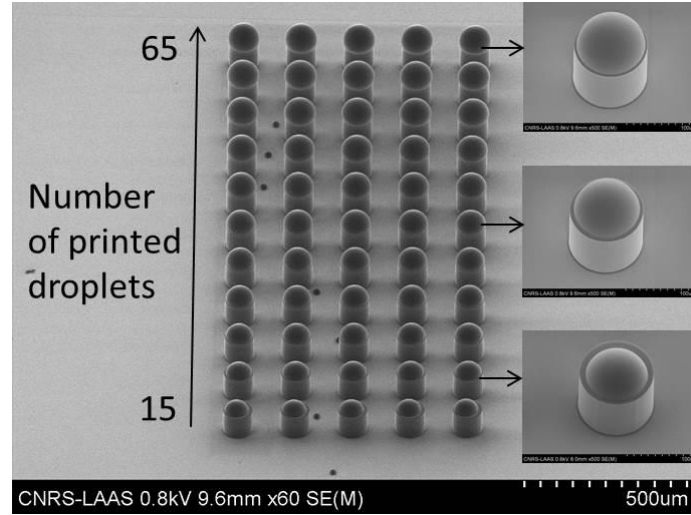
Fig.4.18. SEM image of contact angle variation on epoxy pedestals as a function of the number of printed droplets.

The lens height T and the contact angle $\alpha_{contact}$ of the lenses are characterized using a confocal microscope in Tab.4.5. By varying the ink droplet numbers, different microlens geometries are obtained.

Tab.4.5. Contact angles and lens heights of different droplet numbers.

Lens diameter D	80 μm			
Numbers of droplets	4(min)	8	12	18(max)
Contact angle $\alpha_{contact}$	17°	42°	62°	79°
Lens height T	6 μm	15 μm	25 μm	33 μm

From eq(4.15), the *ROCs* of the microlens are calculated corresponding to different droplet numbers, the more droplets the lower ROC. Fig.4.19 depicts the *ROC* and *T*

trends with droplet number. The control of the *ROC* is fundamental for VCSEL output beam collimation.
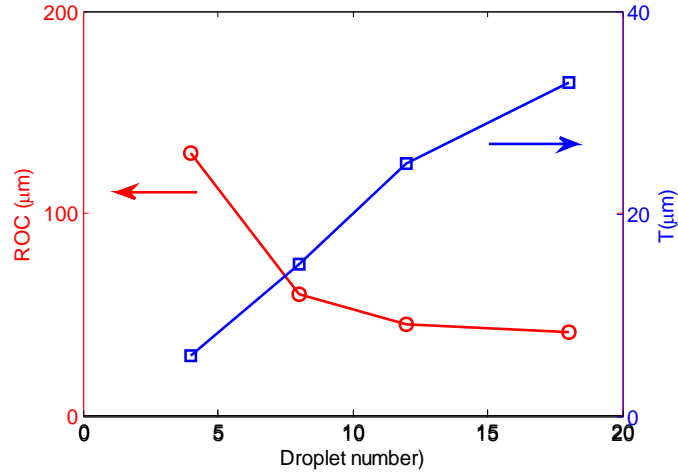
Fig.4.19. *ROC* and *T* variation as a function of droplet number. The red line with circle marks represents the *ROC* value and the blue line with square marks denotes the T value.

Finally, microlenses were deposited on the first series of pedestals printed on VCSEL chips. Fig.4.20 demonstrates the low surface roughness of the microlens, all the microlenses have an 80 μm diameter and are well aligned with the pedestal of the same diameter. In this first trial, the measured *ROC* is 58 μm and the lens height is 16 μm. This should lead to a reduction by a factor higher than 2 of the initial divergence and to a beam size of ~40μm at a 500μm distance. Further optimization of the lens dimensions is under progress on a second production series.
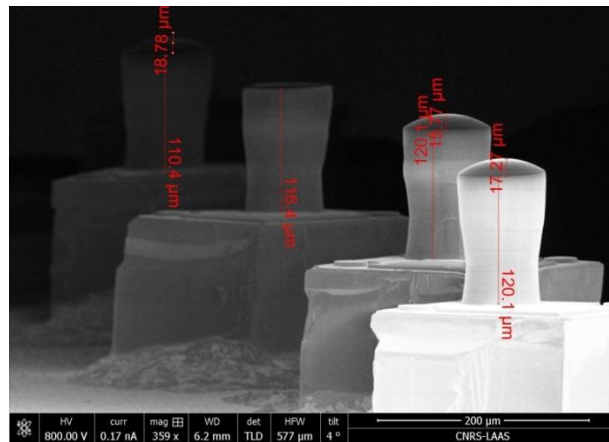
Fig.4.20. The first trial of microlenses deposition on the first series of DF-1050 pedestal sprinted on VCSEL chips using inkjet printing technique.

4.3.4. Microlens characterization

To analyze the collimation capability, we use a photodiode to assess the $1/e^2$ divergence angles of both bare VCSELs and lensed VCSELs, the results are shown in Fig.4.21. Full $1/e^2$ divergence angle of the lensed VCSEL (in blue) is 5.5° which is less than half of the bare VCSEL 13°, as expected for this first series. The applied current on both VCSELs was 3 mA, i.e., approximately at twice the threshold value.
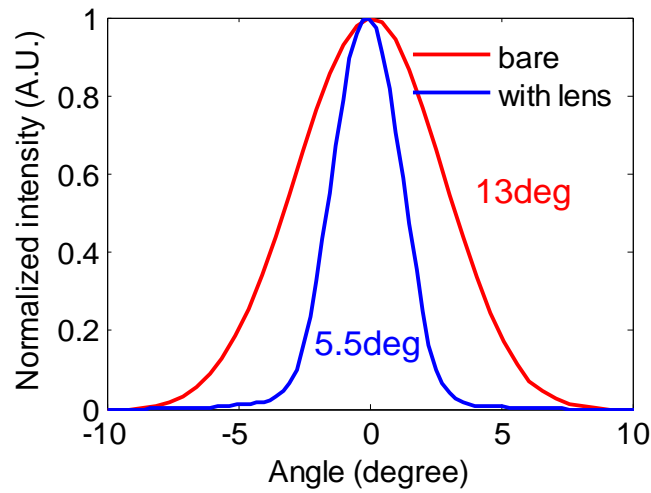
Fig.4.21. Measured $1/e^2$ divergence angles: red line is the bare VCSEL without microlens; blue line denotes the angle of the VCSEL integrated with microlens (applied current: 3mA)
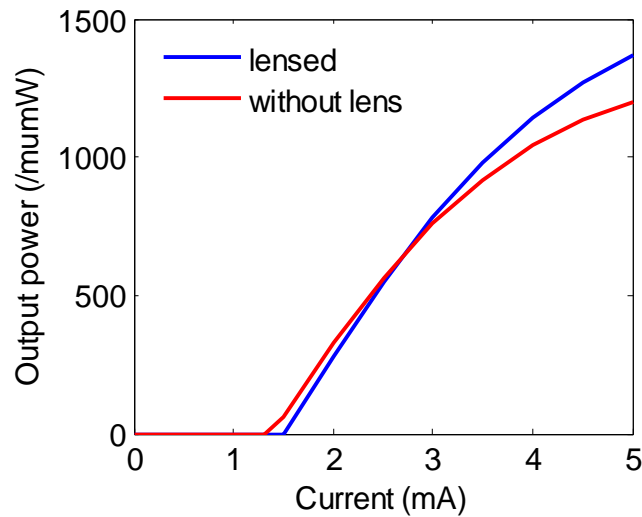
Fig.4.22. Light-current curves of VCSEL before and after lens integration.

As seen in Fig 4.22, lens integration leads to a slight modification of the L-I-V curve, the threshold current of the VCSEL without lens is 1.3 mA, while the one in lensed VCSEL is 1.6mA. This phenomenon is due to the integration of polymer pedestal at the surface and is sensitive to pedestal dimensions[166], [167].
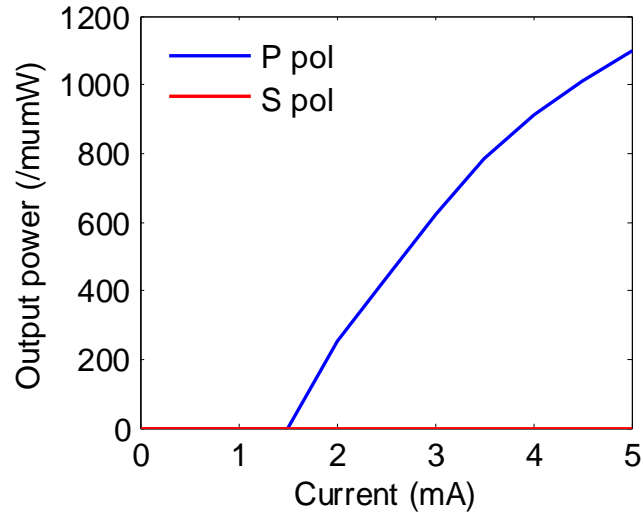
Fig.4.23. Polarization-resolved L-C current of lensed VCSEL. The blue curve is P polarization direction, and red line is S polarization direction which is perpendicular to P direction

In Fig.4.23, one can see that the lensed VCSEL performs a polarization-stable operation thanks to the grating, even if this grating was designed for the case of air as an output medium rather than a polymer. To conclude on this part, we demonstrated for the first time the post-processing integration of a microlens on a single VCSEL chip thanks to dry film technology and direct laser writing.

4.3.5. Microfluidic platform fabrication

We employ a custom-made microfluidic platform as the reactor holder and inlets/outlets ducts connectivity which is illustrated in Fig.4.24. It consists of two elements: metallic frames which are screwed together thus to maintain the polymer microfluidic channel chip and the rubber O-rings as connections. The frame size is 14mm×20mm. This robust apparatus enables both easy handling when changing the channel chip and good protection of the fragile channel chip during the assembly operation and the flow rate measurement.

Fig.4.24. Photograph of the microfluidic platform.

4.3.6. Microfluidic channel designing

This fabrication approach is also based on the use of new kind of dry film photoresists with calibrated thicknesses, (DF-1005 5μm, DF-1020 20μm and DF-1050 48μm), which have been reported useful and interesting for sealing channel using standard lamination[168]–[171].

We designed channel chips of different channel heights: 48μm (DF-1050), 96μm (2×DF-1050), and 192μm (4×DF-1050) by stacking several films on a glass wafer of 4'' in diameter. The channel pattern array of different widths is depicted in Fig.4.25.
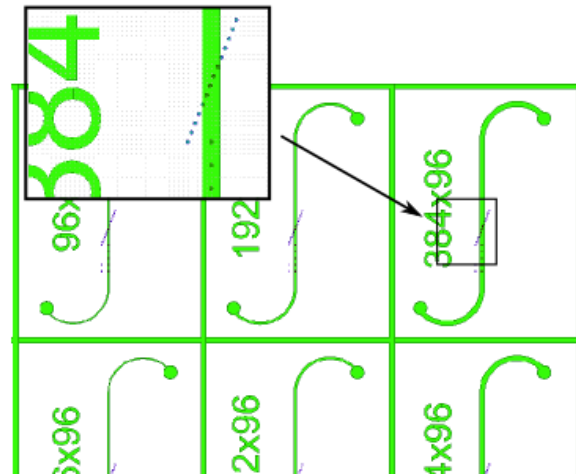
Fig.4.25. Schematic of the microchannel mask pattern design by software including channel pattern and microlens array location (as the inset). Lens diameter is 80μm.Lenses location will allow scanning laterally the channel with an interval of 20μm.

Before the channel chip fabrication, some necessary preparation treatments are applied on the glass wafer. First, we apply a layer of metal by PVD and then photolithography

and chemical etching to make the alignment marks for the following steps. Second, we implement lamination of the protection layer and drilling holes for inlet/outlet port.

In Fig.4.26, all the treatments and technical procedures of 48 µm thickness channel fabrication are described in detail. First, a SAM (Self-Assembled Monolayer) grafting is first applied for improving adhesion of DF film on the glass substrate. The first DF-1050 film of 48 µm thickness is laminated as the channel wall layer. UV exposure with the above-described photolithography mask is then applied to etch the channel pattern. Then, a second DF-1020 film of 20µm thickness is laminated and aligned with the pattern to be the roof cover layer. To prepare lens deposition, we are developing a localized hydrophobic surface treatment on the top DF-1050 layer by grafting FDTS(Perfluoro-decyl-trichlorosilane). This way, the lens will be also self-positioned despite the surface is flat (no pedestal in this case). At the end, microlenses will be deposited using inkjet printing and cured to be solid using the same thermal method than for lensed-VCSELs. This fabrication part is still undergoing and microchannels including microlenses at their surface are not yet available.
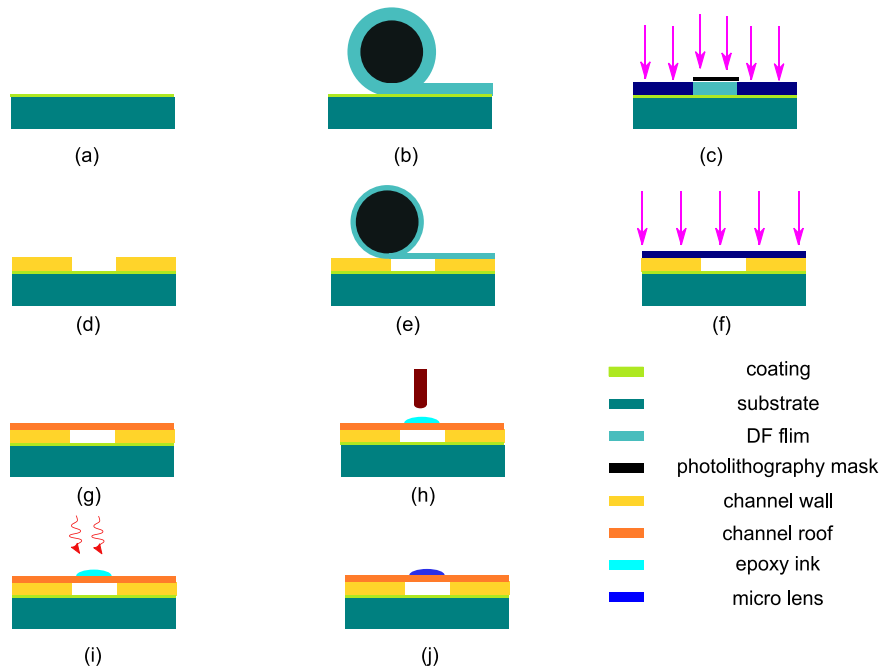
Fig.4.26. Channel chip fabrication procedure: (a) SAM grafting (b) first DF film lamination (c) UV exposure (d) development (e) second film lamination (f) UV exposure (g) photolithography and FDTS grafting (h) microlens inkjet printing and (i) thermal curing.

An image of microfluidic channel fabricated with this method can be seen in Fig. 4.27.
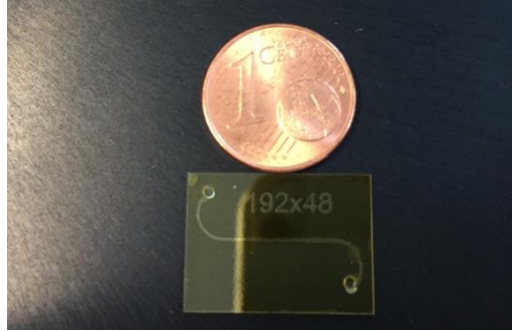
Fig.4.27. Photograph of the microfluidic channel of192μm×48μm (before lens fabrication).

4.4. OFI velocimetry implementation

In the following section, OFI velocimetry measurements performed with the lensed-VCSEL are performed. The experiment results are presented and discussed to evaluate the system capability.

4.4.1. Preliminary experiments: evaluation of the VCSEL with integrated lens on a rotating disk

The setup used for visibility measurements of 670nm VCSEL mounted on TO46 holders (in Chapter 3) could not be used for lensed-VCSELs on PCB, because of a too short working distance. Nevertheless, prior to display the lens integrated on VCSEL in a microfluidic system, a first test was performed on a rotating metallic disc (Fig 4.28) without any extra optics. The distance between the disk and the laser source is roughly 30 mm thus leading to a spot diameter on target around 5mm.
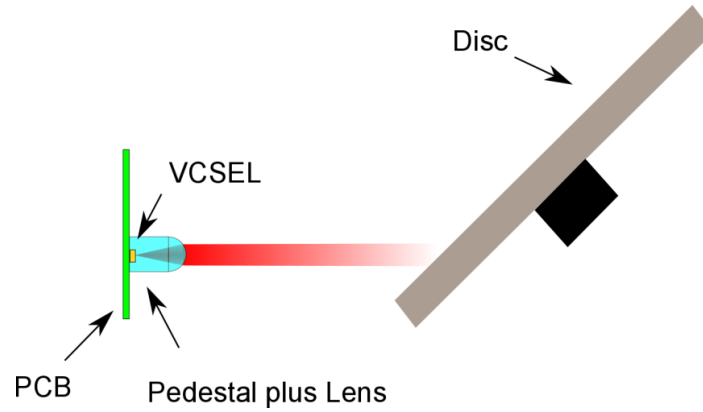
Fig.4.28. Experimental setup for preliminary OFI velocimetry measurement with a bulk rotating disc at a distance of around 30mm from the sensor.

The disc is mounted on a step motor which velocity is controlled. Thus the OFI signal spectrum exhibit a unique frequency peak which broadening is due both to the diverging incident radiation and to the distribution of velocity within the spot on the disk surface (Fig. 4.29).
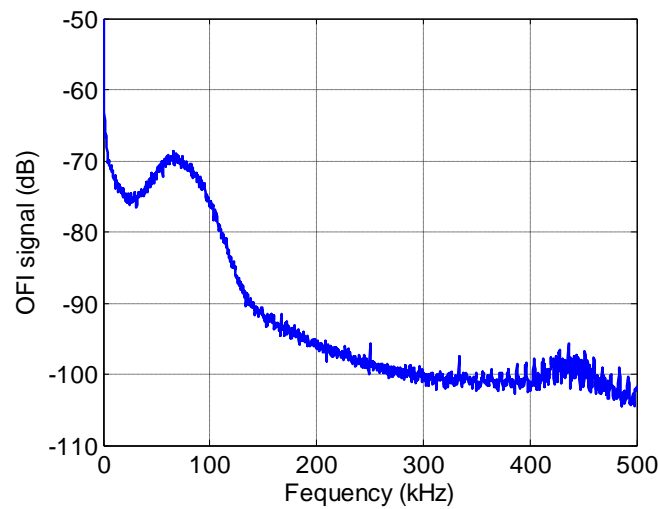
Fig.4.29. OFI signal frequency spectrum of the integrated sensor system in the preliminary OFI velocimetry measurement.

This measurement shows the interest of the integrated lens, as the visibility (~12 dB) of the Doppler peak is pretty acceptable and much better than what has been observed previously with a different VCSEL without lens[172].

4.4.2. Microfluidic flow measurements

Now, the integrated OFI sensor is applied in flow measurement inside micro-channels, the setup is sketched as the beginning of this chapter in Fig.4.3. A 192μm×48μm rectangular cross-section channel we have designed in Fig. 4.30 is employed as the fluidic reactor. The angle between the laser axis and normal to the channel is around 10º to approach the minimum distance from PCB to the channel chip. In the inset, the distance from the sensor to the channel surface in around 500 μm, and the beam diameter in the channel center is around 120 μm(bare) and 40 μm(lensed), respectively.

The 4.89μm PS solution with concentration 0.1%w/t is pumped into the channel by a syringe pressing pump (PHD 22/2000 Harvard Apparatus) just as presented in chapter 3. We vary the flow rate from 1μL/min to 10μL/min. Such low setting allows avoiding damaging the channel.
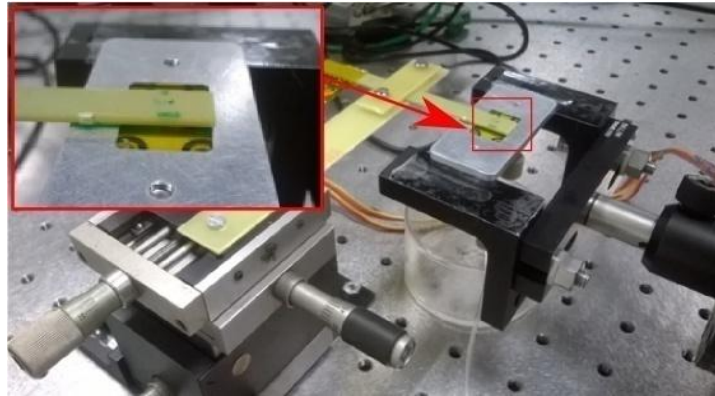
Fig.4.30. Schematic of the integrated OFI sensor setup in microfluidic measurement. The inset is the fluidic platform.

The OFI signal is acquired through the junction voltage of VCSELs. As in chapter 3, the signal is amplified using a customized trans-impedance amplifier and acquired using a National Instrument acquisition card (Ni USB 6251) at a sampling frequency of 400 kHz. Processing of the signal consists in 30 averagings of the Fast Fourier Transform (FFT) of 2^{15} samples length. All the data acquisition procedure and processing is automated by a custom-made LabVIEW program. Two VCSELs mounted in the same conditions on the PCB are tested: one with a microlens, one without (as a reference).

The OFI sensor signal spectra for different flow rate Q are computed. Averaged Doppler frequencies are extracted using the same weighted moment method[173], [174]. The results in different configurations are compared for the integrated sensor capability assessment.
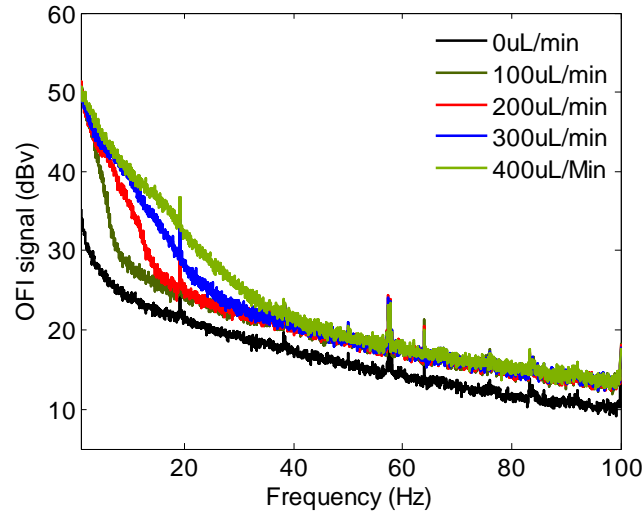
Fig.4.31. OFI signal spectra at different flow rates Q of the bare VCSEL and the 600 μm ×200 μm PDMS channel.

.
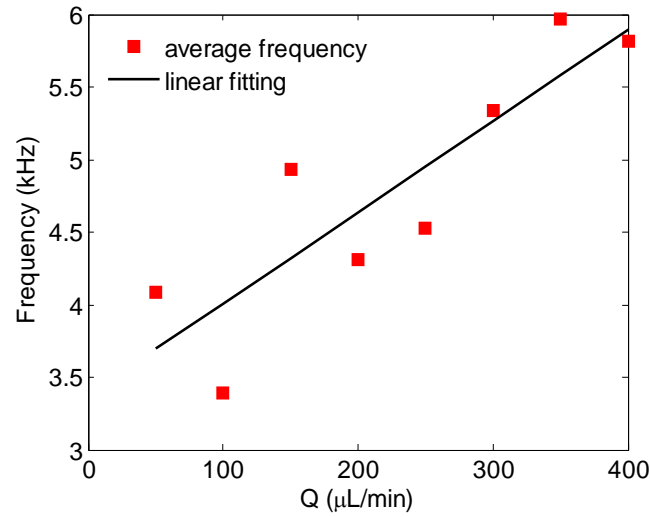
Fig.4.32. Average Doppler frequency extracted in weighted moment method against the flow rate Q with the bare VCSEL and the 600 μm ×200 μm PDMS channel.
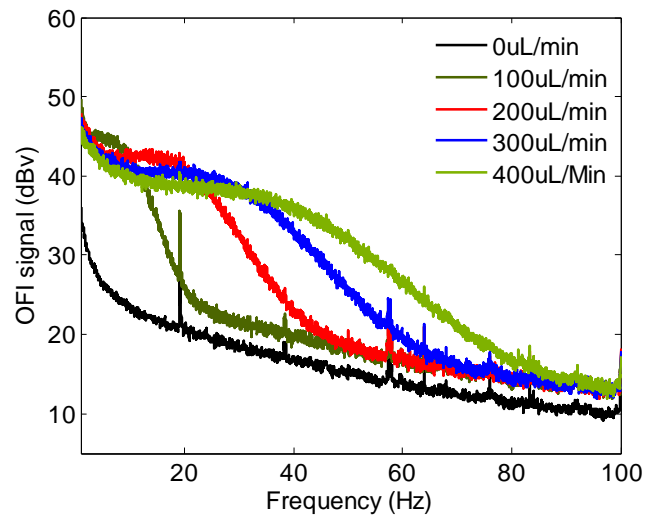
Fig.4.33. OFI signal spectra at different flow rates Q with the microlens integrated on VCSEL and the 600μm ×200μm PDMS channel.
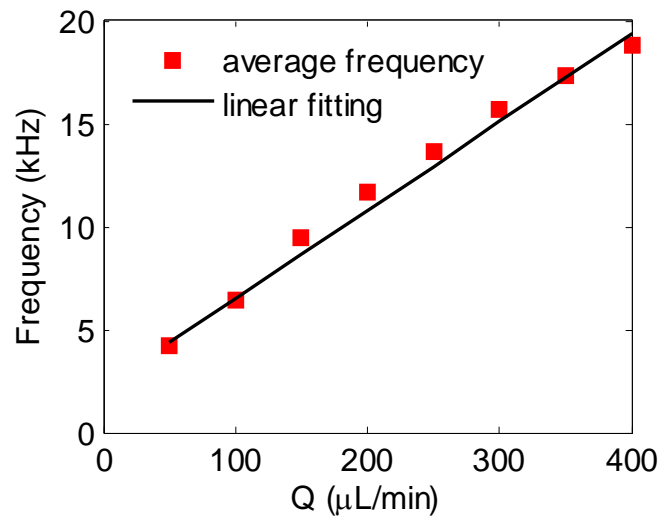
Fig.4.34. Average Doppler frequency extracted with weighted moment method versus the flow rate Q with the microlens integrated on VCSEL and the 600 μm ×200 μm PDMS channel.
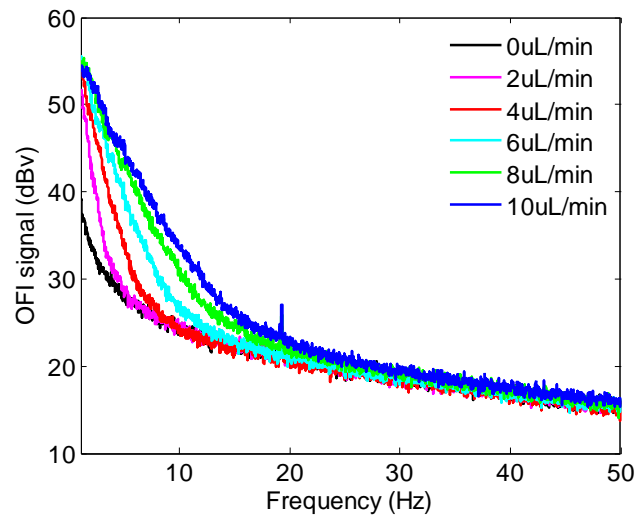
Fig.4.35. OFI signal spectra at different flow rates Q with the bare VCSEL anda192μm×48μm DF channel.
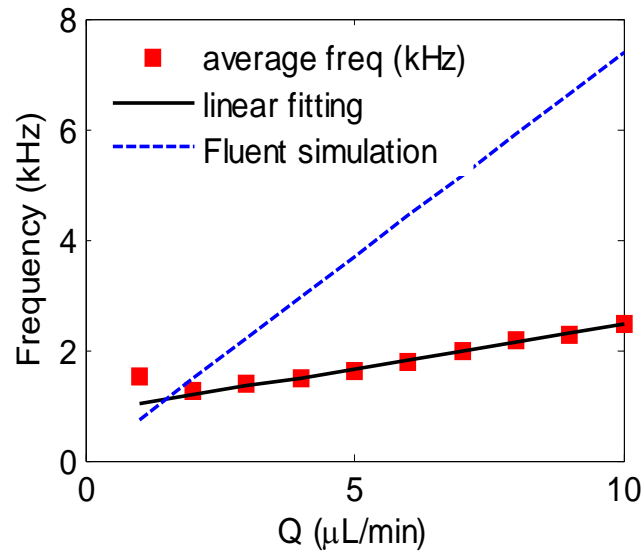
Fig.4.36. Average Doppler frequency extracted with the weighted moment method against flow rates Q with the bare VCSEL and a 192μm ×48μm DF channel.
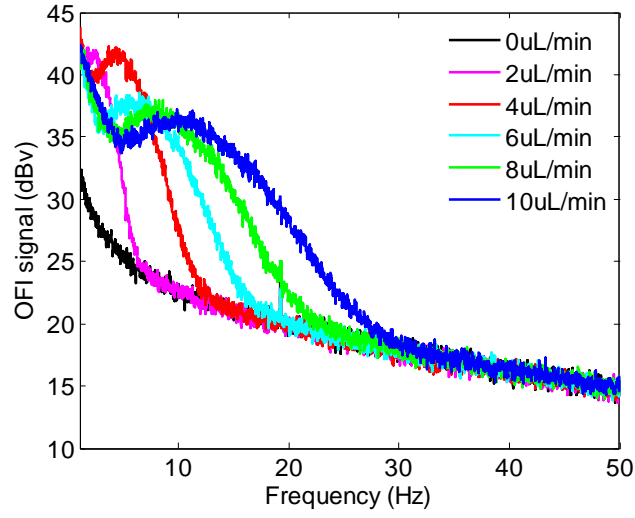
Fig.4.37. OFI signal spectra at different flow rates Q with the microlens integrated on the VCSEL and a 192μm ×48μm DF channel.
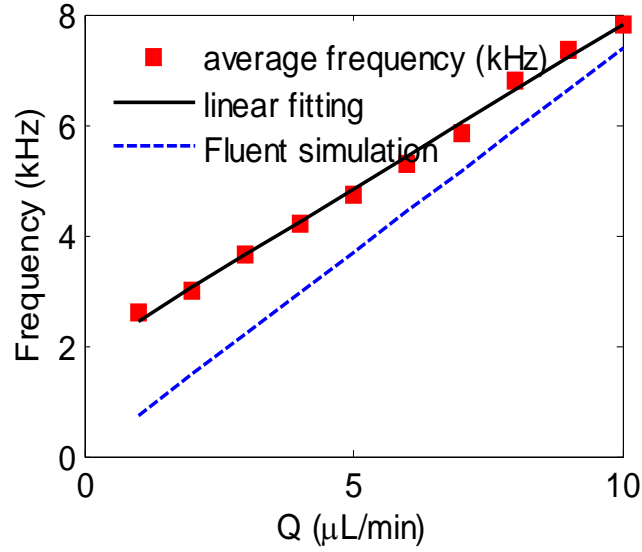
Fig.4.38. Average Doppler frequency extracted with the weighted moment method against the flow rate Q with the microlens integrated on the VCSEL and a192μm×48μm DF channel.

In Figs.4.31and 4.35 low amplitude signals are observed with the bare VCSEL system, this phenomenon can be attributed to the VCSEL natural divergence that induces a spreading of the light emission on a surface that is much bigger than the channel. Consequently, the weighted moment method cannot offer good linear trend against flow rate (Fig.4.32 and Fig.4.36).

On the contrary, the integrated OFI sensor with microlens presents an outstanding signal to noise ratio (SNR) level even in the micro-channel of cross-section dimension 192μm ×48μm.No less than 17 dB of visibility is observed for all the measurements in two different microchannels. The average Doppler frequency computed from the weighted moment method presents a good linearity versus the flow rate Q, which is in good agreement with the simulation results. Thus, a good sensing capability for flow rate or velocity evaluation in related application is to be expected with this system.

We applied the simulation method which has been presented in Chapter 2 to validate the simulation capability. Both spectra in lensed and bare VCSELs at Q=10μL/min were simulated. In case of bare lens, because the divergence angle is too big, insufficient incident rays hit the individual particles, so that the resulting scattered light power is too low to be received on the feedback detector surface.

Nevertheless, the simulated spectrum of lensed VCSEL assuming an incident angle of 10° is depicted in Fig.4.39, where there is a frequency peak at around 10kHz (red), which is quite close to the measurement result. However, the obtained shape is quite different from the measured one. This can be attributed to a lower power density and thus for each particle position very few rays are actually coming back into the laser cavity.
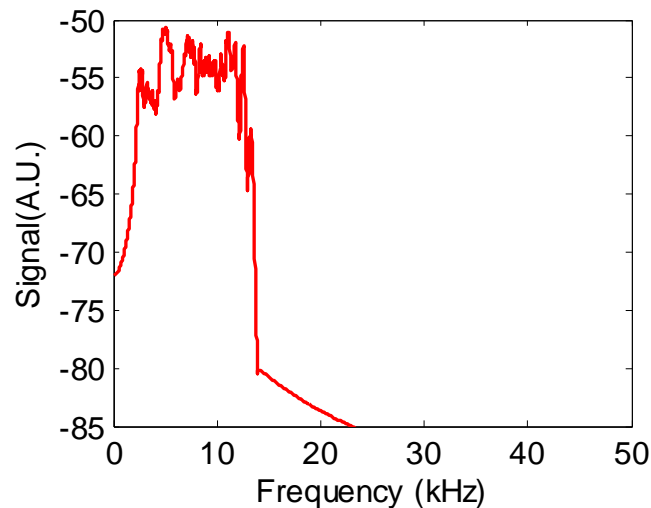
Fig.4.39. Simulated OFI spectrum at Q=10μL/min, the microlens integrated on the VCSEL and a 192μm×48μm DF channel.

4.5. Conclusions

We have designed a new integrated OFI sensor system based on micro-optical fabrication techniques, the fabrication procedure and measurement validations are presented in detail. The design based on Gaussian beam propagation and transform principles that were performed with ZEMAX merit function. In particular, the integrated microlens on the VCSEL collimating performance, i.e. the minimization of the far field divergence angle behind the microlens as well as the focusing lens optimization has been obtained by adjusting the lenses geometry.

Then the detailed fabrication procedure, including the DF pedestal integration, epoxy microlens printing and DF micro-channel realization is presented and discussed.

After optically and electrical characterization of the microlensed-VCSEL, flow measurements in two different microchannel dimensions are performed for system validation. Outstanding signal level and good Doppler frequency-flow rate linear trend prove that this system can satisfy the flowing sensing requirements even in the extremely tiny channel. We believe this system can be a potential tool in the design of future Lab-on-a-Chip devices requiring precise flow rate or fluid velocity monitoring.

Because of the limited time and tricky fabrication procedure, microscale focusing lens deposition on the channel has not been implemented yet. Further work will be done in both micro-fabrication and integrated OFI sensor experiments.

5 Conclusion and future prospects

The main objectives during the course of my Ph.D. studies were twofold: first, to model OFI sensors performance in microfluidic configuration, taking into account the structural complexity and particle characteristics. Second, to design and optimize a compact OFI flowmetry sensor based on micro-fabrication techniques.

5.1. Conclusion

In the first chapter, we reviewed the existing optical sensing techniques that measure flow rates and velocity field distribution in microchannels. A comparative study of the most established methods highlighted the potential of optical feedback interferometry (OFI) sensors in terms of costs, reliability, and compactness.

In the second chapter, we developed a novel comprehensive numerical methodology which enables precise reproduction and prediction of the OFI signal in microfluidic measurements. A new laser output power expression involving feedback perturbations from multiple scatterers was developed. Thanks to numerical simulation methods, optical propagation and fluid flow velocity distribution are evaluated. Then OFI signal was simulated via a dedicated MATLAB algorithm based on the laser rate equations under multiple feedbacks that merges the multi-simulation results. Moreover, the laser-particle interaction was investigated and the scattering behavior was evaluated using optical simulation tools to understand the OFI signal spectral broadening arising from the scattering angle dispersion. The impact of particle concentrations and sizes was analyzed so that the dependence of OFI signals upon these parameters further improves our model.

In Chapter 3, to validate the method depicted in Chapter 2, a series of measurements were performed using a commercial laser diode (VCSEL). The measurement results were compared with the simulation results to understand the OFI flowmetry sensor performance in different configurations. A good agreement with simulation results was found, successfully proving our numerical method capability.

In chapter 4, we designed a new integrated OFI sensor system based on micro-optical fabrication techniques. The objective was to avoid the use of bulk optics and to integrate two coupled polymer microlenses: a collimation one on the VCSEL chip and a focusing one on the microfluidic channel. The detailed fabrication procedure and tasks were presented and discussed. The Gaussian beam propagation in the integrated OFI sensor system was performed with ZEMAX software, by which we emphasized the optimization works including the minimization of the far field divergence angle of the VCSEL thanks to the microlens deposited on an epoxy pedestal. Finally, OFI measurements demonstrated a significant enhancement of signal level linked to the microlens on the VCSEL surface. This was successfully compared to modelling. Unfortunately, due to several technical issues, the production of a microfluidic chip with a deposited microlens on its surface was not achieved at the time of the manuscript writing and the results cannot be presented yet.

5.2. Summary of key findings

We developed a new comprehensive numerical model to describe the OFI flow sensor performance in a micro-scale channel based on multiple simulation software. To our knowledge, ZEMAX ray-tracing simulation was, for the first time, used in the special round-trip beam path of the feedback system. Our model is also the first work taking into account the influences of the particle scattering angle distribution and the fluidic system structure on the OFI signal. The simulation results were consistent with the measurements exhibiting the efficiency of the methodology.

In particular, we predicted that, under certain conditions in very small section channels, a second Doppler frequency appears in the OFI spectrum. This Doppler peak which has been experimentally validated was proven to be due to the contribution to the optical feedback of flowing particles passing in the vicinity of the rear interface of the microreactor where forward scattering light was reflected by this interface.

We successfully designed and implemented an integrated and robust VCSEL-based OFI flow sensor system which is directly mounted on a PCB with a small footprint (few mms). To this aim, we developed a new fabrication method based on thick resist film transfer and direct laser writing in order to integrate a collimation microlens on a

VCSEL chip at a post-mounting stage. Although the lens dimensions were not totally optimized and the focusing microlens was not yet integrated on the microfluidic part, more than 20dB of OFI signal level was constantly extracted all through the measurements in a microscale channel, much superior to the bare VCSEL case. In addition, a good Doppler frequency-flow rate linear trend proved that this OFI system can satisfy the flowing sensing accuracy requirements even in the extremely tiny channel.

5.3. Future works

Some further work could be interesting in the near further:

1. So far, our model only applies geometry optics theory to simulate the particle scattering performance, other well-known scattering theories such as Mie theory or Rayleigh theory could also be taken into account in our model.

2. Bi-concave ellipsoid modeling instead of the spherical particle could be of great interest to improve the simulation in the realistic case of red blood cell flowing in a capillary.

3. So far our model does only take into account the single scattering of light by particles. In the case of high concentration, a single photon will be scattered multiple times before traveling back to the laser. A further extension should be to implement an approach that would consider the multiple interactions of a single photon with particles before re-entering the laser cavity.

4. Because of technical limitations, at the date, we did not have enough time to deposit the micro-scale focusing lens on the channel surface using a localized surface treatment. This work is under progress and should lead rapidly to a further improvement of the compact OFI sensor performance. Optimization of lensed-VCSEL collimation is also undergoing.

References

[1] G. M. Whitesides, "The origins and the future of microfluidics.," *Nature*, vol. 442, no. 7101, pp. 368–73, 2006.

[2] P. Vennemann, R. Lindken, and J. Westerweel, "In vivo whole-field blood velocity measurement techniques," *Exp. Fluids*, vol. 42, no. 4, pp. 495–511, Mar. 2007.

[3] M. Draijer, E. Hondebrink, T. Van Leeuwen, and W. Steenbergen, "Review of laser speckle contrast techniques for visualizing tissue perfusion," *Lasers Med. Sci.*, vol. 24, no. 4, pp. 639–651, Jul. 2009.

[4] V. V. Tuchin, *Handbook of Coherent Domain Optical Methods: Biomedical Diagostics, Environment and Material Science*. Kluwer Academic Publishers, 2004.

[5] Z. Chen, T. E. Milner, D. Dave, and J. S. Nelson, "Optical Doppler tomographic imaging of fluid flow velocity in highly scattering media," *Opt. Lett.*, vol. 22, no. 1, p. 64, 1997.

[6] R. Lindken, M. Rossi, S. Große, and J. Westerweel, "Micro-Particle Image Velocimetry (µPIV): Recent developments, applications, and guidelines," *Lab Chip*, vol. 9, no. 17, p. 2551, Sep. 2009.

[7] J. G. Santiago, S. T. Wereley, C. D. Meinhart, D. J. Beebe, and R. J. Adrian, "A particle image velocimetry system for microfluidics," *Exp. Fluids*, vol. 25, no. 4, pp. 316–319, Sep. 1998.

[8] M. Baker and H. Wayland, "On-line volume flow rate and velocity profile measurement for blood in microvessels," *Microvasc. Res.*, vol. 7, no. 1, pp. 131–143, 1974.

[9] L. Büttner, J. Czarske, and H. Knuppertz, "Laser-Doppler velocity profile sensor with submicrometer spatial resolution that employs fiber optics and a diffractive lens.," *Appl. Opt.*, vol. 44, no. 12, pp. 2274–2280, 2005.

[10] U. Zabit, F. Bony, T. Bosch, and A. D. Rakic, "A self-mixing displacement sensor with fringe-loss compensation for harmonic vibrations," *IEEE Photonics Technol. Lett.*, vol. 22, no. 6, pp. 410–412, 2010.

[11] U. Zabit, O. D. Bernal, and T. Bosch, "A self-mixing displacement sensor compensating parasitic vibration with a MEMs accelerometer," *2011 IEEE SENSORS Proc.*, vol. 2, no. 2, pp. 1386–1389, Oct. 2011.

[12] A. Ashrif, A. Bakar, Y. L. Lim, S. J. Wilson, M. Fuentes, K. Bertling, T. Taimre, T. Bosch, and A. D. Raki, "On the feasibility of self-mixing interferometer sensing for detection of the surface electrocardiographic signal using a customized electro-optic phase modulator," *Physiol. Meas*, vol. 34, pp. 281–289, 2013.

[13] R. Michalzik and K. J. Ebeling, "Operating Principles of VCSELs," in *Vertical-Cavity Surface-Emitting Laser Devices*, Springer Berlin Heidelberg, 2003, pp. 53–98.

[14] A. Kazutaka, K. Otsuka, and J.-Y. Ko, "Self-mixing laser Doppler vibrometry with high optical sensitivity : application to real-time sound," *New J. Phys.*, vol. 5, p. 8.1-8.9, 2003.

[15]   S. Shinohara, A. Mochizuki, H. Yoshida, and M. Sumi, "Laser Doppler velocimeter using the self-mixing effect of a semiconductor laser diode," *Appl. Opt.*, vol. 25, no. 9, p. 1417, 1986.

[16]   U. Zabit, O. D. Bernal, T. Bosch, and F. Bony, "MEMS accelerometer embedded in a self-mixing displacement sensor for parasitic vibration compensation.," *Opt. Lett.*, vol. 36, no. 5, pp. 612–4, Mar. 2011.

[17]   G. Giuliani, S. Bozzi-Pietra, and S. Donati, "Self-mixing laser diode vibrometer," *Meas. Sci. Technol.*, vol. 14, no. 1, pp. 24–32, Jan. 2003.

[18]   M. Nikolić, Y. L. Lim, K. Bertling, T. Taimre, and A. D. Rakić, "Multiple signal classification for self-mixing flowmetry," *Appl. Opt.*, vol. 54, no. 9, pp. 2193–2198, 2015.

[19]   M. Nikolic, Y. Lim, and S. Wilson, "Flow profile measurement in micro-channels using changes in laser junction voltage due to Self-mixing effect," *IEEE sensors*, pp. 1394–1397, 2011.

[20]   M. Nikolić, D. P. Jovanović, Y. L. Lim, K. Bertling, T. Taimre, and A. D. Rakić, "Approach to frequency estimation in self-mixing interferometry: multiple signal classification," *Appl. Opt.*, vol. 52, no. 14, p. 3345, 2013.

[21]   L. Scalise, W. Steenbergen, and F. de Mul, "Self-mixing feedback in a laser diode for intra-arterial optical blood velocimetry.," *Appl. Opt.*, vol. 40, no. 25, pp. 4608–15, 2001.

[22]   Y. Yeh and H. Z. Cummins, "Localized fluid flow measurements with an HeNe laser spectrometer," *Appl. Phys. Lett.*, vol. 4, no. 10, pp. 176–178, 1964.

[23]   E. W. Washburn, "The Dynamics of Capillary Flow," *Phys. Rev.*, vol. 17, no. 3, pp. 273–283, Mar. 1921.

[24]   J. W. Foreman, R. D. Lewis, J. R. Thornton, and H. J. Watson, "Laser Doppler velocimeter for measurement of localized flow velocities in liquids," *Proc. IEEE*, vol. 54, no. 3, pp. 424–425, 1966.

[25]   E. R. Pike, D. A. Jackson, P. J. Bourke, and D. I. Page, "Measurement of turbulent velocities from the Doppler shift in scattered laser light," *J. Phys. E.*, vol. 1, no. 7, p. 306, Jul. 1968.

[26]   W. K. George and J. L. Lumley, "The laser-Doppler velocimeter and its applicaiton to the measurement of turbulence," *J. Fluid Mech.*, vol. 60, no. 2, pp. 321–362, 1973.

[27]   C. Riva, B. Ross, and G. B. Benedek, "Laser Doppler measurements of blood flow in capillary tubes and retinal arteries.," *Invest. Ophthalmol.*, vol. 11, no. 11, pp. 936–944, 1972.

[28]   J. B. Abbiss, "Principles and practice of laser-Doppler anemometry," *Opt. Laser Technol.*, vol. 8, no. 5, pp. 236–237, Oct. 1976.

[29]   J. König, A. Voigt, L. Büttner, and J. Czarske, "Precise micro flow rate measurements by a laser Doppler velocity profile sensor with time division multiplexing," *Meas. Sci. Technol.*, vol. 21, no. 7, p. 74005, 2010.

[30]   T. J. H. Essex and P. O. Byrne, "A laser Doppler scanner for imaging blood flow in skin," *J. Biomed. Eng.*, vol. 13, no. 3, pp. 189–194, May 1991.

[31]   G. Michelson, M. Groh, M. Langhans, and B. Schmauss, "2-dimensional mapping and retinal and papillary microcirculation using scanning laser Doppler flowmetry," *Klin. Monbl. Augenheilkd.*, vol. 207, no. 3, pp. 180–90, Sep. 1995.

[32]   S. A. Pape, C. A. Skouras, and P. O. Byrne, "An audit of the use of laser Doppler imaging (LDI) in the assessment of burns of intermediate depth," *Burns*, vol. 27, no. 3, pp. 233–239, May 2001.

[33]   A. Fischer, U. Wilke, R. Schlüßler, D. Haufe, T. Sandner, and J. Czarske, "Extension of frequency modulated Doppler global velocimetry for the investigation of unsteady spray flows," *Opt. Lasers Eng.*, vol. 63, pp. 1–10, Dec. 2014.

[34]   D. R. Cadel and K. T. Lowe, "Cross-correlation Doppler global velocimetry (CC-DGV)," *Opt. Lasers Eng.*, vol. 71, pp. 51–61, Aug. 2015.

[35]   D. Huang, E. A. Swanson, C. P. Lin, J. S. Schuman, W. G. Stinson, W. Chang, M. R. Hee, T. Flotte, K. Gregory, C. A. Puliafito, and J. G. Fujimoto, "Optical coherence tomography.," *Science*, vol. 254, no. 5035, pp. 1178–81, Nov. 1991.

[36]   A. M. Rollins, S. Yazdanfar, J. K. Barton, and J. a Izatt, "Real-time in vivo color Doppler optical coherence tomography.," *J. Biomed. Opt.*, vol. 7, no. 1, pp. 123–129, 2002.

[37]   B. Cense, N. Nassif, T. Chen, M. Pierce, and S. Yun, "Ultrahigh-resolution high-speed retinal imaging using spectral-domain optical coherence tomography," *Opt. Express*, vol. 12, no. 11, pp. 2435–2447, 2004.

[38]   R. J. Adrian, "Twenty years of particle image velocimetry," *Exp. Fluids*, vol. 39, no. 2, pp. 159–169, Jul. 2005.

[39]   F. Sarrazin, K. Loubière, L. Prat, C. Gourdon, T. Bonometti, and J. Magnaudet, "Experimental and numerical study of droplets hydrodynamics in MicroChannel," *AIChE J.*, vol. 52, no. 12, pp. 4061–4070, Dec. 2006.

[40]   A. K. Prasad, "Particle Image Velocimetry," *Curr. Sci.*, vol. 1, pp. 51–60, 2000.

[41]   M. Riethmuller, L. David, and B. Lecordier, "Particle Image Velocimetry," in *Laser Velocimetry in Fluid Mechanics*, Hoboken, NJ, USA: John Wiley & Sons, Inc., 2012, pp. 159–281.

[42]   D. B. Barker and M. E. Fourney, "Measuring fluid velocities with speckle patterns," *Opt. Lett.*, vol. 1, no. 4, p. 135, Oct. 1977.

[43]   T. D. Dudderar and P. G. Simpkins, "Laser speckle photography in a fluid medium," *Nature*, vol. 270, no. 5632, pp. 45–47, Nov. 1977.

[44]   R. Grousson and S. Mallick, "Study of flow pattern in a fluid by scattered laser light," *Appl. Opt.*, vol. 16, no. 9, p. 2334, Sep. 1977.

[45]   R. Meynart, "Convective flow field measurement by speckle velocimetry," *Rev. Phys. Appliquée*, vol. 17, no. 5, pp. 301–305, May 1982.

[46]   R. Meynart, "Equal velocity fringes in a Rayleigh-Benard flow by a speckle method," *Appl. Opt.*, vol. 19, no. 9, p. 1385, May 1980.

[47]   R. Meynart, "Speckle velocimetry study of vortex pairing in a low-Re unexcited jet," *Phys. Fluids*, vol. 26, no. 8, p. 2074, 1983.

[48]   R. Meynart, "Equal velocity fringes in a Rayleigh-Benard flow by a speckle method," *Appl. Opt.*, vol. 19, no. 9, p. 1385, May 1980.

[49]   R. J. Adrian, "Scattering particle characteristics and their effect on pulsed laser measurements of fluid flow: speckle velocimetry vs particle image velocimetry," *Appl. Opt.*, vol. 23, no. 11, p. 1690, Jun. 1984.

[50]   R. Lindken, J. Westerweel, and B. Wieneke, "Stereoscopic micro particle image velocimetry," *Exp. Fluids*, vol. 41, no. 2, pp. 161–171, Aug. 2006.

[51]   S. T. Wereley and C. D. Meinhart, "Micron-Resolution Particle Image Velocimetry," in *Microscale Diagnostic Techniques*, Berlin/Heidelberg: Springer-Verlag, 2005, pp. 51–112.

[52]   S. W. Stone, C. D. Meinhart, and S. T. Wereley, *A microfluidic-based nanoscope*, vol. 33, no. 5. Springer-Verlag, 2002.

[53]   C. L. Asbury, A. H. Diercks, and G. van den Engh, "Trapping of DNA by dielectrophoresis," *Electrophoresis*, vol. 23, no. 16, pp. 2658–2666, Aug. 2002.

[54]   S. Yao and J. G. Santiago, "Porous glass electroosmotic pumps: theory," *J. Colloid Interface Sci.*, vol. 268, pp. 133–142, 2003.

[55]   A. Günther and K. F. Jensen, "Multiphase microfluidics: from flow characteristics to chemical and materials synthesis.," *Lab Chip*, vol. 6, no. 12, pp. 1487–503, Dec. 2006.

[56]   B. J. Kim, Y. Z. Liu, and H. J. Sung, "Micro PIV measurement of two-fluid flow with different refractive indices," *Meas. Sci. Technol.*, vol. 15, no. 6, pp. 1097–1103, Jun. 2004.

[57]   A. Günther, S. A. Khan, M. Thalmann, F. Trachsel, and K. F. Jensen, "Transport and reaction in microscale segmented gas-liquid flow.," *Lab Chip*, vol. 4, no. 4, pp. 278–286, Jul. 2004.

[58]   Y. Sugii, S. Nishio, and K. Okamoto, "In vivo PIV measurement of red blood cell velocity field in microvessels considering mesentery motion," *Physiol. Meas.*, vol. 23, no. 2, pp. 403–416, May 2002.

[59]   J. R. Hove, R. W. Köster, A. S. Forouhar, G. Acevedo-Bolton, S. E. Fraser, and M. Gharib, "Intracardiac fluid forces are an essential epigenetic factor for embryonic cardiogenesis," *Nature*, vol. 421, no. 6919, pp. 172–177, Jan. 2003.

[60]   J. H. Jeong, Y. Sugii, M. Minamiyama, H. Takeuchi, and K. Okamoto, "Interaction between liposomes and RBC in microvessels in vivo," *Microvasc. Res.*, vol. 73, no. 1, pp. 39–47, Jan. 2007.

[61]   P. K. WONG, Y.-K. LEE, and C.-M. HO, "Deformation of DNA molecules by hydrodynamic focusing," *J. Fluid Mech.*, vol. 497, pp. 55–65, Dec. 2003.

[62] J. Leyton-Mange, S. Yang, M. H. Hoskins, R. F. Kunz, J. D. Zahn, and C. Dong, "Design of a Side-View Particle Imaging Velocimetry Flow System for Cell-Substrate Adhesion Studies," *J. Biomech. Eng.*, vol. 128, no. 2, p. 271, Apr. 2006.

[63] B. J. Gemmell, H. Jiang, and E. J. Buskey, "A new approach to micro-scale particle image velocimetry (μPIV) for quantifying flows around free-swimming zooplankton," *J. Plankton Res.*, vol. 36, no. 5, pp. 1396–1401, Sep. 2014.

[64] T. H. Maiman, "Stimulated Optical Radiation in Ruby," *Nature*, vol. 187, no. 4736, pp. 493–494, Aug. 1960.

[65] D. A. Kleinman and P. P. Kisliuk, "Discrimination Against Unwanted Orders in the Fabry-Perot Resonator," *Bell Syst. Tech. J.*, vol. 41, no. 2, pp. 453–462, Mar. 1962.

[66] J. S. Graham and R. K. P. George, "Apparatus for measurement of lengths and of other physical parameters which are capable of altering an optical path length," 1968.

[67] X. Dai, M. Wang, Y. Zhao, and J. Zhou, "Self-mixing interference in fiber ring laser and its application for vibration measurement," *Opt. Express*, vol. 17, no. 19, p. 16543, Sep. 2009.

[68] H. Lee, "Spectral Characteristics of Vertical-Cavity Surface-Emitting Lasers with External Optical Feedback," *IEEE Photonics Technol. Lett.*, vol. 3, no. 7, pp. 597–599, 1991.

[69] S. Blaize, B. Bérenguier, I. Stéfanon, A. Bruyant, G. Lérondel, P. Royer, O. Hugon, O. Jacquin, and E. Lacot, "Phase sensitive optical near-field mapping using frequency-shifted laser optical feedback interferometry," *Opt. Express*, vol. 16, no. 16, p. 11718, Aug. 2008.

[70] S. Okamoto, H. Takeda, and F. Kannari, "Ultrahighly sensitive laser-Doppler velocity meter with a diode-pumped Nd:YVO$_4$ microchip laser," *Rev. Sci. Instrum.*, vol. 66, no. 5, pp. 3116–3120, May 1995.

[71] R. P. Green, J.-H. Xu, L. Mahler, A. Tredicucci, F. Beltram, G. Giuliani, H. E. Beere, and D. A. Ritchie, "Linewidth enhancement factor of terahertz quantum cascade lasers," *Appl. Phys. Lett.*, vol. 92, no. 7, p. 71106, Feb. 2008.

[72] Y. Mitsuhashi, J. Shimada, and S. Mitsutsuka, "Voltage change across the self-coupled semiconductor laser," *IEEE J. Quantum Electron.*, vol. 17, no. 7, pp. 1216–1225, 1981.

[73] L. Scalise, Y. Yu, G. Giuliani, G. Plantier, and T. Bosch, "Self-mixing laser diode velocimetry: Application to vibration and velocity measurement," *IEEE Trans. Instrum. Meas.*, vol. 53, no. 1, pp. 223–232, 2004.

[74] T. Bosch, I. C. Bes, L. Scalise, and G. Plantier, "Optical Feedback Interferometry," in *Encyclopedia of Sensors*, American Scientific Publishers, 2006, pp. 1–20.

[75] S. Donati, "Developing self-mixing interferometry for instrumentation and measurements," *Laser Photonics Rev.*, vol. 6, no. 3, pp. 393–417, 2012.

[76] S. Ma, F. Xie, L. Chen, Y. Z. Wang, L. L. Dong, and K. Q. Zhao, "Development of dual-wavelength fiber ring laser and its application to step-height measurement using self-mixing interferometry," *Opt. Express*, vol. 24, no. 6, p. 5693, 2016.

[77] P. Dean, J. T. Keeley, A. Valavanis, K. Bertling, Y. L. Lim, T. Taimre, R. H. S. Alhathlool, L. H. Li, D. Indjin, A. D. Rakić, E. H. Linfield, and A. G. Davies, "Active phase-nulling of the self-mixing phase in a terahertz frequency quantum cascade laser," *Opt. Lett.*, vol. 40, no. 6, p. 950, 2015.

[78] R. Kliese, Y. L. Lim, K. Bertling, A. A. A. Bakar, T. Bosch, and A. D. Rakic, "Self-mixing displacement sensing using the junction voltage variation in a GaN laser," in *2008 Conference on Optoelectronic and Microelectronic Materials and Devices*, 2008, pp. 23–25.

[79] M. T. Fathi and S. Donati, "Thickness measurement of transparent plates by a self-mixing interferometer," *Opt. Lett.*, vol. 35, no. 11, pp. 1844–6, 2010.

[80] Y. Gao, Y. Yu, J. Xi, Q. Guo, J. Tong, and S. Tong, "Improved method for estimation of multiple parameters in self-mixing interferometry," *Appl. Opt.*, vol. 54, no. 10, p. 2703, 2015.

[81] F. F. M. de Mul, M. H. Koelink, A. L. Weijers, J. Greve, J. G. Aarnoudse, R. Graaff, and A. C. M. Dassel, "A semiconductor laser used for direct measurement of the blood perfusion of tissue," *IEEE Transactions on Biomedical Engineering*, vol. 40, no. 2. pp. 208–210, 1993.

[82] L. Rovati, S. Cattini, and N. Palanisamy, "Measurement of the fluid-velocity profile using a self-mixing superluminescent diode," *Meas. Sci. Technol.*, vol. 22, no. 2, p. 25402, Feb. 2011.

[83] L. Campagnolo, M. Nikolić, J. Perchoux, Y. L. Lim, K. Bertling, K. Loubière, L. Prat, A. D. Rakić, and T. Bosch, "Flow profile measurement in microchannel using the optical feedback interferometry sensing technique," *Microfluid. Nanofluidics*, vol. 14, no. 1–2, pp. 113–119, Jul. 2013.

[84] Y. L. Lim, R. Kliese, K. Bertling, K. Tanimizu, P. A. Jacobs, and A. D. Rakić, "Self-mixing flow sensor using a monolithic VCSEL array with parallel readout," *Opt. Express*, vol. 18, no. 11, pp. 11720–7, May 2010.

[85] E. E. Ramrez-Miquet, J. Perchoux, K. Loubière, C. Tronche, L. Prat, and O. Sotolongo-Costa, "Optical feedback interferometry for velocity measurement of parallel liquid-liquid flows in a microchannel," *Sensors*, vol. 16, no. 8, 2016.

[86] R. Kliese, Y. Lim, T. Bosch, and A. Rakić, "GaN laser self-mixing velocimeter for measuring slow flows," *Opt. Lett.*, vol. 35, no. 6, pp. 814–816, 2010.

[87] V. Contreras, J. Lönnqvist, and J. Toivonen, "Detection of single microparticles in airflows by edge-filter enhanced self-mixing interferometry," *Opt. Express*, vol. 24, no. 8, p. 8886, 2016.

[88] S. K. Ozdemir, S. Shinohara, S. Takamiya, and H. Yoshida, "Noninvasive blood flow measurement using speckle signals from a self-mixing laser diode: in vitro and in vivo experiments," *Opt. Eng.*, vol. 39, no. 9, p. 2574, Sep. 2000.

[89] S. K. Ozdemir, S. Takamiya, S. Ito, S. Shinohara, and H. Yoshida, "Self-mixing laser speckle velocimeter for blood flow measurement," *IEEE Trans. Instrum. Meas.*, vol. 49, no. 5, pp. 1029–1035, 2000.

[90]   S. K. Ozdemir, I. Ohno, and S. Shinohara, "A Comparative Study for the Assessment on Blood Flow Measurement Using Self-Mixing Laser Speckle Interferometer," *IEEE Trans. Instrum. Meas.*, vol. 57, no. 2, pp. 355–363, 2008.

[91]   F. F. M. de Mul, L. Scalise, A. L. Petoukhova, M. van Herwijnen, P. Moes, and W. Steenbergen, "Glass-fiber self-mixing intra-arterial laser Doppler velocimetry: signal stability and feedback analysis," *Appl. Opt.*, vol. 41, no. 4, pp. 658–67, 2002.

[92]   M. Norgia, A. Pesatori, and L. Rovati, "Self-mixing laser doppler spectra of extracorporeal blood flow: A theoretical and experimental study," *IEEE Sens. J.*, vol. 12, no. 3, pp. 552–557, 2012.

[93]   E. Figueiras, R. Oliveira, C. F. Lourenco, R. Campos, A. Humeau-Heurtier, R. M. Barbosa, J. Laranjinha, L. F. Requicha Ferreira, and F. F. M. De Mul, "Self-mixing microprobe for monitoring microvascular perfusion in rat brain," *Med. Biol. Eng. Comput.*, vol. 51, no. 1–2, pp. 103–112, 2013.

[94]   A. Quotb, E. E. Ramirez-Miquet, C. Tronche, and J. Perchoux, "Optical Feedback Interferometry sensor for flow characterization inside ex-vivo vessel," in *IEEE SENSORS 2014 Proceedings*, 2014, pp. 362–365.

[95]   A. Mowla, T. Taimre, Y. L. Lim, K. Bertling, S. J. Wilson, T. W. Prow, H. P. Soyer, and A. D. Rakić, "Concurrent Reflectance Confocal Microscopy and Laser Doppler Flowmetry to Improve Skin Cancer Imaging: A Monte Carlo Model and Experimental Validation," *Sensors*, vol. 16, no. 9, p. 1411, 2016.

[96]   M. Norgia, A. Pesatori, and L. Rovati, "Self-mixing laser Doppler: a model for extracorporeal blood flow measurement," *IEEE*, no. 1, 2010.

[97]   H. W. Jentink, F. F. de Mul, H. E. Suichies, J. G. Aarnoudse, and J. Greve, "Small laser Doppler velocimeter based on the self-mixing effect in a diode laser.," *Appl. Opt.*, vol. 27, no. 2, pp. 379–85, 1988.

[98]   R. Lang and K. Kobayashi, "External optical feedback effects on semiconductor injection laser properties," *IEEE J. Quantum Electron.*, vol. 16, no. 3, pp. 347–355, 1980.

[99]   W. M. Wang, W. J. O. Boyle, K. T. V. Grattan, and A. W. Palmer, "Self-mixing interference in a diode laser: experimental observations and theoretical analysis," *Appl. Opt.*, vol. 32, no. 9, p. 1551, Mar. 1993.

[100]   G. Plantier, C. Bes, and T. Bosch, "Behavioral model of a self-mixing laser diode sensor," *IEEE J. Quantum Electron.*, vol. 41, no. 9, pp. 1157–1167, Sep. 2005.

[101]   K. Petermann, *Laser Diode Modulation and Noise*. Springer Netherlands, 1988.

[102]   P. J. de Groot, G. M. Gallatin, and S. H. Macomber, "Ranging and velocimetry signal generation in a backscatter-modulated laser diode," *Appl. Opt.*, vol. 27, no. 21, pp. 4475–4480, Nov. 1988.

[103]   G. Liu, S. Zhang, J. Zhu, and Y. Li, "Theoretical and experimental study of intensity branch phenomena in self-mixing interference in a He–Ne laser," *Opt. Commun.*, vol. 221, no. 4–6, pp. 387–393, Jun. 2003.

[104] A. Larsson, "Advances in VCSELs for Communication and Sensing," *IEEE J. Sel. Top. Quantum Electron.*, vol. 17, no. 6, pp. 1552–1567, Nov. 2011.

[105] A. Pruijmboom, M. Schemmann, J. Hellmig, J. Schutte, H. Moench, and J. Pankert, "VCSEL-based miniature laser-Doppler interferometer," in *Proc. SPIE 6908, Vertical-Cavity Surface-Emitting Lasers XII*, 2008, vol. 6908, no. 1, p. 69080I–69080I–7.

[106] A. Pruijmboom, S. Booij, M. Schemmann, K. Werner, P. Hoeven, H. van Limpt, S. Intemann, R. Jordan, T. Fritzsch, H. Oppermann, and M. Barge, "VCSEL-based miniature laser-self-mixig interferometer with integrated optical and electronic components," *Proc. SPIE*, vol. 7221, p. 72210S–72210S–12, Feb. 2009.

[107] A. Kroner, I. Kardosh, F. Rinaldi, and R. Michalzik, "Towards VCSEL-based integrated optical traps for biomedical applications," *Electron. Lett.*, vol. 42, no. 2, p. 93, 2006.

[108] D. Heinis, C. Gorecki, C. Bringer, V. Bardinal, T. Camps, J.-B. Doucet, P. Dubreuil, and C. Fontaine, "Miniaturized Scanning Near-Field Microscope Sensor Based on Optical Feedback Inside a Single-Mode Oxide-Confined Vertical-Cavity Surface-Emitting Laser," *Jpn. J. Appl. Phys.*, vol. 42, no. Part 2, No. 12A, pp. L1469–L1471, Dec. 2003.

[109] L. M. Lechuga, J. Tamayo, M. Álvarez, L. G. Carrascosa, A. Yufera, R. Doldán, E. Peralías, A. Rueda, J. A. Plaza, K. Zinoviev, C. Domínguez, A. Zaballos, M. Moreno, C. Martínez-A, D. Wenn, N. Harris, C. Bringer, V. Bardinal, T. Camps, C. Vergnenègre, C. Fontaine, V. Díaz, and A. Bernad, "A highly sensitive microsystem based on nanomechanical biosensors for genomics applications," *Sensors Actuators, B Chem.*, vol. 118, no. 1–2, pp. 2–10, 2006.

[110] E. Thrush, O. Levi, W. Ha, G. Carey, L. J. Cook, J. Deich, S. J. Smith, W. E. Moerner, and J. S. Harris, "Integrated semiconductor vertical-cavity surface-emitting lasers and PIN photodetectors for biomedical fluorescence sensing," *IEEE J. Quantum Electron.*, vol. 40, no. 5, pp. 491–498, May 2004.

[111] Y. Lim, M. Nikolic, K. Bertling, R. Kliese, and A. Rakic, "Self-mixing imaging sensor using a monolithic VCSEL array with parallel readout," *Opt. Express*, vol. 17, no. 7, pp. 5517–5525, 2009.

[112] R. S. Matharu, J. Perchoux, R. Kliese, Y. L. Lim, and A. D. Rakić, "Maintaining maximum signal-to-noise ratio in uncooled vertical-cavity surface-emitting laser-based self-mixing sensors.," *Opt. Lett.*, vol. 36, no. 18, pp. 3690–2, Sep. 2011.

[113] J. Albert, M. C. Soriano, I. Veretennicoff, K. Panajotov, J. Danckaert, P. a. Porta, D. P. Curtin, and J. G. McInerney, "Laser doppler velocimetry with polarization-bistable VCSELs," *IEEE J. Sel. Top. Quantum Electron.*, vol. 10, no. 5, pp. 1006–1012, 2004.

[114] L. Campagnolo, S. Roman, and J. Perchoux, "A new optical feedback interferometer for measuring red blood cell velocity distributions in individual capillaries : a feasibility study in microchannels," *Comput. Methods Biomech. Biomed. Engin.*, vol. 15, no. S1, pp. 104–105, 2012.

[115] J. Perchoux and T. Bosch, "Multimode VCSELs for Self-Mixing Velocity Measurements," *2007 IEEE Sensors*, no. 3, pp. 419–422, 2007.

[116] M. Grabherr, P. Gerlach, R. King, and R. Jager, "Integrated photodiodes complement the

VCSEL platform," *Proc. SPIE*, vol. 7229, p. 72290E–72290E–9, Feb. 2009.

[117]   W. M. Wang, K. T. V Grattan, A. W. Palmer, and W. J. O. Boyle, "Self-mixing interference inside a single-mode diode laser for optical sensing applications," *J. Light. Technol.*, vol. 12, no. 9, pp. 1577–1587, 1994.

[118]   T. Taimre, M. Nikolić, K. Bertling, Y. L. Lim, T. Bosch, and A. D. Rakić, "Laser feedback interferometry: a tutorial on the self-mixing effect for coherent sensing," *Adv. Opt. Photonics*, vol. 7, no. 3, p. 570, Sep. 2015.

[119]   C. H. Henry, "Theory of the linewidth of semiconductor lasers," *Quantum Electron. IEEE J.*, vol. 18, no. 2, pp. 259–264, 1982.

[120]   M. Slot, M. H. Koelink, F. G. Scholten, F. F. M. de Mul, A. L. Weijers, J. Greve, R. Graaff, A. C. M. Dassel, J. G. Aarnoudse, and F. H. B. Tuynman, "Blood flow velocity measurements based on the self-mixing effect in a fibre-coupled semiconductor laser:in vivo and in vitro measurements," *Med. Biol. Eng. Comput.*, vol. 30, no. 4, pp. 441–446, 1992.

[121]   L. A. Coldren and S. W. Corzine, "Diode Lasers and Photonic Integrated Circuits," *Opt. Eng.*, vol. 36, no. 2, p. 616, Feb. 1997.

[122]   Y. L. Lim, J. R. Tucker, and A. D. Rakic, "Distance measurement using the change in junction voltage across a laser diode due to the self-mixing effect," *2006 North. Opt. Conf. Proc.*, vol. 6038, pp. 73–77, 2006.

[123]   A. A. A. Bakar, J. Z. V Flores, Y. L. Lim, R. Kliese, and A. D. Rakić, "Self-Mixing Interferometer technique based on VCSEL under the effect of polarization mode switching," *2010 Int. Conf. Photonics, ICP2010*, pp. 0–3, 2010.

[124]   A. Quirantes, F. Arroyo, and J. Quirantes-Ros, "Multiple Light Scattering by Spherical Particle Systems and Its Dependence on Concentration: A T-Matrix Study," *J. Colloid Interface Sci.*, vol. 240, no. 1, pp. 78–82, Aug. 2001.

[125]   M. I. Mishchenko, J. W. Hovenier, and D. W. Mackowski, "Single scattering by a small volume element," *J. Opt. Soc. Am. A*, vol. 21, no. 1, p. 71, Jan. 2004.

[126]   H. Zhao, "Optical ensemble analysis of intraocular lens performance through a simulated clinical trial with ZEMAX.," *Opt. Lett.*, vol. 34, no. 1, pp. 7–9, 2009.

[127]   X. Lee and C. Wang, "Optical design for uniform scanning in MEMS-based 3D imaging lidar," *Appl. Opt.*, vol. 54, no. 9, pp. 2219–2223, 2015.

[128]   P. Abgrall, V. Conedera, H. Camon, A.-M. Gue, and N.-T. Nguyen, "SU-8 as a structural material for labs-on-chips and microelectromechanical systems," *Electrophoresis*, vol. 28, no. 24, pp. 4539–4551, Dec. 2007.

[129]   M. Spiga and G. L. Morino, "A symmetric solution for velocity profile in laminar flow through rectangular ducts," *Int. Commun. Heat Mass Transf.*, vol. 21, no. 4, pp. 469–475, 1994.

[130]   M. Born, *Principles of Optics.* Elsevier Science, 1980.

[131] F. Xu, K. F. Ren, X. Cai, and J. Shen, "Extension of geometrical-optics approximation to on-axis Gaussian beam scattering. II. By a spheroidal particle with end-on incidence.," *Appl. Opt.*, vol. 45, no. 20, pp. 5000–9, 2006.

[132] M. Norgia, A. Pesatori, and L. Rovati, "Low-cost optical flowmeter with analog front-end electronics for blood extracorporeal circulators," *IEEE Trans. Instrum. Meas.*, vol. 59, no. 5, pp. 1233–1239, 2010.

[133] E. Hecht and Eugene, *Optics 4th Edition*. Addison Wesley Longman Inc, 1998.

[134] P. A. Porta, D. P. Curtin, and J. G. McInerney, "Laser Doppler velocimetry by optical self-mixing in vertical-cavity surface-emitting lasers," *IEEE Photonics Technol. Lett.*, vol. 14, no. 12, pp. 1719–1721, Dec. 2002.

[135] J. Al Roumy, J. Perchoux, Y. L. Lim, T. Taimre, A. D. Rakić, and T. Bosch, "Effect of injection current and temperature on signal strength in a laser diode optical feedback interferometer," *Appl. Opt.*, vol. 54, no. 2, p. 312, Jan. 2015.

[136] S. V Sankar, B. J. Weber, D. Y. Kamemoto, and W. D. Bachalo, "Sizing fine particles with the phase Doppler interferometric technique.," *Appl. Opt.*, vol. 30, no. 33, pp. 4914–20, 1991.

[137] S. V Sankar and W. D. Bachalo, "Response characteristics of the phase Doppler particle analyzer for sizing spherical particles larger than the light wavelength.," *Appl. Opt.*, vol. 30, no. 12, pp. 1487–96, 1991.

[138] W. M. Farmer, "Measurement of particle size, number density, and velocity using a laser interferometer.," *Appl. Opt.*, vol. 11, no. 11, pp. 2603–12, 1972.

[139] C. Zakian, M. Dickinson, and T. King, "Particle sizing and flow measurement using self-mixing interferometry with a laser diode," *J. Opt. A Pure Appl. Opt.*, vol. 7, no. 6, pp. S445–S452, 2005.

[140] H. Wang and J. Shen, "Fast and economic signal processing technique of laser diode self-mixing interferometry for nanoparticle size measurement," *Appl. Phys. B Lasers Opt.*, vol. 115, no. 2, pp. 285–291, 2014.

[141] L. Campagnolo, "Optical feedback interferometry sensing technique for flow measurements in microchannels," Institut National Polytechnique de Toulouse - INPT, 2013.

[142] Y. Zhao, J. Perchoux, L. Campagnolo, T. Camps, R. Atashkhooei, and V. Bardinal, "Optical feedback interferometry for microscale-flow sensing study: numerical simulation and experimental validation," *Opt. Express*, vol. 24, no. 21, p. 23849, Oct. 2016.

[143] Z. D. Popovic, R. A. Sprague, and G. A. N. Connell, "Technique for monolithic fabrication of microlens arrays.," *Appl. Opt.*, vol. 27, no. 7, pp. 1281–1284, Apr. 1988.

[144] H. Ottevaere, B. Volckaerts, J. Lamprecht, J. Schwider, A. Hermanne, I. Veretennicoff, and H. Thienpont, "Two-dimensional plastic microlens arrays by deep lithography with protons: fabrication and characterization," *J. Opt. A Pure Appl. Opt.*, vol. 4, no. 4, p. 354, Jul. 2002.

[145] P. Ruther, B. Gerlach, J. Göttert, M. Ilie, J. Mohr, A. Müller, and C. Oßmann, "Fabrication and characterization of microlenses realized by a modified LIGA process," *Pure Appl. Opt. J. Eur. Opt. Soc. Part A*, vol. 6, no. 6, pp. 643–653, Nov. 1999.

[146] C. Croutxé-Barghorn, O. Soppera, and D. J. Lougnot, "Fabrication of microlenses by direct photo-induced crosslinking polymerization," *Appl. Surf. Sci.*, vol. 168, no. 1–4, pp. 89–91, Dec. 2000.

[147] C. H. Tien, C. H. Hung, and T. H. Yu, "Microlens arrays by direct-writing inkjet print for LCD backlighting applications," *IEEE/OSA J. Disp. Technol.*, vol. 5, no. 5, pp. 147–151, 2009.

[148] W.-C. Chen, T.-J. Wu, W.-J. Wu, and G.-D. J. Su, "Fabrication of inkjet-printed SU-8 photoresist microlenses using hydrophilic confinement," *J. Micromechanics Microengineering*, vol. 23, no. 6, p. 65008, 2013.

[149] J. Y. Kim, N. B. Brauer, V. Fakhfouri, D. L. Boiko, E. Charbon, G. Grutzner, and J. Brugger, "Hybrid polymer microlens arrays with high numerical apertures fabricated using simple ink-jet printing technique," *Opt. Mater. Express*, vol. 1, no. 2, p. 259, 2011.

[150] S. Biehl, R. Danzebrink, P. Oliveira, and M. a Aegerter, "Refractive Microlens Fabrication by Ink-Jet Process," *J. Sol-Gel Sci. Technol.*, vol. 182, pp. 177–182, 1998.

[151] D. J. Hayes, M. E. Grove, D. B. Wallace, T. Chen, and W. R. Cox, "Inkjet printing in the manufacture of electronics, photonics, and displays," in *International Symposium on Optical Science and Technology*, 2002, p. 94.

[152] A. Braeuer, P. Dannberg, U. Zeitner, G. Mann, and W. Karthe, "Application oriented complex polymer microoptics," *Microsyst. Technol.*, vol. 9, no. 5, pp. 304–307, 2003.

[153] V. Bardinal, B. Reig, T. Camps, C. Levallois, E. Daran, C. Vergnenègre, T. Leïchlé, G. Almuneau, and J. B. Doucet, "Spotted custom lenses to tailor the divergence of vertical-cavity surface-emitting lasers," *IEEE Photonics Technol. Lett.*, vol. 22, no. 21, pp. 1592–1594, 2010.

[154] R. Herloski, S. Marshall, and R. Antos, "Gaussian beam ray-equivalent modeling and optical design," *Appl. Opt.*, vol. 22, no. 8, p. 1168, Apr. 1983.

[155] T. Li, H. Kogelnik, and T. Li, "Laser Beams and Resonators," in *IEEE*, 1966, vol. 54, no. 10, pp. 1312–1329.

[156] M. Grabherr, R. King, R. Jäger, D. Wiedenmann, P. Gerlach, D. Duckeck, and C. Wimmer, "Volume production of polarization controlled single-mode VCSELs," in *Proc. SPIE*, 2008, p. 690803.

[157] B. Reig, V. Bardinal, J. B. Doucet, E. Daran, T. Camps, M. Aufray, A. Lamure, and C. Tendero, "Study of SU-8 reliability in wet thermal ambient for application to polymer micro-optics on VCSELs," in *Japanese Journal of Applied Physics*, 2014, vol. 53, no. 8 SPEC. ISSUE 2.

[158] D. Barat, V. Bardinal, I. Dika, O. Soppera, a. Rumyantseva, B. Reig, M. Renault, a. Bruyant, J. B. Doucet, T. Camps, J. P. Malval, and E. Daran, "Microlens self-writing on vertical laser diodes by Near Infra-Red photo-polymerization," *Microelectron. Eng.*, vol.

111, pp. 204–209, Nov. 2013.

[159] B. Reig, V. Bardinal, T. Camps, Y. G. Boucher, C. Levallois, J. B. Doucet, D. Bourrier, E. Daran, and J. Launay, "Polymer tunable microlens arrays suitable for VCSEL beam control," in *Proc. of SPIE*, 2012, vol. 8428, p. 84280N–84280N–10.

[160] A. El Hasni, S. Pfirrmann, A. Kolander, E. Yacoub-George, M. König, C. Landesberger, A. Voigt, G. Grützner, and U. Schnakenberg, "Six-layer lamination of a new dry film negative-tone photoresist for fabricating complex 3D microfluidic devices," *Microfluid. Nanofluidics*, vol. 21, no. 3, p. 41, 2017.

[161] S. Abada, L. Salvi, R. Courson, E. Daran, B. Reig, J. B. Doucet, T. Camps, and V. Bardinal, "Comparative study of soft thermal printing and lamination of dry thick photoresist films for the uniform fabrication of polymer MOEMS on small-sized samples," *J. Micromechanics Microengineering*, vol. 27, no. 5, p. 55018, 2017.

[162] B. Derby, "Inkjet Printing of Functional and Structural Materials: Fluid Property Requirements, Feature Stability, and Resolution," *Annu. Rev. Mater. Res.*, vol. 40, no. 1, pp. 395–414, 2010.

[163] L. Jacot-Descombes, M. R. Gullo, V. J. Cadarso, and J. Brugger, "Fabrication of epoxy spherical microstructures by controlled drop-on-demand inkjet printing," *J. Micromechanics Microengineering*, vol. 22, no. 7, p. 74012, 2012.

[164] F. Chen, J. Lu, and W. Huang, "Using Ink-Jet Printing and Coffee Ring Effect to Fabricate Refractive Microlens Arrays," *IEEE Photonics Technol. Lett.*, vol. 21, no. 10, pp. 648–650, 2009.

[165] G. M. Vahid Fakhfouri, "Drop-On-Demand Inkjet Printing of SU-8 Polymer," *Micro Nanosyst.*, vol. 1, no. 1, pp. 63–67, 2009.

[166] T. Ansbæk, C. H. Nielsen, N. B. Larsen, S. S. Dohn, A. Boisen, I.-S. Chung, D. Larsson, K. Yvind, and T. Ansbaek, "Polymer-coated vertical-cavity surface-emitting laser diode vapor sensor," *Proc. SPIE*, vol. 7615, p. 76150A–76150A, Feb. 2010.

[167] V. Bardinal, T. Camps, B. Reig, P. Debernardi, O. Soppera, D. Barat, J.-B. Doucet, and E. Daran, "VCSEL beam control with collective and self-aligned polymer technologies," *Proc. SPIE*, vol. 8276, p. 82760U–82760U–9, Feb. 2012.

[168] I. Chartier, J. Sudor, Y. Fouillet, N. Sarrut, C. Bory, and A. Gruss, "Fabrication of an hybrid plastic-silicon microfluidic device for high-throughput Genotyping," *Micromach. Microfabr.*, vol. 4982, pp. 208–219, Jan. 2003.

[169] P. Vulto, N. Glade, L. Altomare, J. Bablet, L. Del Tin, G. Medoro, I. Chartier, N. Manaresi, M. Tartagni, and R. Guerrieri, "Microfluidic channel fabrication in dry film resist for production and prototyping of hybrid chips.," *Lab Chip*, vol. 5, no. 2, pp. 158–62, 2005.

[170] Y. C. Tsai, H. P. Jen, K. W. Lin, and Y. Z. Hsieh, "Fabrication of microfluidic devices using dry film photoresist for microchip capillary electrophoresis," *J. Chromatogr. A*, vol. 1111, no. 2, pp. 267–271, 2006.

[171] K. Stephan, P. Pittet, L. Renaud, P. Kleimann, P. Morin, N. Ouaini, and R. Ferrigno, "Fast prototyping using a dry film photoresist: microfabrication of soft-lithography masters

for microfluidic structures," *J. Micromechanics Microengineering*, vol. 17, no. 10, pp. N69–N74, 2007.

[172] J. Perchoux, L. Campagnolo, Y. L. Lim, and A. D. Rakic, "'Lens-free' self-mixing sensor for velocity and vibrations measurements," in *2010 Conference on Optoelectronic and Microelectronic Materials and Devices*, 2010, pp. 43–44.

[173] R. F. Bonner and R. Nossal, "Principles of Laser-Doppler Flowmetry," Springer US, 1990, pp. 17–45.

[174] D. Dopheide, V. Strunck, and H. J. Pfeifer, "Miniaturized multicomponent laser Doppler anemometers using high-frequency pulsed diode lasers and new electronic signal acquisition systems," *Exp. Fluids*, vol. 9, no. 6, pp. 309–316, Sep. 1990.